Lappeenrannan teknillinen yliopisto
Lappeenranta University of Technology

Jarkko Vartiainen

MEASURING IRREGULARITIES AND SURFACE DEFECTS FROM PRINTED PATTERNS

Thesis for the degree of Doctor of Science (Technology) to be presented with due permission for public examination and criticism in the Auditorium 1382 at Lappeenranta University of Technology, Lappeenranta, Finland on the 27th of April, 2007, at noon.

Acta Universitatis
Lappeenrantaensis
264

Supervisors Professor Heikki Kälviäinen
Docent D.Sc (Tech.)Joni-Kristian Kämäräinen
D.Sc. (Tech.) Lasse Lensu
Department of Information Technology
Lappeenranta University of Technology
Finland

Reviewers Professor Risto Ritala
Measurement and Information Technology
Tampere University of Technology
Finland

D. Sc. (Tech) Matti Niskanen
Department of Electrical and Information Engineering
University of Oulu
Finland

Opponents Professor Janne Heikkilä
Department of Electrical and Information Engineering
University of Oulu
Finland

Professor Risto Ritala
Measurement and Information Technology
Tampere University of Technology
Finland

ISBN 978-952-214-370-9
ISBN 978-952-214-371-6 (PDF)
ISSN 1456-4491

Lappeenrannan teknillinen yliopisto
Digipaino 2007

Preface

The work presented in this thesis has been carried out at the Laboratory of Information Processing in the Department of Information Technology at Lappeenranta University of Technology, Finland, during the years 2003-2006.

First and foremost I would like to thank my supervisors, Joni-Kristian Kämäräinen, Lasse Lensu and professor Heikki Kälviäinen. Their help and support during the project is greatly appreciated.

I would also like to thank co-authors of the publications, Albert Sadovnikov, Alexander Drobchenko, they have also been involved with the project from the start. Also discussions with Ville Kyrki and Pekka Paalanen have been very helpful during the course of this long project. The constructive comments from reviewers Dr. Matti Niskanen and professor Risto Ritala are gratefully appreciated.

For financial support I would like to thank Papvision project partners, the European Union, Tekes, Stora Enso Oyj, UPM-Kymmene Oyj, Myllykoski Paper Oy, Metso Paper Oy and Labvision Technologies Oy. Research for the thesis was conducted under Tekes projects 70049/03, 70056/04 and 40483/03. Also support from Lauri and Lahja Hotinen fund, Eemil Aaltonen fund, and the Research Foundation of Lappeenranta University of Technology (LTY:n tukisäätiö) is appreciated.

For the great working environment, I would like to thank the staff of the IT department, it was a pleasure working there. Special thanks go to my colleagues, Leena, Jani, Jarmo, Toni ja Saku, who participated the lectures and courses and made them somewhat more easier to bear. Also my symphaties for the people who had the (un)fortunate pleasure of sharing an office with me, Pekka, Tomi and Tuomas, hopefully you are not permanently traumatised by your experience.

Lappeenranta, March 2007

Jarkko Vartiainen

Abstract

Jarkko Vartiainen
Measuring irregularities and surface defects from printed patterns
Lappeenranta, 2007
116 p.

Acta Universitatis Lappeenrantaensis 264
Diss. Lappeenranta University of Technology

ISBN 978-952-214-370-9
ISBN 978-952-214-371-6 (PDF)
ISSN 1456-4491

Quality inspection and assurance is a very important step when today's products are sold to markets. As products are produced in vast quantities, the interest to automate quality inspection tasks has increased correspondingly. Quality inspection tasks usually require the detection of deficiencies, defined as irregularities in this thesis.

Objects containing regular patterns appear quite frequently on certain industries and science, e.g. half-tone raster patterns in the printing industry, crystal lattice structures in solid state physics and solder joints and components in the electronics industry. In this thesis, the problem of regular patterns and irregularities is described in analytical form and three different detection methods are proposed. All the methods are based on characteristics of Fourier transform to represent regular information compactly. Fourier transform enables the separation of regular and irregular parts of an image but the three methods presented are shown to differ in generality and computational complexity.

Need to detect fine and sparse details is common in quality inspection tasks, e.g., locating small fractures in components in the electronics industry or detecting tearing from paper samples in the printing industry. In this thesis, a general definition of such details is given by defining sufficient statistical properties in the histogram domain. The analytical definition allows a quantitative comparison of methods designed for detail detection. Based on the definition, the utilisation of existing thresholding methods is shown to be well motivated. Comparison of thresholding methods shows that minimum error thresholding outperforms other standard methods.

The results are successfully applied to a paper printability and runnability inspection setup. Missing dots from a repeating raster pattern are detected from Heliotest strips and small surface defects from IGT picking papers.

Keywords: quality inspection, paper industry, regular patterns, thresholding, automated optical inspection, Fourier transform, machine vision, image processing and analysis, Heliotest

UDC 676.017.7 : 004.932.2 : 004.921

3D	3 dimensional
$\vec{a}$	Vector a
$\mathfrak{F}$	Discrete Fourier transform
$\mathfrak{F}^{-1}$	Inverse discrete Fourier transform
$\mathfrak{M}(u,v)$	Mask filter
$\mu(x)$	Mean
$I(u,v)$	Unit function
N	Newton
$N(\mu,\sigma)$	Normal distribution
R^2	Coefficient of determination
σ	Standard deviation
$\xi(x,y)$	Spatial image
$\Xi(u,v)$	Fourier transformation of $\xi(x,y)$

CCD	Charge-coupled device, imaging sensor
FFT	Fast Fourier Transform
H	Multiplicative noise function
h	Histogram
ISO	International Standardisation Organisation
$L*a*b*$	Adams Chromatic Value Space
pdf	Probability density function
Pa	Pressure in pascals
RH	Relative humidity (in air)
RGB	Red, Green, Blue colour space
S	Surface area
T	Threshold
u,v	position in Fourier domain
x,y	position in spatial domain
VVP	Velocity viscosity product

Chapter I

Introduction

The purpose of this thesis is to find methods to perform automatic visual quality inspection for two quality inspection tasks in the paper and printing industry. Quality inspection and monitoring are essential steps when today's products are sold to the markets. Consistency in the quality inspection process is crucial in order to guarantee that different production batches meet the required quality criteria. Often, the inspection is conducted visually by trained personnel, which means that the results can be subjective for various reasons such as difference in opinions, tiredness and other physiological or psychological factors.

Machine vision can overcome some of these human deficiencies: Computers do not get tired and produce repeatable results under standardised inspection conditions. In the paper and printing industry, these quality inspection problems are encountered when paper printing quality is assessed. Paper grade quality is determined by printing a test pattern on a paper and then various measurements are taken and the test paper inspected visually by laboratory staff with a magnifying class or a microscope.

1.1 Research questions

The specific problems that are addressed in this thesis are the detection of irregularities from regular patterns and the detection of small and sparse details from a paper surface. Such problems are inherent in the Heliotest and picking test. The Heliotest is a standard method in the paper industry to test the smoothness of printing paper. Smoothness is related to paper printability. The smoother the paper, the better the ink absorbs onto the paper, resulting in colourful and detailed prints. The picking test measures the surface strength of a paper. It gives a rough indication of how fast a given paper can be printed before the paper surface starts to tear due to friction forces affecting the paper surface during print head and paper interaction.

1.1.1 Detecting irregularities from regular patterns

In the Heliotest, half-tone dots are printed on a strip of paper so that the spacing of the dots stays the same but the size decreases towards the end of the strip. The dots form a regular raster pattern on the paper surface. Due to roughness of the paper, ink does not always absorb to the paper resulting in missing or partially missing dots in the regular pattern. In the paper and printing industries, paper quality is determined by counting the distance to the 20th missing dot from the start of the printed regular area [36]. This is the first main research problem in the thesis; the detection of defects from regular patterns.

An image processing sub-field which contains many similar characteristics to regular patterns is texture analysis. In texture analysis, however, the most typical problem is to distinguish between different types of textures, and thus, the proposed approaches favour between-texture type classification. Irregularity detection, however, needs within-texture type of classification. Still, there are many useful texture characteristics and notations that can be used, e.g., half-tone dots can be considered as texture atoms and their spacing can be represented as the spatial interrelationships between the atoms [28]. Research related to irregularity detection has been conducted in fabric defect detection (e.g., [12]), but there the problem setting is too loose for missing dot detection: fabric defect detection is primarily concerned about the location of a possible error, but in missing dot detection, it is necessary to find what is wrong in the given location. In other words, one needs to find both the locations where there are irregularities, and what kind of irregularities are present, e.g., a partly or completely missing dot or a group of dots. Specific image processing methods for missing half-tone dot detection have been proposed, e.g., by Langinmaa [53], and Heeschen and Smith [31]. Their methods are based on template matching or binary level processing. According to the authors of both methods, their weakness is the difficulty of distinguishing the exact number of missing dots from areas that contain clusters of missing dots.

1.1.2 Detecting small and sparse details from the background

The second research problem in the thesis is the detection of small and sparse details from a paper surface as is the case in the picking test. The picking test is performed with a special printing oil that is printed at accelerating speed on a paper surface. At certain speed, the paper surface starts to tear due to the increasing force affecting its surface. At first only some fibres start to lift from the paper and then the paper surface starts to tear up more visibly. These small surfacing fibres are small defects that need to be detected from the background. In the imaged samples, the proportion of pixels related to defects is typically very small, making the grey-level histograms almost unimodal. Additionally, the grey-level values of both the defects and surface overlap significantly. The spatial distribution of the defects can be considered random, and thus, general thresholding methods are applicable.

Binary thresholding is one of the most commonly used and essential operations in digital image processing, and in many applications thresholding is used at some point of the algorithm. Even though the operation itself is very simple, the problem of selecting an optimal threshold value is not trivial at all. For a single image, the optimal value can be

selected manually, but adaptive thresholding methods exist intended to automatically estimate the optimal value. Due to its importance, adaptive thresholding has been studied for a few decades, and a wide variety of different methods have been proposed (see, e.g., [79]). The extensive work in the past should have resulted in a proper method existing, for any problem. Since the different methods value different properties, method selection depends on the characteristics of the problem domain.

This thesis assesses the ability of adaptive thresholding to bring up fine and sparse details. Most methods perform well when the image foreground and background constitute areas of sufficiently equal sizes, and the grey level values have substantially non-overlapping distributions [79]. However, when either or both of the above assumptions are not valid, major difficulties can be encountered. The problem can be solved by defining the necessary statistical properties in the histogram domain and by analysing the performance of well-known and well-performing general adaptive thresholding methods and methods specifically applicable to unimodal histograms. Another approach to solve the problem could be to use techniques widely used in content based image retrieval where the goal is to locate images of a same object/scene from different angles. These methods often rely both on colour information and spatial information of the colour to better separate different images from each other [34]. The basic underlying idea is that instead of using only colour information, both colour and spatial information is used to better separate different images from each other. The same idea could be applied to more clearly separate small and sparse defects from the background. To include spatial information, a spot filter that emphasises the small bright spots on samples is used in this work due to its simplicity and ease of use.

1.2 Contributions

The main contributions of this thesis are methods for detecting irregularities from regular patterns and the study of methods for detecting small and sparse surface defects. The methods have been created to fulfil the needs of the paper and printing industry, but they are not limited these particular fields. The methods for detecting irregularities from regular patterns are robust and can be applied anywhere where regular data is available. Evaluation of these methods has proven them to be very accurate and relatively simple to implement, which should make them very attractive for use in quality inspection tasks.

The work presented in this thesis is a part of the larger Papvision project (http://www.it.lut.fi/project/papvision) investigating machine vision methods for paper quality inspection. Several people took part in the Papvision project. This thesis is a monograph, but some of the results have been published in scientific conferences or other scientific media (in [77, 20] the author participated in development, was one of main authors and performed the experiments, in [91, 92, 93, 94] the author developed the methods, wrote the articles and performed the experiments). The author provided software and helped build the setup introduced in Chapter 5.

1.3 Structure of the thesis

Chapter 2 gives background information about the research area. It gives an overview of the methods and procedures used today in paper structure analysis and reviews previous

research in the area.

Chapter 3 describes the first research problem of the thesis, the detection of missing atoms from repeating patterns. The chapter describes the problem in detail and then gives a detailed explanation of the methods that were developed during the course of the research. After presenting theoretical considerations, the experiments are described and the results given.

Chapter 4 considers the second problem of the thesis, namely the detection of small and sparse details. The structure of this chapter follows that of Chapter 3. First the theoretical background for the problem is introduced and then the methods proposed and their validity are analysed. The methods are then verified with both artificial and real data.

Chapter 5 presents the application of the proposed methods to experimental test setup. The setup specifications are shown and a method to detect the measurement area from input images is presented. The setup is then used at paper mills to perform the Heliotest and picking test. The measurements obtained by the system and by industrial experts are given in appendices II and III.

In Chapter 6 the weaknesses and strengths of the methods introduced in Chapters 3 and 4 are discussed. The discussion also contemplates other possible applications where these methods could be used.

Chapter II

Paper quality inspection

Inspecting product quality is common in all industries and the paper and printing industry is no exception. Quality inspection can be performed at many stages of the production cycle, raw materials, end products and intermediates of a manufacturing process can all be tested. The aim of quality inspection is to numerically describe the most relevant properties or features of a product or its intermediate or both. Unfortunately inspection tests do not always measure the exact features of the product in question, e.g., object density can be determined by measuring its mass and volume. For inspection to be relevant, the feature measured should correlate well with a property of the product under consideration.

In industry, inspection can have other functions. It can be used to control process conditions or for quality assurance that the end products are consistent, i.e. their properties do not vary, and they meet set quality criteria. Inspection can also be used to obtain additional value for marketing purposes. Selecting the proper test for different situations requires careful consideration.

Nowadays, more and more tests are done on-line during production. This gives the benefit of being able to adjust production process right away in order to maintain an efficient and consistent production cycle. Therefore industry wants to perform as many tests as possible on-line. Unfortunately, not all tests can be performed on-line due to a lack of proper sensors or methods, and furthermore some tests require strict control over the measurement environment, which is rarely possible on-line. For some products customers may also require varying quality inspections on purchased products.

2.1 Paper quality properties

Paper quality is tested just as any other industrial product. According to [55] the basic questions to ask when conducting inspections are as follows: What are the process conditions and the variations that are wanted to be monitored with the testing and

what feature or function of the material should the inspection describe. Answering these questions can identify the relevant tests and analyses.

Process analysis tries to define the control variables of paper making process that allow it to run smoothly and produce paper with the necessary properties. The first step in process analysis is defining critical control variables. A control variable is critical if changing it positively affects one process or product property and at the same time negatively affects another. These critical control variables can be listed and their effect on the whole process identified. In order to improve any paper making process, knowing how it affects on the individual fibres and the pulp is necessary. Measuring single fibre properties is useful for this purpose.

Paper is a network formed by bonding of fibres and fibre fragments. The properties of all the components, including fillers and additives, influence the properties of the paper. Single fibre properties describe statistical properties of fibres such as their fibre length. Fibres can be classified by given criteria, e.g., classifying them in to early- and late-wood fibres [32]. Analysis of pulp fibres is an important area of pulp and paper quality inspection but is beyond the scope of this thesis.

Product analysis defines the properties that relate to the use of paper. Important features, requirements and measures concerning the use of a product are required for product analysis. This thesis is mainly related to product analysis since the properties of the end product are measured, i.e., properties related to the printability and runnability of the paper. An example of a product analysis measurement is paper runnability. A paper requires sufficient strength so that it does not tear during the printing process. Product analysis defines the specific strength property to measure, tensile strength or tear strength. Table 2.1 describes several tests that are used to describe the functional requirements of paper products.

Many physical properties describe the paper characteristics. The properties can be grouped as follows [56], of which the most relevant to the thesis are in bold and introduced in the following subchapters:

-Basic properties

-Strength properties

-Stiffness properties

-Structural properties

-Surface properties

-Absorption properties

-Optical properties

A number of methods exist to measure these properties and it is a large topic in itself. This thesis concentrates only on tests that measure properties in bold in the list. Other properties are only briefly introduced. Paper properties discussed below are described in more detail in [56, 83, 90, 1].

The aim of inspecting a piece of paper or board is often to obtain information about the properties of a much larger set than that on which the test is made. Therefore it is essential to perform the test on a sample that best represents all the produced material. To be representative, each sample has to have an equal statistical probability to be included into the sample set. In practice this requirement is difficult to fulfil. Paper is delivered in large rolls and obtaining a sample from the middle or centre of a roll is not viable. Therefore samples are obtained from many rolls and using the to most frequently applied principle, the number of rolls sampled should be relative to the square root of the total number of rolls in the consignment. described in detail in [44].

From each sampled roll, a few sheets of paper are cut with a minimum size of 300×450mm The sheets are combined into one sample set that is randomised by careful mixing. From these larger sheets, test pieces can be cut based on the specifications of the different inspection tests.

The next requirement for paper inspection is the testing environment. Wood fibres are naturally hygroscopic and thus paper easily absorbs moisture from the ambient atmosphere or releases moisture if the atmosphere is drier than the moisture content of the paper. The moisture content of the paper affects almost all of its physical properties. Therefore the preferred conditioning climate is $50 \pm 2\%$RH and 23 ± 1^oC [41]. Other alternative allowed in tropical countries is 65% and 27^oC. The normal conditioning time for paper is usually 4 hours which is relatively long since the absorption or desorption rate of moisture from and to paper is quite fast, it happens in the first minutes after the paper is moved from one atmosphere to another. Temperature is not as crucial a parameter, although it has been standardised mainly to keep the relative humidity within acceptable limits.

The most basic properties of any paper or board include moisture content, basis weight, thickness, density, and filler content. Paper and board trade is based on weight, therefore basis weight links the paper weight to its surface area. Thickness and density on the other hand describe the paper structure.

The moisture content of paper is determined simply by weighting the paper before and after drying at 105 ± 2^oC as per [40]. Moisture content is expressed as a percentage of the weight of the moist sample. Basis weight (grammage) is the weight per unit area of paper and board, expressed in g/m^2. This is determined by weighing a piece of paper with a known area as described in [42]. Thickness is measured in micro meters (μm). It is measured by using a thickness gauge at a paper sheet or sheets of paper compressed with a given pressure between two parallel plates. Density then is obtained as a ratio between the basis weight and thickness of the paper. Filler content is obtained by igniting the paper sample at 900^oC as per [43] or at 525^oC, depending on the filler composition.

Stiffness relates to a material's elastic properties and measures how much the material resists when it is deformed by an external load. Paper stiffness is usually measured as tensile stiffness and bending stiffness. Tensile stiffness is measured by subjecting the paper to a force parallel to the paper surface, the resulting deformation is elongation. This measure can be obtained at the same time with the tensile strength test. Bending stiffness measures the paper's ability to withstand a bending force when one end of the paper is tied down and the a force applied to free end. Methods for performing the test vary, but perhaps the simplest way is to use the paper's own weight and measure how

much gravity bends the paper from the horizontal level when one end is supported and the other hangs freely.

Other things to note about paper measures is the direction of fibres in the paper. Most machine made papers have the fibres aligned in the machine direction of the paper. This anisotropy is referred to as fibre orientation or paper directionality. Fibre orientation has a strong influence on paper properties depending on the direction of the paper. When results are reported, the direction of the test in relation to the paper should always be given. Depending on the manufacturing technique, the two sides of the paper can also be different, therefore if necessary, the properties of both sides of the paper should be measured. A review of different tests for paper coatings are presented in [96], some of the tests presented in the paper are also applicable for inspecting plain uncoated papers. Next the different properties of paper are considered.

2.1.1 Strength properties

Tensile strength can be used to describe the general strength of any material. For paper, it is the maximum force per unit width that a paper strip can resist before it breaks when the load is applied parallel to the length of the paper strip. Tensile strength is expressed in kN/m. The measure is dependant on fibre orientation and therefore the measurement direction should always be mentioned. Zero-span tensile strength measures the strength of individual fibres instead of that of the paper. It is a special case of tensile strength testing.

Bursting strength indicates how much pressure the paper can resist without breaking. The pressure is applied perpendicular to the paper surface. The unit for bursting strength is kPa. The bursting strength test is an old test for paper strength and it was developed empirically.

Internal tearing resistance measures the mean strength required to continue paper tearing from an initial tear in a single sheet of paper. It is very much dependant on the fibre orientation and therefore the direction in which the measurement is done should always be mentioned. The unit for expressing tearing strength is newton (N) or millinewton (mN).

Folding strength measures the paper's ability to withstand folding without breaking under a certain load. The load is constant but is usually much lower than the tensile strength of the paper. The folding strength is expressed directly as the number of double foldings the paper can withstand. The test is old and has present day uses when measuring paper aging, also banknotes are subjected to this test.

The surface strength of a paper tells the paper's ability to resist forces that pull fibre or fibre bundles from its surface. Low surface strength may cause linting and runnability problems in rotogravure printing or even destroy the printing result. Linting is a term that means slow accumulation of loose material, such us fibres from a paper surface, onto a printing blanket and inking unit in offset printing. It affects how ink transfers from the printing plate to the paper and causes loss of details in the print. The picking property is very similar to linting, the main difference is that in linting the material can be totally detached from its original location whereas in picking, the material such as fibres are at least partially bonded with the paper. Dusting is a term used to describe loose colour

pigments on the paper surface and it is closely related to linting and picking. Surface strength is usually measured with high viscosity, tacky oils or printing inks. The test sample is printed with at a continuously increasing speed and the speed at which the picking starts is measured. The product of the speed and print oil or ink viscosity is the measure of the surface strength.

The Z-directional strength of a paper measures the paper's ability to resist tensile loading in a direction perpendicular to the paper surface. After the Z-directional strength limit of the paper is reached, the paper structure breaks inside the paper but not at its surface. Essentially the paper is split into two parts so that the paper surface does not get damaged on either side. This kind of loading of paper happens often in offset printing and certain converting operations such as corrugating, folding and plastic coating.

2.1.2 Surface properties

The most important surface properties of paper are surface strength, roughness or smoothness, friction and gloss. Surface strength was described earlier in section 2.1.1. Paper smoothness or roughness describes paper surface topography. Paper smoothness is obtained by measuring airflow between a paper surface and measuring surface or edge. Information needed for these measures are pressure difference used to create the airflow, pressure of the measuring head against the paper surface, and the area of the measuring head. The volume of air flow per time unit is reported as roughness and the time for a certain air volume to stream out is called smoothness.

Friction has two main measures, static friction and kinetic friction. Static friction can be measured by attaching one paper to a surface and another to the bottom of a sled of known weight. Next the sled is placed on top of the paper attached to the surface and then the sled can be either pulled with an increasing force or the surface inclined until the sledge starts to move. Kinetic friction can be obtained by pulling the sled over the paper on the surface at constant speed and by measuring the average friction force over a specified length of sliding. More variations to the measures are obtained by changing paper orientations.

Gloss measures the interaction of light and the paper surface. There are four basic ways how light can interact with paper and usually they all can happen at the same time. Figure 2.1 shows what can happen when light hits a paper surface. Gloss measures the paper's ability to specularly reflect light. High gloss is desirable in high quality paper with many images. Paper with high gloss has a wider tone range than that of a matte surface. The downside of high gloss is that it usually impairs the readability of text and therefore in textbooks it is a highly undesirable property.

Gloss can be measured in many ways but the paper industry has adopted a 75^o specular gloss method. The angle refers to the angle at which the light is projected onto the paper surface and the angle at which it is viewed. The angle is given from the perpendicular to the paper surface. This angle was selected because it had the best correlation with visually perceived gloss. With gloss it is also important that the gloss is as even as possible, the higher the gloss the easier it is for a human to detect unevenness of gloss.

Table 2.1: Examples of tests used for describing the functional requirements of paper products [55]. Tests that relate to the topic of this thesis are in bold.

Required behaviour of paper	**Measurable properties**
Sufficient strength	Tensile strength Bursting strength Tearing strength Z-directional strength
Suitable structure	Density Air permeance
Correct optical properties	Brightness Opacity Colour
Suitable surface properties	**Smoothness or roughness** **Surface strength**
Sufficient stiffness	Bending stiffness Concora medium test Crush test Edge crush test

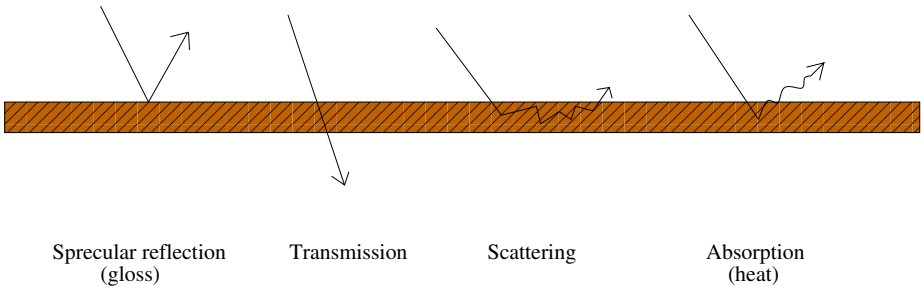

Figure 2.1: Light interaction with paper

2.1.3 Absorption properties

Absorption properties are important. In printing it is important to know how well ink or printing oil can adhere to a given paper type. Water repellency of a paper can obtained by measuring how much water it can absorb in a certain time period. This kind of measure is important for example in the production of tissue papers. Another way to measure absorption properties is to pull a liquid filled nozzle over the sample at varying speeds. The liquid in the nozzle can be coloured water or printing oil. During the movement the liquid fill the cavities of the paper and partially absorbs into the paper sample. At each speed the amount of colour absorbed is measured and in this way the amount absorbed can be estimated as a function of time.[83].

For printing papers, the absorbency of paper is often measured with printing tests. A common test used to measure how well ink absorbs to the paper is the ink stain test where ink is hand-smeared to a paper and then the ink shape is used to estimate the paper structure and evenness. A problem with this method is that it does not correlate well with other laboratory tests or with actual printing processes. The main reason is that the interaction time between the ink and the paper in ink stain test is much longer than in actual printing.

Rotogravure printing requires a specific test to measure how well ink absorbs to a paper. The greatest problem with rotogravure printing involves the reproduction of light and medium tones. Defects that appear are missing dots and waving. Waving defects are elongated density defects with an area about $1mm^2$ perpendicular to the printing direction [73]. Missing dots are inevitable at 5% half tone but disastrous when occurring at 20% to 30% half tones [73]. The number of missing dots is a traditional measure of rotogravure printability of paper. In laboratories, the Heliotest indicates the number of missing dots. The test pattern is a 110 mm long and 8 mm wide raster where the tone changes from dark to light. The size of the printed dots decreases towards the end of the test pattern [53, 13]. The quality of the paper is defined as the distance from the darker end of the test strip to the 20th missing dot on the strip. The longer the distance, the better the printing quality. Fig. 2.2 shows a sample image of a Heliotest strip.

Figure 2.2: Sample Heliotest strip with the measurement area, i.e. the area where the missing dots are measured, (110mm ×8mm) marked on the image.

2.2 Paper printability and runnability

Some of the properties described in the previous section relate to printability and runnability of paper. Printability is a quality potential of paper for a certain printing process. Good printability means that the paper in question is not very sensitive to different printing process variables and always produces good print quality. Defining printing

quality is however not absolute. It is dependant on the final use of the printed product. Some, but not all, properties that can be used to measure print quality are print density, resolution and evenness of the printed image. Printability tests depend on the printing process involved. Some tests are applicable for general printability inspection while others are dependant on the printing process. Paper absorption and surface properties relate closely to paper printability. A review of measures related to paper coating surfaces, paper structures and printability can be found in [13].

Runnability generally means the maximum speed of a printing machine possible without encountering any problems. Paper strength and surface properties affect the runnability of paper. Poor runnability is anything that can reduce printing efficiency, and insufficient runnability of paper can result in web breaks that suddenly stop production. More subtle ways of encountering runnability problems are cumulative effects such as linting, dusting, or piling which require processing to be stopped and maintenance cleaning operations to be performed. Slow drying times also affect the printing speed. Separating the inspection of printability and runnability can be difficult since printability problems often originate from runnability problems and vice versa.

Runnability is an essential problem for all printing papers. Runnability problems between different printing methods, such as rotogravure, flexographic, offset and even digital printing generally do not differ very much. Relevant differences appear between web printing and sheet printing. In web fed presses, good runnability means that the paper will run through the printing machine at planned speeds without problems and with few complications such as web breaks, stress variations and flapping. In newsprint, for example, a frequency of less than 2 web breaks per 100 paper rolls printed is desirable.

Other problems in web printing are cracking and blistering. Cracking is a phenomenon where central pages come off from a book/newspaper due to breaks at staple points. This property is generally related to paper humidity, and web offset papers are normally produced to low humidity to avoid blistering in the drying phase of a printing process. Unfortunately low humidity paper is brittle and can therefore crack during folding and stapling.

Blistering is a problem where the paper fibre matrix ruptures and blisters when steam expands inside a paper during the high temperature drying sequence that completes the web printing process. The main properties that affect blistering are paper moisture content, porosity of the paper coating layer, internal strength of the paper, ink coverage of the paper and drying temperature. Due to very rapid heating from ambient to 100^oC-150^oC the moisture in the paper evaporates and tries to escape through the coating layer of the paper or produces blisters if the vapour pressure exceeds the internal bonding strength of the paper.

In sheet fed printing, each sheet is printed separately. Therefore measuring runnability is more oriented to different types of feeding, transportation and delivery problems. Paper curl, poor stiffness and paper surface properties such as friction and static electricity influence sheet fed press runnability.

Curling means out-of-plane movement of a paper. Curl can result from different fibre orientation or fibre bonding on different sides of the paper. Fibre swelling and shrinkage due to moisture variations can also induce curling.

Static electricity refers to a paper's capacity to charge itself and the time required to discharge itself. Highly charged sheets collect dust easily and easily adhere together which will cause runnability problems.

Some paper properties affect runnability from a certain time after starting to print. Such time dependant problems occur basically due to interaction between the paper and printing ink. Linting, picking and piling are typical time dependent runnability problems.

2.3 Machine vision in quality inspection

When talking about computer vision, the topic can be separated into two main fields, namely computer vision and machine vision. The distinction between the two is a bit vague, but roughly it can be said that computer vision's ultimate goal is to emulate human vision [23] whereas machine vision is merely interested in using sensors attached to computers in industrial applications in which robustness and simplicity are the main virtues. Many quality inspection tasks today have been automated using computer- and camera-based systems. Earlier the computation power required by machine vision applications has somewhat deterred its use for industrial purposes. Now all is changing, as the field of science has matured and methods improved. The computational power of modern desktop computers has increased quite rapidly, which has made it possible to use methods that were computationally too complex in the past. interest in

The benefits of automation are quite clear. Cameras do not strain like human eyes do and the results are almost always repeatable, which is another huge benefit over human-based quality inspection. Repeatability of inspection is very important when it must be guaranteed that two batches of a product meet the same quality criterions. Sometimes it is not viable to do the quality inspection by human visual inspection. Such a case can be, for example, locating defective solder joints on circuit boards. The number of solder joints on one chip can be in the thousands and using somebody visually inspecting each solder point repeatedly is not effective [2].

Typical machine vision systems today consist of a single or multiple CCD cameras and an ordinary desktop computer (see Fig. 2.3). Typical machine vision applications require constant lighting conditions so that the obtained images remain constant or in order to ensure that fast moving objects are sufficiently illuminated for high speed cameras. After the image acquisition, the image is usually preprocessed in order to enhance contrast or to remove noise [97]. This can be done with special hardware or by computer. Further processing then allows more sophisticated image manipulation such as edge detection, contour tracking, thresholding, feature extraction and object recognition. These features can then be analysed by specially designed software which can then decide whether or not the imaged object meets the specifications needed and reacts accordingly by marking the defective part or by removing it from the production line [97]. The benefits of using simple off the shelf commercial cameras come from upkeep and maintenance. It is rather easy and usually cheap and fast to obtain spare parts if they can be found in almost every electric hardware store [60].

Of course there can be more demanding tasks which can require some kind of robot to inspect places where it is difficult or dangerous for a human to go. An example of such an application is water pipes inspection [62] or a nuclear plant where the radiation is a

problem [60]. It is impossible for a human to fit into a small water pipe, but a specific robot has been developed for just that kind of task [62]. Naturally not all tasks are as demanding but can still benefit from computer vision based quality inspection systems. In fact such systems can be found in many industrial areas. Automatic visual quality inspection is used, for example, for pulp [9, 11], metal [63], print [95], wood [71], textile [66] and electronic components [2, 97]. A more thorough overview of recent industrial machine vision systems and applications can be found in [60] and earlier surveys in [65, 14].

Section 2.1 introduced measures for paper properties. Next some automated methods for measuring paper properties are introduced. It is good to keep in mind, though, that most of the tests mentioned in Section 2.1 are still performed manually by laboratory experts. Special emphasis on this survey is put on methods that have been used for the Heliotest (introduced in Section 2.1.3) and picking test (Section 2.1.1) since they are the main topics of this thesis. A brief overview of some methods that are used for quality monitoring in steps when wood is processed to paper are introduced in order to give some understanding of what happens during the paper making process.

2.3.1 Paper making process analysis

Computer vision based systems are used quite widely in the paper industry. Wooden chips that are used for making the pulp are analysed based on the colour of the chips on the conveyor [85]. Colour information can reveal how much bark and how much wood the chip flow contains. All measurements are done online during production. As this is a commercial product, detailed information about the colour analysis is not available.

The composition of pulp can be analysed using machine vision. The speed at which the pulp moves on the conveyor and the high resolution required dictates that special arrangements regarding hardware is required. The hardware consists of several CCD camera lines that shift their electrical charges from one line to the next one in synchronisation with the inspected product movement. This shift procedure is performed in such a way that an image of each product line is acquired in several positions and the single acquired images are added to each other by the camera electronics in order to pro-

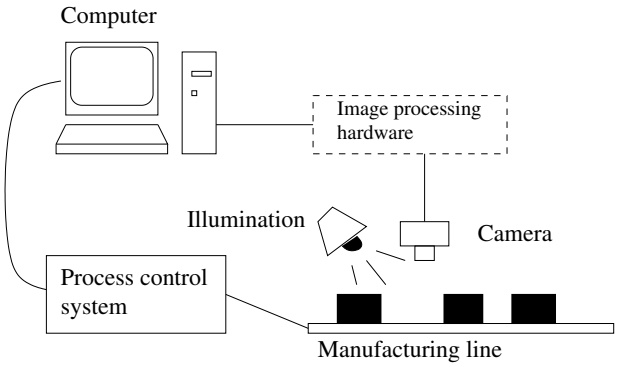

Figure 2.3: Typical machine vision based industrial system.

duce a single line-image that has several times more dynamic range than a conventional linear camera, therefore allowing impurity detection under the appropriate inspection requirements [9]. The obtained images are sharp, but their lighting is not homogeneous. Therefore the images can not be thresholded with uniform threshold to detect impurities but instead a section of image is chosen from each image. Each of these sections have more even lighting distribution. To further enhance lighting evenness, the darkest and brightest images are removed from the block image series. After these images have been removed, the mean and standard deviation of the remaining images are calculated and this information in turn is then used for setting appropriate threshold [9]. Impurities in pulp are then detectable by thresholding. A similar system is proposed in [8], where the paper making process is imaged on-line using a TDI (Time delay integration) camera. Neural networks are used to train filters which in turn can be used to detect defects from the on-line images.

A system for detecting a dry line at the wet end of a paper machine is introduced in [7]. The dry line of paper is the location where water disappears from the surface of the pulp web in the wet end of a paper machine. In the study in [7] a standard CCD-camera was used with some special lighting arrangements to image the dry line of the paper web. From the images a dry line edge profile is extracted and it is compared to basis weight and moisture data. The edge profile data correlates well with basis weight and therefore the edge profile information near the wet end of the paper machine can be directly used to control the paper making process. A comparable method is also proposed in [50]. The contribution of the authors is the way camera is positioned next to the paper machine, instead of above it. This placement makes camera maintenance easier and the camera is not subjected to the moisture and hot air above the paper machine.

Performance and suitability of CCD line cameras for paper web inspection is reviewed in [52]. In the paper CCD line camera performance is analysed regarding its charge transfer efficiency which in turn affects the imaging response of the camera. Camera suitability for use in paper web inspection is studied by detecting streaks in the paper web at different locations of the camera cell.

The application of Fourier transform for examining the dimensions of a paper web is introduced in [27]. Ways of obtaining non blurry still images from a fast moving paper web (up to 20 m/s) are also studied. In their earlier paper [26] Hansson and Manneberg studied the suitability of Fourier transform for measuring paper dimensions and fibre orientation on a stationary paper.

In [89] 9 different texture feature extraction methods for characterising paper properties are compared. The aim of the work was to study the suitability of the different texture features for classifying papers into different grades. The features were classified based on unsupervised learning. The data was also visualised by using a self-organising map (SOM) to map the multidimensional feature vectors into a more easily understandable 2-dimensional map. The authors conclude that best clustering results are obtained by using a local binary pattern to obtain the texture features. They suggest that a SOM and feature extraction could be used on-line to characterising paper during paper making process. Based on the paper characteristics, a paper machine could be adjusted on-line by using the information provided by the SOM and the extracted features.

2.3.2 Paper product analysis

In [33] Ho and Smith present a way to measure basis weight, width, and moisture content online. Labelling this as a machine vision application is somewhat questionable since no pattern recognition is used nor actual images grabbed from the paper. Instead the paper machine's own sensor information is used. First, paper mill personnel set limits for different properties like basis weight. Then, the system colour codes this information to a quickly understandable form so that the paper machine operators can have a good overview of the general quality of the paper they are making. Quantisation noise in the sensor data is reduced by low-pass filtering.

In [18] Don et al. describe a method which produces a 3D image of a paper. The process is quite straight forward where the paper is sliced with a special purpose machine called a microtome. Microtomes are designed to cut uniform slices for microscope imaging. After slicing, a microscopic image is taken from the paper slice on which the analysis is to be done. The system is meant to analyse paper coating used on high quality papers. The purpose of the coating is to fill cavities and covets on the paper's surface. The distinction between the paper and the coating is based on colour information. Because there are different coatings, user intervention in the beginning of the process is required. A user must loosely mark the coating on the first image so that the colour of the coating can be known. No spatial information is stored. The decision if an image pixel is coating or not is based on colour information of the current pixel and also pixels adjoining the current image. After the whole sample is sliced, a 3D image of the sample can be formed with the coating and paper segmented separately. Naturally this process is time consuming and it also destroys the sample.

In [6] Bergman et al. use a rather complex colour segmentation technique to evaluate ink dots on a printed pattern. First, the printed pattern is imaged with a standard CCD camera. Then the obtained image is converted from RGB colour space to CIE $L^*a^*b^*$ colour space. This is done to avoid the distance measurement problems inherent in the RGB colour space. Namely the metrics in RGB colour space do not represent colour differences on a uniform scale therefore making it difficult to evaluate the similarity of different colours based on their distance in RGB space. The segmentation is done in three steps. First, parameters for rough initial segmentation are obtained using a Fuzzy Kohonen clustering algorithm. After segmentation the resulting image is eroded using a binary erosion algorithm. Fine refinement of the segmentation is then performed using a fuzzy cluster volume algorithm to learn the parameters of the refined clusters. Initial rough segmentation uses only colour information in order to speed up processing, the final refining segmentation step uses also the pixel's spatial information. Rough initial segmentation information is used to obtain balanced training data for the actual refining final segmentation. The purpose of the erosion operation is to prevent the initial rough segmentation from selecting uncertain pixels that are located near the edges where colours change. After final segmentation the shape of the ink dots can be analysed.

A theory for a colour histogram based printing quality assessment method is presented in [59]. Initially the illumination of the image has to be normalised since histogram based methods are quite sensitive to illumination changes [59]. This is done based on a method proposed in [29]. After illumination normalisation the dimensionality of the colour histogram is reduced by projecting it into RG, GB and BR colour planes. Next

the three planes are rotated and summed. In order to further reduce dimensionality a fourth-order moment is calculated for the summed matrix. Finally eigen-values from the fourth-order moment are calculated and are used in a supervised three layer neural network for image classification. The proposed system can detect colour differences of similar images under different lighting conditions, but cannot detect any spatial changes.

In [48] a thermal imaging camera is used for various paper quality property inspection tasks. According to the study, camera response does not directly measure, for example, paper curliness right after it has been printed. Instead the variations in thermal image correlate well with for instance paper curling after the paper has been heated in the printing machine.

Two prior methods have been proposed for counting the missing dots in gravure printing. The first method [31] uses morphology to locate the missing dots. The procedure is quite straightforward. First the input image is converted to a binary image by thresholding, after which the median of the dot size is calculated. Next a series of dilations are performed until the area covered by the swelling dots reaches a predefined threshold. After the dilation step the image contains mostly missing dots and some noise. Noise is removed based on the estimated size of an actual dot. The size of the missing dot hole is estimated statistically from the dilated image. Finally, after noise removal, the missing dots are estimated based on the size of the hole in the dilated binary image. If multiple missing dots are next to each other, then the "large" missing dot is divided by the size of the single missing dot in order to separate the multiple missing dots from each other. This method works quite well if the missing dots are not grouped but with multiple missing dots near each other the method struggles to differentiate the actual number of missing dots in the missing dot cluster [31]. Determining the stopping threshold for the dilations can also be problematic. Numerous missing dots can mean that dilations are carried on even when the dots have already merged and and after a while actual missing dot "holes" get covered with the swelling dot area until the threshold is reached.

Another approach to calculate the number of missing dots in gravure printing was proposed in [53]. First the input image is filtered using a combination of median and minimum filters.

$$\begin{aligned} y_{ij} &= med(z_1, z_2, z_3, z_4) \\ z_1 &= min(x_{i,j-v}, \ldots, x_{i,j} \ldots, x_{i,j+v}) \\ z_2 &= min(x_{i-v,j}, \ldots, x_{i,j} \ldots, x_{i+v,j}) \\ z_3 &= min(x_{i+v,j-v}, \ldots, x_{i,j} \ldots, x_{i-v,j+v}) \\ z_4 &= min(x_{i-v,j-v}, \ldots, x_{i,j} \ldots, x_{i+v,j+v}) \end{aligned} \tag{2.1}$$

where x_{ij} is the grey level pixel value at location i, j, v is a constant that defines the region of interest. Med() denotes median of values in parenthesis and min() denotes minimum of values in parenthesis. The idea of the median/minimum filter is to alleviate the strong tendency of a minimum filter to expand dark (dot) area. After pre-processing, the image is filtered using a matching filter that is designed to find dark areas that are surrounded with white areas. According to the author, several templates were tested but the exact design seemed to have little significance provided that it is of the right type [53]. Template matching is implemented by using convolution filtering. The decision to accept a response as a missing dot is based on the size of the response. Supervised learning is used to teach a proper threshold value for the size of the response. Due to the

large size of Heliotest samples, the samples are imaged in parts and a threshold for each part is taught separately. The problem with this method is the same as in [31], namely when the missing dots are clustered next to each other, the template matching fails due to fact that the missing dot area is larger than originally anticipated.

Article [30] introduces an on-line method for detecting missing dots from printed paper. An optical method for counting missing dots based on optical Fourier analysis is used. First the method is analysed and the optical Fourier transforms response is derived analytically. Optical Fourier transform is obtained by using a special imaging arrangement. Details about the arrangement can be found from the article. In the analytical analysis of optical Fourier transform, the authors first derive Fourier transform for a perfect screen dot pattern with dot-to-dot interval a and dot size b. The object is limited by a circular aperture with diameter D. This limitation of the field of view makes the comparison of intensities in the Fourier plane possible. The result of this Fourier transformation is a Fourier pattern with the same kind of symmetry as the original image. Separation of peaks in the Fourier plane however is inversely proportional to the corresponding distances in the original spatial screen dot pattern and the width of the peaks is much smaller than the diameter b of a screen dot. The main result of this transformation is a Fourier plane with intense central peak surrounded by regular peaks with decreasing intensities as they progress further from the central peak.

Next dots are randomly removed from the perfect screen dot pattern and a Fourier plane equation derived for this imperfect screen dot pattern. The imperfect pattern $r_{imperfect}(x, y)$ can be considered to consist of perfect pattern $r_{perfect}(x, y)$ and of a defect $r_{defect}(x, y)$ as follows

$$r_{imperfect}(x, y) = r_{perfect}(x, y) + r_{defect}(x, y). \tag{2.2}$$

The same was deemed to apply in the Fourier plane. The missing dots in the imperfect dot pattern add light to the central peak in the Fourier plane and remove light from the other regular peaks. The important result of this phenomenon is that the regular peaks in the Fourier plane stay in their place but the light transferred from them due to missing dots spreads between the peaks. The intensity of the peaks does not necessarily diminish as the number of missing dot increases, but rather oscillates. Therefore the number of missing dots can be estimated by measuring intensities between the peaks. In practical experiments the authors confirm that actual measurements are in good agreement with their theoretical predictions. The method can calculate the number of missing dots from an image, but it does not return location information about the missing dots and therefore is not suitable for the Heliotest.

Some commercial applications [21, 38, 51] for paper quality assessment also exist, [38] for example uses local binary patterns in analysing paper surface. Unfortunately as these are commercial products, detailed information about these methods is not available.

2.4 Summary

Quality control via automation is gaining popularity as methods in computer vision get faster, more refined and more accurate. Applications that were possible but not practical 10–20 years ago are very much applicable today as the computing speed of computers

has increased and cheaper cameras have appeared. Especially in industry, line cameras are often used. The cameras are fast and simple image processing tasks can be done at a camera hardware level therefore reducing the processing power required by the computer software.

In the paper and printing industry, many tests have not yet been automated, e.g., propositions how to automate the picking test have not been found during the course of the project. Some of the tests require special arrangements in which automation is not practical due the necessary user interaction involved. Some tests on the other hand could benefit from automation: Results would be more repeatable and the likelihood of human errors would reduce. Examples of such tests are the picking test and the Heliotest. Both have definite features that are measured and both are straining for humans to perform for long periods of time.

Chapter III

Printability evaluation by counting missing dots

This chapter describes automatic inspection methods for rotogravure print inspection. The inspection is conducted by calculating missing dots from rotogravure printed Heliotest strips. The Heliotest was introduced in Section 2.1.3. In the Heliotest, dots are printed on a paper. Some of the dots can be missing since, for various reasons, the ink is not absorbing on to the paper perfectly. The distance from the beginning of the printed area to the 20th missing dot on the strip is an inspection property widely used in industry. Fig. 3.1 shows a detailed part of a strip.

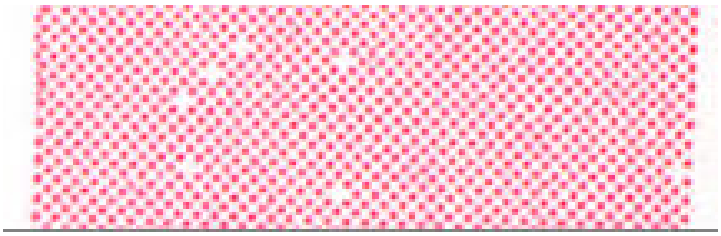

Figure 3.1: Part of a Heliotest strip, dots and some missing dots in the image are visible.

3.1 The Heliotest printability test

As discussed in Section 2.2, printability describes how well a paper reproduces the original artwork. The test is performed under standard atmosphere $23.0 \pm 1.0\ ^oC$ and $50 \pm 2\%$ rh. The test print is performed at $1 m/s$ with a special Heliotest ink. A formal description of how to perform the Heliotest is introduced in [36] as follows:

1. Starting from the side with the largest dots in the variable screen area count the missing dots until the 20th one.

2. Measure the distance in mm from the 20th missing dot to the beginning of the variable screen area.

3. In the case when the distance is very small (only a few millimetres) count the total number of missing dots in the four dotted lines on both sides of the variable half tone.

4. Repeat Steps 1 and 2 or 3 for each test strip.

5. Calculate the average and if required the standard deviation. In some cases it may be useful to mention the highest and lowest value as well.

6. If needed, assess the printing quality visually in the conventional screen area.

The different screen areas of a Heliotest strip are shown in Fig. 3.2 The half-tone area is produced by a printing disk that contains the dot pattern carved on the surface of the disk. The diameter of the carved dots remains the same throughout the disk but the depth changes in order to produce less intensive half tones. Deeper engraves produce darker tones and larger dots and shallower engraves produce lighter and smaller dots. The half-tone print produced by the printing disk is the area from which the 20th missing dot is measured and is therefore the most important part of the print.

A conventional screen area is used for general visual assessment of the printing quality. Although it is seldom used since it does not provide much information.

Two lines of dots on both sides of the half-tone area are used if the actual half-tone area contains too many missing dots right from the start. In that case, the total number of missing dots is calculated from these lines. This can happen if the paper is very rough. In practice, this information is very rarely used.

The use of this test as a good measure of printability has been called into question since the results obtained in laboratory tests with the Heliotest have not necessary correlated well with actual online printing results [73]. Nevertheless, the measure is important for the paper and printing industry.

3.2 Overall structure of the automated Heliotest method

This section gives an overview of how the missing atom (in the Heliotest images, missing dots) detection methods work. The first step when performing missing atom detection is image acquisition. It will be discussed in section 3.3. After the image has been acquired, it will be converted to grey level. Instead of using a linear conversion, a method based on Bayesian-decision making is used, resulting in much better contrast in the grey level image. The method is described in section 3.4.

The grey level image is then subjected to the 3 methods proposed in section 3.5. The basic idea behind missing atom detection from images comes from the properties of Fourier transform. The repeating pattern in the spatial image causes repeating peaks in the Fourier domain. By utilising this information the faultless repeating pattern of the original image can be obtained which can then be used to detect missing atoms from the original faulty image. Finally the proposed methods are tested in the experiments section 3.6.

3.3 Image acquisition

The requirements for image acquisition in the Heliotest are rather demanding due to the high resolution required. The diameter of an individual dot in a Heliotest sample is around 140 μm which dictates that the resolution of the image should be around 1200 dpi (dots per inch). At that resolution, the individual dots will be around 5-15 pixels in diameter, depending on which part of the Heliotest strip is acquired. The resolution level means aliasing is avoided since the dots form the highest frequencies in the Heliotest images and the dots themselves are not very sharp from the edges due to ink spreading into the paper.

Image enhancement based on colour information is performed in order to distinguish grey "dirt", such as dust, from the red printed dots. In laboratory conditions, a sufficiently accurate flatbed scanner can be used, but in practice, the samples may be wet with printing ink and therefore contact is not desirable.

3.4 Converting a colour image into a grey level image

After the half-tone screen area has been located from the input image, it is converted to a grey level image. Linear grey level conversion, however, introduces poor contrast in the resulting grey level image. So contrast enhancement is required in order to better distinguish dots from the background and "dirt". Ordinary conversion from a RGB image to a grey level, i.e. summing the individual channels and dividing by 3, introduces poor contrast in the grey level image between the dots and the background which in turn means that thresholding in later steps of image processing is difficult. Therefore a more suitable conversion method for the colour image to the grey level is required. This can be achieved by doing the colour conversion and contrast enhancement simultaneously, instead of consecutively. Fig. 3.3 demonstrates the difference between ordinary grey level conversion and the proposed method. If an image contains any unevenness in lighting, it should be compensated for before applying contrast stretching or colour image to the grey level image conversion.

The objective of contrast enhancement is to preprocess the image so that relevant information can be either seen immediately or processed further more reliably. These techniques are typically applied when the image itself or the device used for image representation provides poor visibility and characteristics of different regions of interest in the image. The reason for the poor representation can be a high dynamic range of pixel intensities when displays cannot reproduce them, a narrow dynamic range over the the regions of interest, or even incompatibility with the human observer. The most important application areas for contrast enhancement are medical imaging [98] and visualisation of images with a high dynamic range [70]. The enhancement is usually performed to produce a better representation for a human observer, but properly enhanced images can also enable more accurate and more reliable results in general image processing tasks, such as segmentation, due to an enhanced signal-to-noise-ratio.

A reversible and fast contrast enhancement is often preferred, e.g., in medical imaging. Therefore, the methods typically exploit histograms. The histogram can be multidimensional, such as a 3-D colour histogram, but most methods assume a 1-D histogram is

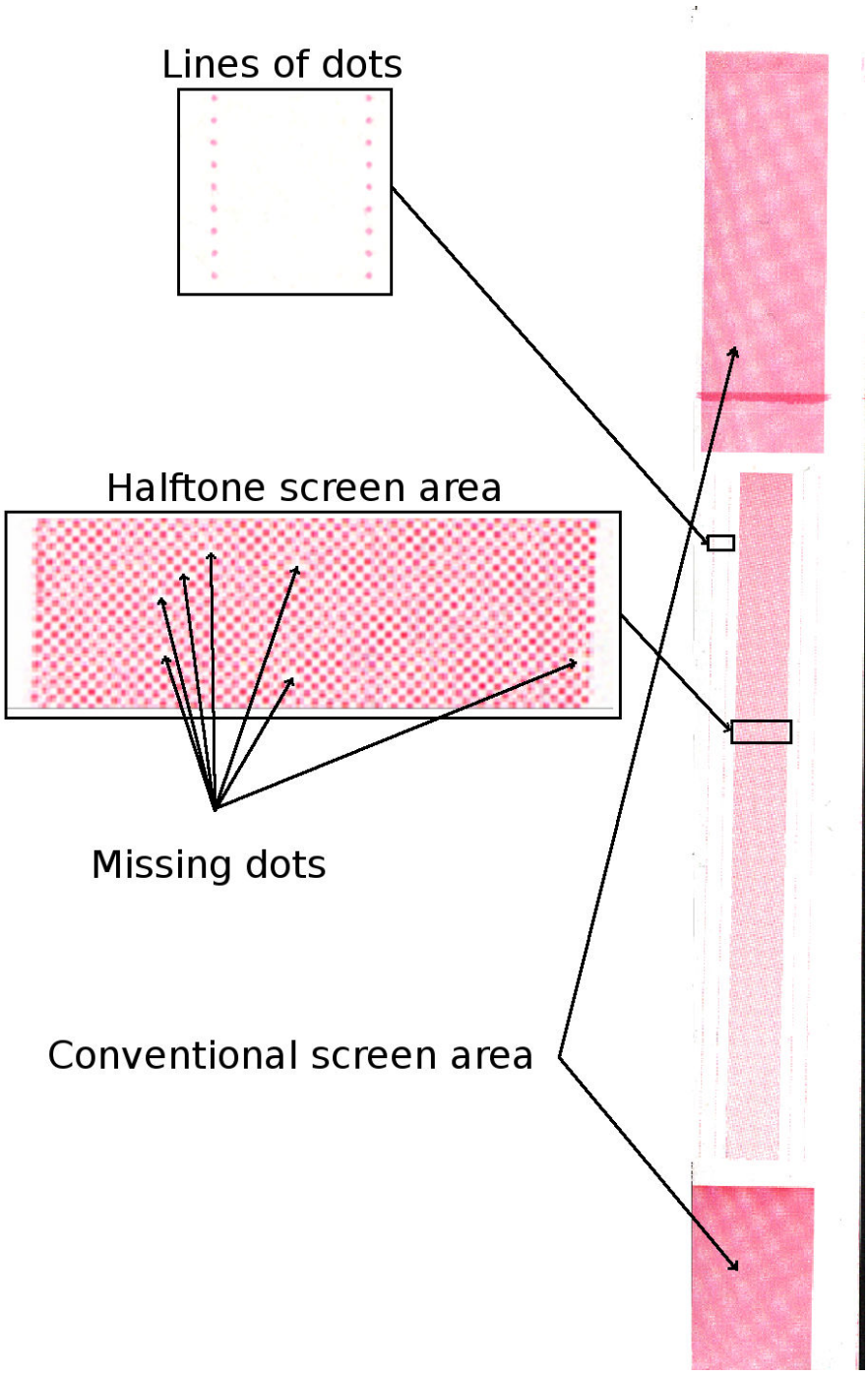

Figure 3.2: Detailed description of Heliotest print.

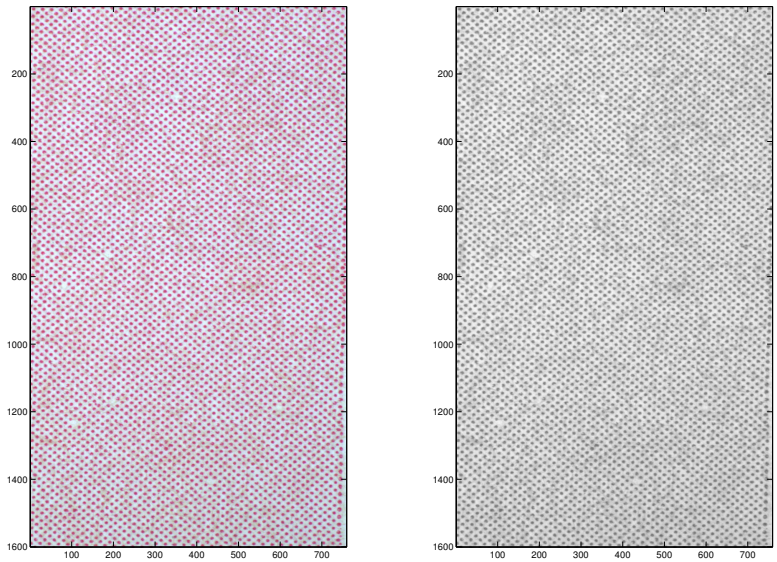

(a) (b)

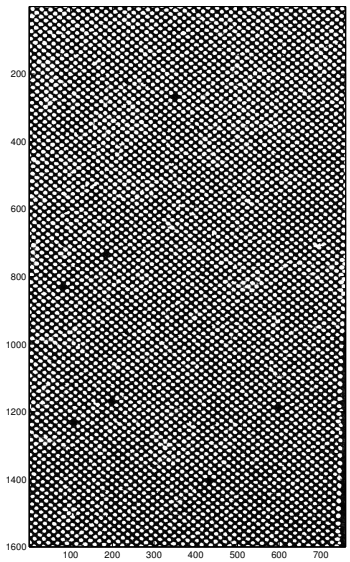

(c)

Figure 3.3: Example of colour enhancement: a) Original RGB image; b) RGB image converted to grey level image; c) Original RGB image in gray level after contrast enhancement.

sufficient, resulting in separate processing of the colour components in the enhancement process. The baseline method for contrast enhancement is histogram equalisation [25, 35], but the method does not utilise any information about which regions should be emphasised. This "blind" equalisation often leads to a representation where image noise is amplified, and the properties aiding separability of different image regions decline [98]. The amplification of noise may be avoided to some extent by local processing [98], but an undesired result is the loss of rank order of image intensities. It seems that estimation of the background and foreground, either manually or automatically, is necessary for successful contrast enhancement. Manual estimation would make the solution trivial, but automatic estimation still remains a challenging problem. Automatic estimation may be based solely on the intensity information, or it can include also analysis of spatial relationships.

Actual contrast enhancement is based on stretching the perceivable dynamic range between the estimated regions (visual enhancement). In visual enhancement, pseudo colouring [82] or multiple images are used to artificially emphasise the contrast [70]. The use of multidimensional data is, however, difficult for many image processing techniques, such as frequency- or scale-space methods. Therefore, multi-representation is generally a good solution only for visualisation purposes.

In this section, colour conversion and enhancement is presented as a method to project N-dimensional image data to a 1-dimensional (grey-level) image which possesses a maximal contrast between the foreground and background. The main reason for the grey-level image representation is to allow the use of standard image processing techniques, even though it can also be used for visualisation purposes. In the simplest case, the image is bi-modal, i.e., there are two regions of interest. In this case, the maximal contrast is achieved by binarisation. Binarisation, however, does not provide optimal contrast due to the presence of noise. To achieve better contrast, Bayesian inference and posteriori values are utilised in the enhancement. Similar approaches have been used, for example, in thresholding [49] and colour segmentation [72]. The proposed colour conversion and contrast enhancement is analytically studied with simulated data, and the efficiency is also demonstrated with real images.

3.4.1 Colour to grey conversion and contrast enhancement

Successful contrast enhancement produces an output image where the dynamic range of output space values is organised to emphasise the separation between regions of semantically different classes. It should be noted that there exists no definition for optimal contrast enhancement, but the desired result depends on the application. A similar but more unambiguous problem is image segmentation in which regions of similar characteristics (texture, colour, etc.) should be automatically labelled with the same label. For instance, in colour segmentation it is assumed that different colours belong to different semantic regions. The input space, typically the RGB or HSI colour space, is mapped to discrete colour labels, and if the assumption holds, desired regions, such as the human skin may be revealed [72].

An optimal output space for the contrast enhancement cannot be defined either: some methods, such as histogram equalisation, work on the grey level histogram domain and

produce a new representation within the same domain, while other methods produce an index labelled representation (pseudo colouring) or even multiple images.

The next part to be addressed is a specific mapping problem where an N-channel input image (e.g., $N = 1$ for grey-level images, $N = 3$ for RGB images) is mapped to a 1-D representation where the maximal contrast is optimised between M different regions of interest. The mapping of M different regions into a single variable is a distinct problem, and it will be evident that the posteriori contrast, as it will be defined, provides the minimum error only as biased by the selected mapping method. How the biased error relates to the true error is an information theoretic problem dealing with how the region data should be optimally coded into a single variable. The true error can be achieved only in the bi-modal case ($M = 2$). is generalisable to any number of regions M, however.

3.4.2 The bi-modal image model

In the bi-modal image model, there are two different regions of interest, ω_0 and ω_1, in the image $f(x, y)$ where $f : (x, y) \rightarrow \vec{x}$. The output space values $\vec{x}$ of the two regions vary with respect to probability distributions $p(\vec{x}|\omega_0)$ and $p(\vec{x}|\omega_1)$, and the covered area of the two regions is defined by a priori probabilities $P(\omega_0)$ and $P(\omega_1)$. Since the maximal contrast can be achieved only by a representation where no ambiguity exists between the two regions, the maximal contrast for the bi-modal image model corresponds to a binary representation, e.g.,

$$\vec{x} \rightarrow \begin{cases} 0, \text{if } \vec{x} \in \omega_0 \\ 1, \text{if } \vec{x} \in \omega_1 \end{cases} . \tag{3.1}$$

Symbols 0 and 1 are selected here just for convenience – any other two different symbols agree with the definition. For a bi-modal image, the optimal contrast enhancement would produce a representation where the pixels belonging to the region ω_0 are denoted by one symbol, and the pixels belonging to the region ω_1 by another symbol.

It is clear that the maximal contrast can be obtained by using binary thresholding methods. However, if the distributions of the two classes overlap, thresholding provides also the maximal error for a single pixel if a wrong decision has been made. Thresholding does not generally provide the minimum-error maximal contrast.

For image $f : (x, y) \rightarrow \vec{x}$ where for all spatial points (x, y) the minimum error for contrast is obtained by Bayesian inference if the conditional probability density functions of the classes, $p(\vec{x}|0)$ and $(\vec{x}|1)$ and a priories of both regions $P(0)$ and $P(1)$ are known as follows

$$\vec{x} \Rightarrow \begin{cases} 0, \text{ if } p(x|0)P(0) \geq p(x|1)P(1), \\ 1, \text{ if } p(x|0)P(0) < p(x|1)P(1) \end{cases} . \tag{3.2}$$

The Bayesian rule guarantees minimum error in binarisation, and by following this principle Kittler and Illingworth defined a method to select the optimal threshold value assuming normal distributions for $p(\vec{x}|0)$ and $p(\vec{x}|1)$ [49].

If binary representation is assumed, the Kittler and Illingworth method can in this context be referenced as the minimum-error maximal contrast. It is clear that there exists a confusion factor in the binary Bayesian decision. For example, when the posteriories of

both regions are 0.5, the decision favouring 0 would not be the optimal decision. Binarisation does not allow utilisation of the confidence information, but if the non-maximal contrast by the real number space is sufficient, the confidence can be embedded into the contrast description. For values between $[0, 1]$, the minimum-error decision corresponds directly to the posteriori values [15] as shown below. Since 0 now represents strong certainty of the region ω_0 and ω_1 of 1, the posteriori of either region can be selected. In order to maximise the contrast, the value that minimises the error function

$$\underset{V(\vec{x})}{\operatorname{argmin}}\ error\ \forall \vec{x} \tag{3.3}$$

where *error* is the expectation of squared error in thresholding defined as

$$error(\vec{x}) = P(0|\vec{x})(V-0)^2 + P(1|\vec{x})(1-V)^2 \tag{3.4}$$

where V and $1-V$ are the posteriori values obtained by Bayesian decision. *error* is minimised if $V = P(1|\vec{x})$. By writing the equation into the form

$$error(\vec{x}) = V^2 + (2P(0|\vec{x}) - 2)V + 1 - P(0|\vec{x}) \tag{3.5}$$

and differentiating it regarding V and setting gradient to 0, the result is the minimum of the *error* function.

$$V = 1 - P(0|\vec{x}) = P(1|\vec{x}) \tag{3.6}$$

Therefore for a bi-modal image model, the posteriori values provide the true minimum error contrast in a mean square sense. Since this applies to all pixels in an image, the mean squared error (MSE) can be computed as

$$MSE = \frac{\sum_x \sum_y error(\vec{x})}{\sum_x \sum_y 1}, \tag{3.7}$$

where $\sum_x \sum_y 1$ is the number of pixels in an image. The benefit of this methods is that unlike in equation 3.2 instead of thresholding an image into crisp 1 or 0, unclear pixels get a value between $[0, 1]$.

3.4.3 Estimating probability distributions

Before the presented results can be applied, the distributions and their parameters, $p(\vec{x}|\omega_i)$ and $P(\omega_i)$, for different regions of interest must be estimated. Only one assumption is made, the assumption by Kittler and Illingworth is generalised and it is assumed that the probability densities $p(\vec{x}|\omega_i)$ are multivariate normal distributions. If no prior knowledge of the distribution type is available, the multivariate normal distribution provides a good general solution playing a predominant role in many areas of mathematics [86].

The expectation maximisation (EM) algorithm was applied [69] for the estimation of M normal distributions in N-dimensional input space.

3.5 Feature extraction and detecting missing dots

As can be seen from Fig. 3.1, Heliotest samples consist of a regular texture pattern. The three basic ways to describe texture are statistical, structural and spectral [23]. Statistical properties analyse the statistical properties of the points that comprise a surface in the image. Typically these point values are computed from grey level values, although colour information can also be used. The structural approach characterise texture as being composed of simple primitives called texels that are arranged on the surface according to some rule. The rule can be formally defined by some grammar. Spectral approaches are typically used for periodic 2D patterns in an image. The most commonly used spectral approach is the Fourier transform. Its properties can be used to describe periodicity of grey levels of a surface by identifying high energy peaks in the spectrum.

Since the Heliotest clearly presents a regular texture pattern, the most promising methods for detecting this regularity (and consequently irregularity) come from the spectral approach. Different spectral domain approaches can be, for example, Fourier transform, cosine transform and Gabor filters [24]. The methods were compared for applicability to the Heliotest in [76]. Based on those tests, and prior papers [88, 47] about using Fourier transform for regular pattern detection, Fourier transform was selected for further study.

In the article [30] the use of optical Fourier transform to detect missing dots from a raster pattern is proposed. In the article, an analytical model for obtaining Fourier transform from a raster pattern is derived. The model assumes that an image of an infinite size raster pattern is obtained through an aperture D millimetres wide. Fig. 3.4 compares magnitudes (absolute values of Fourier spectra) obtained by the analytical model with results obtained by applying FFT on an image with the same parameters. The difference in the images originates from the way they are obtained. The analytical model views an infinite raster pattern through a round aperture with finite size whereas FFT performs Fourier transformation on a rectangular image with finite dimensions. As can be seen from the image profiles in Figs. 3.4(d) and 3.4(e), both methods produce distinct peaks in the Fourier domain. These peaks define the repeating pattern in the spatial domain.

3.5.1 Pattern regularity

It is worthwhile to define terms dot and pattern in this context. A dot is a particular type of texture atom; an indivisible atom which can be represented for example by a 2-d Gaussian function. A pattern is a set of spatial coordinates in which dots are reproduced. When the pattern expresses some degree of periodicity it can be considered as regular. Similar definitions and results are used in solid state physics and in definitions of crystal lattice structures [3].

Regularity is a property which means that some mnemonic instances follow predefined rules. In the spatial domain, regularity typically means that a pattern consists of a periodic or approximately periodic structure of smaller pattern units or atoms, and thus, it is worthwhile exploring pattern regularity in terms of periodical functions and especially via their Fourier transforms. The following is mainly based on definitions in solid state physics and is related to Bravais lattice formulations: A Bravais lattice is an infinite array of discrete points with an arrangement and orientation that appears exactly the

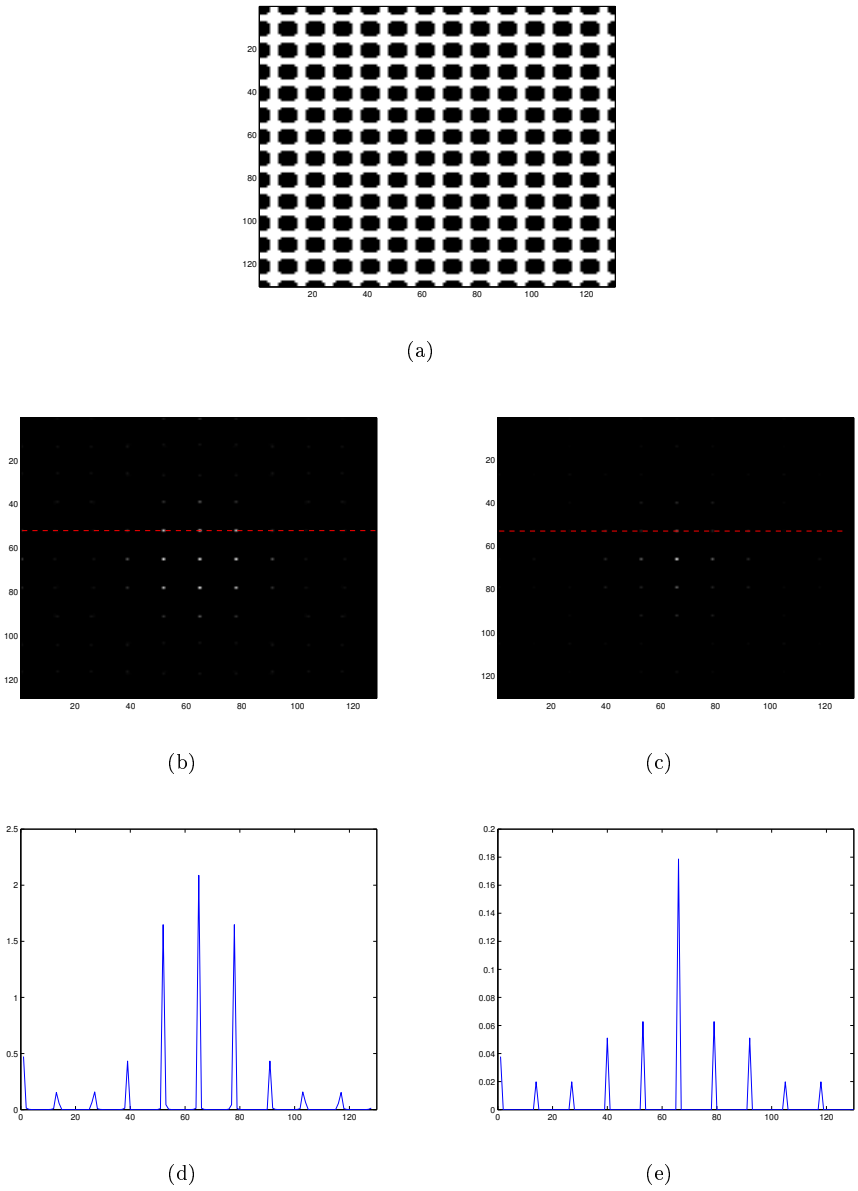

Figure 3.4: Comparison of Fourier transform obtained analytically and by using FFT. (a) Rater pattern to which Fourier is applied; (b) Analytically obtained Fourier magnitude in logarithmic scale; (c) Numerically obtained Fourier magnitude in logarithmic scale; (d) Image profile along the dashed line in Fig. 3.4(b); (e) Image profile along the dashed line in Fig. 3.4(c)

same from whichever of the points the array is viewed. A two-dimensional (2-d) Bravais lattice consists of all points with position vectors $\mathbf{R}$ of the form

$$\mathbf{R} = n_1\vec{a}_1 + n_2\vec{a}_2 \tag{3.8}$$

where $\vec{a}_1$ and $\vec{a}_2$ are any two linearly independent vectors, and n_1 and n_2 range through all integer values. The vectors $\vec{a}_i$ are called primitive vectors and are said to generate or span the lattice. It should be noted that the vectors $\vec{a}_i$ are not unique. Fig. 3.5 shows a part of a two-dimensional Bravais lattice [3].

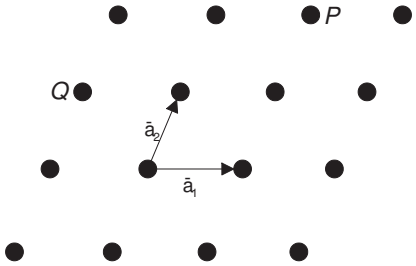

Figure 3.5: A two-dimensional Bravais lattice of no particular symmetry, an oblique net. All the net points are linear combinations of two primitive vectors (e.g. $P = \vec{a}_1 + 2\vec{a}_2$, and $Q = -\vec{a}_1 + \vec{a}_2$).

The definition of a Bravais lattice refers to points, but it can also refer to a set of vectors which represent another structure. A point as an atom can also be replaced with any, preferably locally concentrated, structure. A region which includes exactly one lattice point is called a primitive unit cell and $\vec{a}_i$ now defines the spatial relationship of the unit cells [3]. Unit cells can also be defined as non-primitive but in both cases they must fill the space without any overlapping. The primitive and non-primitive unit cells are not unique.

3.5.2 Fourier transform of 2-d periodic functions

Let us consider a function $f(\vec{r})$ (where $\vec{r} = (x, y)$) in which the spatial domain is a periodic extension of a unit cell. Periodicity can be formally described. Let M be a 2×2 matrix which is invertible and such that

$$f(M\vec{m} + \vec{r}) = f(\vec{r}) \tag{3.9}$$

where $\vec{m}$ is any 2-dimensional integer vector Now, clearly, every point $\vec{r}$ in the space can be written uniquely as

$$\vec{r} = M(\vec{n} + \vec{u}) \tag{3.10}$$

where $\vec{n}$ is a 2-dimensional integer vector and $\vec{u}$ is a vector where each coordinate satisfies $0 \leq u_i < 1$. A unit cell $\mathcal{U}(M)$ is the region in space corresponding to all points $M\vec{u}$. It can be shown that the volume of a unit cell is $V = |\det M|$.

The set of all points $\mathcal{L}(M)$ of the form $M\vec{n}$ is called the lattice induced by M. A point in the space corresponds to a point in the unit cell translated by a lattice vector. Note that a sum of two lattice vectors is a lattice vector and the periodicity of function f implies that its value is invariant under translations by multiples of the lattice vector. A matrix $\hat{M}$ can be obtained by inverting and transposing M

$$\hat{M} = M^{-T} \ . \tag{3.11}$$

For $\hat{M}$ a new lattice and unit cell can be associated, called the reciprocal lattice $\mathcal{L}\left(\hat{M}\right)$ and the reciprocal unit cell $\mathcal{U}\left(\hat{M}\right)$, respectively. If we consider wave number space, each vector $\vec{k}$ is written uniquely as

$$\vec{k} = \hat{M}\left(\vec{\kappa} + \vec{\xi}\right) \tag{3.12}$$

where $\vec{\kappa}$ is a 2-dimensional integer vector and $\vec{\xi}$ any real vector whose ordinates $0 \leq \xi_i < 1$. The reciprocal lattice vectors span the lattice points $\hat{M}\vec{\kappa}$.

The fundamental result is that Fourier transform of a periodic function with a unit cell specified by M has a discrete spectrum, with peaks located at the reciprocal lattice points specified by $\hat{M}$ [3]. That is, the wavenumber vectors are constrained to lie at the reciprocal lattice points. The explicit transform and inverse transform formulas are

$$\hat{f}_M\left(\vec{k}\right) = \frac{1}{|\det M|}\int_{\vec{r}\in\mathcal{U}(M)} f(\vec{r})\, e^{-j\left(\vec{k}\cdot\vec{r}\right)} dV(\vec{r}) \ , \ \vec{k} \in \mathcal{L}\left(\hat{M}\right) \tag{3.13}$$

and

$$f(\vec{r}) = \sum_{\vec{k}\in\mathcal{L}\left(\hat{M}\right)} \hat{f}_M\left(\vec{k}\right) e^{j\vec{k}\cdot\vec{r}} \ . \tag{3.14}$$

The discrete spectrum can be interpreted as a continuous spectrum consisting of Dirac impulse functions located at the reciprocal lattice points

$$\hat{f}\left(\vec{k}\right) = \sum_{\vec{\kappa}\in\mathcal{Z}^D} \hat{f}_M\left(\hat{M}\vec{\kappa}\right)\delta\left(\vec{k} - \hat{M}\vec{\kappa}\right) \ . \tag{3.15}$$

3.5.3 Fourier transform of 2-d approximately periodic functions

In a more general case we can take a 2-d image which is only approximately periodic. Consider a pattern image whose unit cell and lattice structures are specified by M. If this image is unbounded in all directions and we can consider a function which is periodic (i.e., invariant under translation by a lattice vector), then the superposition of waves whose wavenumber vectors are necessarily precisely lattice vectors in the reciprocal lattice, specified by $\hat{M} = M^{-T}$.

However, a real image has a finite extent and has imperfections (irregularities). The ideally periodic function is constrained to satisfy certain boundary conditions. The consequences of this is illustrated by considering a situation where the pattern is comprised

only of a finite number of translates of the unit cell. Let V denote the finite region occupied by the pattern, and consider the window function $w_{\mathcal{V}}(\vec{r})$ defined as

$$w_{\mathcal{V}}(\vec{r}) = \begin{cases} 1, & \vec{r} \in \mathcal{V} \\ 0, & \text{otherwise} \end{cases} \tag{3.16}$$

If $f(\vec{r})$ is the ideal, the truly periodic function (with periodicity specified by M) and $f_{\mathcal{V}}(\vec{r})$ is the truncated function

$$f_{\mathcal{V}}(\vec{r}) = w_{\mathcal{V}}(\vec{r}) f(\vec{r}) = \begin{cases} f(\vec{r}), & \vec{r} \in \mathcal{V} \\ 0, & \text{otherwise} \end{cases} \tag{3.17}$$

then $f_{\mathcal{V}}(\vec{r})$ has a continuous spectrum given by

$$\hat{f}_{\mathcal{V}}\left(\vec{k}\right) = \sum_{\vec{\kappa} \in \mathcal{Z}^2} \hat{f}_M\left(\hat{M}\vec{\kappa}\right) \hat{w}_{\mathcal{V}}\left(\vec{k} - \hat{M}\vec{\kappa}\right) \tag{3.18}$$

where $\hat{w}_{\mathcal{V}}$ is Fourier transform of $w_{\mathcal{V}}$.

It can be shown that $\hat{w}_{\mathcal{V}}$ contains a continuous spectrum which has infinite extent but which fades out with $1/\left|\vec{k}\right|$.

The most important result is that approximatively periodic functions have approximatively discrete spectra, with the spectral energy concentrated at points in the reciprocal lattice.

3.5.4 Pattern irregularity

In terms of function periodicity, pattern irregularity can be defined as an aperiodic function $\varepsilon(x, y)$, with spatial energy $|\,\varepsilon\,| \ll |\,f_{\mathcal{V}}\,|$.

Finally, the initial 2-d pattern image can be represented as

$$f_{\mathcal{V}}(\vec{r}) = w_{\mathcal{V}}(\vec{r}) f(\vec{r}) + \varepsilon(\vec{r}) \tag{3.19}$$

and the problem is to separate the regular part $w_{\mathcal{V}}(\vec{r}) f(\vec{r})$ and the irregular part $\varepsilon(\vec{r})$ as accurately as possible.

3.5.5 Extracting the regular pattern information

As was described in the previous section, the formation of the model of the ideal regular part of an image is crucial for irregularity detection; the more accurate the model that can be established the more accurate and detailed the detection that can be made.

The details level needed for the regular part formation is particularly high, for example, in Heliotest images [76], and thus, typical texture segmentation methods (e.g. [28]) or defect detection methods (e.g. [12]) cannot provide sufficient accuracy. The user must be able to define the minimum deviation from the single ideal unit cell which is classified as an irregularity.

One attractive approach to estimate an ideal regular pattern is to derive an analytical model and to estimate model parameters based on an input image. This approach has been proposed, for example, in [12], but requires a precise and very accurate analytical model, in which case the parameter estimation may become very unstable and slow. Typically, real images do not correspond to analytical models but contain distortions and noise. For this reason it is motivated to use the analytical model only as a restricting bias in the regular pattern formation and allow incompleteness by extracting the regular pattern from an input image itself. This approach has been applied in frequency domain self-filtering to emphasise regular patterns [4] and will be the case in the approaches proposed in this thesis as well. Results from the regular lattices and the reciprocal lattice are applied, but only to estimate appropriate model parameters, while details are extracted from an input image. Factors which affect to the selection of this approach will be discussed next.

3.5.6 Spatial modelling limits of accuracy

Before considering how to extract the ideal regular pattern from an input image, it is important to explain why all parameters of the analytical model cannot be directly estimated. Analytical models would be the most obvious solutions since they are commonly used in regular dot pattern synthesis, e.g., in digital half-toning [45], and also used for defect detection (e.g. [12]). In the context of regular dot patterns the analytical expression in (3.19) can be used, but the limits of accuracy prevent estimation of the model parameters directly because of practical restrictions due to the discrete image resolution which cannot be bypassed. For the same reason, the limited available resolution, a half tone synthesis is not necessarily reversible.

Fig. 3.6(a) shows a simplified model of a regular dot pattern which can also be used to describe the pattern in Heliotest assessment [73, 76]. Parameters of the model can be divided in the following classes:

1. Image geometry parameters, i.e., lattice primitive vectors $\vec{a_1}$, $\vec{a_2}$ (see Fig 3.6(a)) and the overall lattice shift vector $\vec{s}$.

2. Unit cell model parameters. In the case of the Heliotest it can, for example, be a 2-d Gaussian hat (see Fig 3.6(b)).

Estimation of all the above-mentioned parameters is necessary in order to generate an accurate ideal regular pattern model which can be used in irregularity detection by comparing or subtracting it from the observed image. However, the estimation is not trivial; it can be performed with search or generic optimisation methods where a target function to be minimised is, for example, energy difference between the observed image and the model. Unfortunately the number of parameters to be optimised is very high and they cannot be independently optimised.

The first step in the pattern modelling is estimation of the lattice parameters $(\vec{a_1}, \vec{a_2})$ representing periodicity (lattice matrix M). These parameters can be derived using a number of techniques: using image autocorrelation space, image texture statistics (grey-level statistics), LBP (local binary pattern [64]), fixed window features, etc. Problems

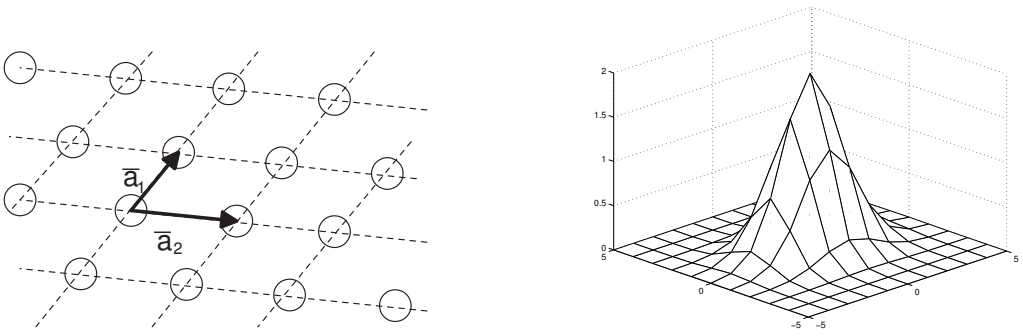

(a) (b)

Figure 3.6: Simple model of a regular dot pattern (Heliotest): (a) 2-d lattice structure ($\vec{a_1}, \vec{a_2}$ - primitive vectors); (b) Gaussian dot model (μ, Σ, A).

may arise, during periodicity estimation such as incorrect period estimation (convergence to harmonics nM instead of M). A solution for the periodicity ambiguity is a correct initial period guess. For example, in the Heliotest proper, limits of the search domain for vectors $\vec{a_1}, \vec{a_2}$ must be defined. This approach depends on the input image and further generalisation seems to meet with low success.

It is also possible to estimate the parameters using statistical tools: the mean lattice matrix M_μ and lattice matrix deviation M_Σ. The question arises, whether the mean lattice matrix can be used as a model of the ideal lattice. Practical experiments, unfortunately, showed that it cannot; the observed lattice from an input image is typically not regular enough and therefore it should be modelled rather as a real world stochastic process. Also, as the input images are large, over 1500 pixels in length, even a slight parameter estimation error can divert the estimated lattice points way off near the edges of the image, even when they are correct at the beginning of the image. The only possible way of using this modelling approach would be a local refining where each lattice grid point is adjusted to a corresponding unit cell in the observed image. This in turn would cause additional computational expenses which would prevent an efficient implementation of the method. Furthermore, it should be noted that additional model parameters introduce more uncertainty and more adjustment is then required.

It is evident that it is easy to construct a mathematical model to synthesise regular dot patterns, but this process is often irreversible in practice due to the limited acquisition resolution and exhaustive computation needed in the parameter estimation. With the help of application specific heuristics, a combination of direct estimations and optimisation may still succeed, but whether it is accurate and computationally feasible is questionable. Thus a more general, re-useable, and sufficiently accurate approximation technique is needed.

3.5.7 Exploiting Fourier domain

Let us now consider real images which represent regular dot patterns. Such images are produced by the Heliotest assessment as shown on the left-hand-side of Fig. 3.7. Next consider Fourier spectra of the given image, i.e., the magnitude spectra. On the right-hand-side of Fig. 3.7 it is possible to see the distinctive frequency peaks located at the reciprocal lattice points in Eq. 3.13. Since no special window function is used to preprocess the original input image, and due to the fact that the images are discrete, the frequency peaks can leak energy to adjacent frequencies, mostly perpendicular to the running directions of the spatial patterns. This happens when the pattern does not continue flawlessly on image edges. This energy leakage gives the peaks a "star like" shape, visible on the right-hand-side of Fig. 3.7. The leak direction depends on the amplitude difference on the image edges when they are wrapped around. By windowing the input image with, e.g., the Hamming window function, this energy leakage would diminish, but the peaks would also blur, making it more difficult to detect the repeating peak locations accurately. However, if the number of individual image atoms that form the regular pattern in the spatial domain is small, then a proper windowing could be applied to better distinguish separate peaks from Fourier spectra.

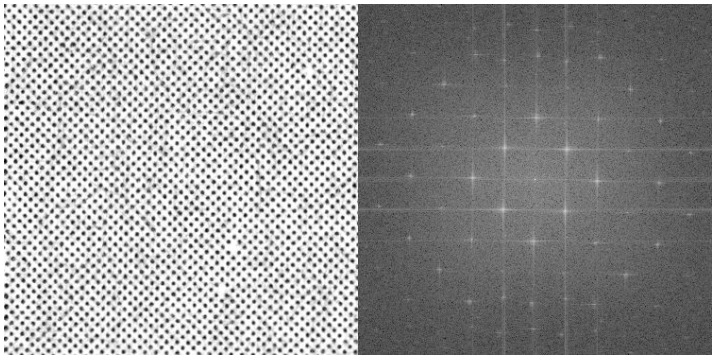

Figure 3.7: Example of regular dot pattern image (Heliotest) and its Fourier spectra magnitude.

It is clear that by filtering out all the other frequencies except the reciprocal lattice frequencies it is possible to estimate the faultless periodic component, the ideal regular pattern, of the input image and by utilising this component also the defect component, the irregular part. These two parts are now called as the regular and irregular parts of the image and demonstrated in Fig. 3.8. It should be noted that effects of image borders in Fig. 3.8 appear since the borders are discontinuity points. Separation of the parts can be formulated as

$$\begin{aligned} \xi(x,y) &= \mathfrak{F}^{-1}\{\Xi(u,v)\} = \\ &= \mathfrak{F}^{-1}\{\mathfrak{M}(u,v)\Xi(u,v) + (I(u,v) - \mathfrak{M}(u,v))\Xi(u,v)\} = \\ &= \underbrace{\mathfrak{F}^{-1}\{\mathfrak{M}(u,v)\Xi(u,v)\}}_{\text{regular part}} + \underbrace{\mathfrak{F}^{-1}\{(I(u,v) - \mathfrak{M}(u,v))\Xi(u,v)\}}_{\text{irregular part}} \end{aligned} \tag{3.20}$$

where $\xi(x, y)$ is the spatial image, $\Xi(u, v)$ is the Fourier domain image, $\mathfrak{F}$ and $\mathfrak{F}^{-1}$ are forward and inverse discrete Fourier transforms, $\mathfrak{M}(u, v)$ is a mask filter (real valued function of the same definition domain as $\Xi(u, v)$), and $I(x, y)$ is a unit function. The decomposition in Eq. 3.20 is possible because Fourier transform and its inverse are linear operators. The mask filter can be of any type suitable for a particular application, i.e., accept/reject (binary), notch filter, etc. The only condition for the mask is that it should include the periodic component while removing other frequencies, i.e., it should have band-pass on frequencies near the reciprocal peak points.

The effect of white (Gaussian) noise in a spatial image does not have a harmful effect on the Fourier image, the energy of the noise will spread evenly on all frequency bands, leaving the repeating peaks still clearly visible, provided that the noise amplitude is not strong enough to mask the repeating peaks. Random noise in an image has a random pattern in the Fourier domain and is application dependant. If it is a problem, should dealt with in the preprocessing steps. Patterned noise in a spatial image, however, has distinct peaks in Fourier domain, and should be dealt in preprocessing if the noise is a problem.

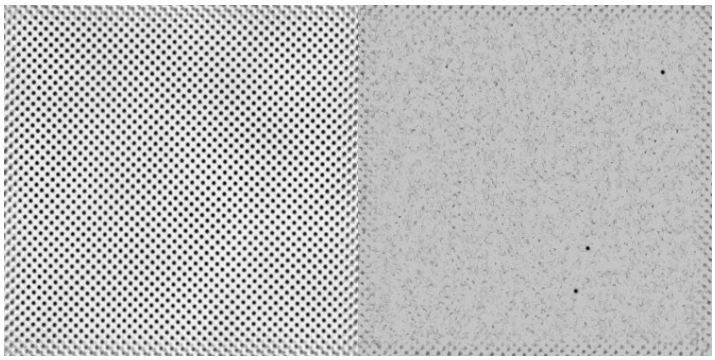

Figure 3.8: Examples of regular and irregular image parts (Heliotest).

3.5.8 Spatial domain vs. Frequency domain

Many image processing techniques work well directly in the spatial domain. However, with repetitive patterns, the choice of frequency domain is obvious. Using the FFT algorithm, forward and inverse Fourier transforms can be made efficiently and fast. 2-d periodicity in the spatial domain is given by a lattice matrix M and a 2-d periodic function in the frequency domain has discrete spectra located at the reciprocal lattice M^{-T} points. For an $N \times N$ image the FFT transform is also $N \times N$ with discrete frequencies ranging from 0 to $(N-1)/N$ (wave numbers $0, \ldots, N-1$). If the input image pattern contains a large number of unit cell translations, the frequency picture will be sparse, having a small number of lattice points in it. Consequently, rough estimation of lattice matrix M through a reciprocal matrix M^{-T} is easier.

Inspecting small details, such as the shape of a single unit cell, is a difficult task in the Fourier domain, and inverse transform back to the spatial domain is needed in detailed

analysis. These issues will be discussed in the next section in the description of the proposed algorithms.

Aliasing can happen during image acquisition if the repeating details are not imaged with sufficient detail. This problem occurs if the sampling frequency is lower than the Nyquist sampling rate. Once again this is an application specific problem and if needed, proper anti-aliasing methods should be applied. After an image has been obtained, no further aliasing problems can occur. Because the images are finite, they are band limited in nature and therefore Fourier transformation can not produce higher frequencies than already apparent in the image.

3.5.9 Method 1: Fourier domain regularity detection and global grey-level processing in the spatial domain

This method (referred to as Method 1) is based on the fact that the periodic regular structure provides intensity peaks in the Fourier domain, as demonstrated for the periodic function f and its reciprocal counterpart $\hat{f}$ in Eqs. 3.9 and 3.15 and shown in Fig. 3.7. If the mask $\mathfrak{M}$ can be automatically generated by utilising locations of the peaks in the frequency domain, regular and irregular parts of an image can be extracted using Eq. 3.20. It is possible to find irregularities from an irregular image by global processing, i.e., by thresholding a grey-level irregular image and then processing the binary areas (see the right-hand-side in Fig. 3.8). The following stages are needed:

1. Image preprocessing to eliminate illumination changes and acquisition noise.
2. Extracting the irregular component by forming the mask based on the peak frequencies.
3. Global processing of the irregular image part.

Irregular component extraction

A general approach for irregular component extraction was established by introducing the theory of reciprocal lattices of periodic patterns in Section 3.5.1 and by the separation principle in Section 3.5.7. The extraction is described in Algorithm 1.

Algorithm 1 *Irregular image extraction*

1: *Compute magnitude of Fourier transform* $|\Xi|$ *of an input image* ξ.
2: *Form the reciprocal lattice vectors using locations of magnitude peaks.*
3: *Create the mask* $\mathfrak{M}$ *by setting Gaussian band-pass filters to reciprocal lattice points.*
4: *Extract the irregular component from* ξ *using the mask* $\mathfrak{M}$ *and the inverse Fourier transform as per 3.20.*

The first and last steps are clear enough, but the other two need more detailed description. The second step actually introduces the problem corresponding to the topic of this chapter: detection of regularity in regular dot patterns. The reciprocal lattice is defined by the primitive vectors, which can be estimated within a sub-pixel accuracy using the

peak locations, but the estimation may be sensitive to the initial guess. The estimation ambiguity occurs due to harmonic components, although it can be prevented by using a sufficiently accurate initial guess. Another ad hoc solution would be to locate all frequency peaks, but since the frequency plane is discrete, the harmonic set estimation based on lower frequencies is not accurate and the peaks need to be adjusted to actual local maxima. This adjustment is performed by looking for a local maximum in a certain neighbourhood. This neighbourhood can be defined as a rectangular area with the first approximation point in the centre and should contain only one local maximum from the harmonics set. It should be noted that estimation to sub-pixel accuracy is not needed since the regular pattern is finally extracted from the original image.

Filter mask generation is based on the reciprocal lattice and a band-pass filter suitable for an application. Without any prior information, the Gaussian succeeds as the general form. The width of the Gaussian can be estimated from the local peaks but again due to the use of the original signal in the regularity extraction, a fixed width can be safely used for efficiency. Two image components are derived from the observed image, one containing the regular image part and the other containing the irregular part. It should be noted that the algorithm tolerates arbitrary rotations and scalings.

Processing the irregular image

The irregular image produced by Algorithm 1 must be further processed to locate which irregularities are significant for the detection. The irregular image may still contain noise, which can be removed using standard noise removal methods, and following noise removal, processing of the irregular image can be defined according to Algorithm 2.

Algorithm 2 *Detecting irregularities from irregular image*

1: *Threshold the irregular image ξ_I using the threshold limit T.*
2: *Locate foreground areas of a size greater than S.*
3: *Compute centres of each foreground areas.*
4: *Return centres as irregularity coordinates.*

There are various methods which can be used to perform the binary processing tasks in Steps 2 and 3, e.g., areas of size less than S can be removed using the binary opening procedure [23]. Algorithm 2 requires two parameters to be defined: a threshold value T and the minimum area S. T can be obtained for example as:

$$T = \text{mean}(\xi_I) + n \ \text{std}(\xi_I) \tag{3.21}$$

where the mean is used to calculate the mean of the irregular image ξ_I grey level values and std to calculate standard deviation of irregular image grey level values. The grey level histogram of ξ_I is assumed to follow Gaussian distribution and therefore parameter n defines the confidence interval inside which pixels are determined to belong to the background, i.e., they are not considered as missing dots. The regular image can be used as a training set to obtain good values for the minimum area S. By thresholding the regular image ξ_R using for example Otsu's [68] standard method, the dots can be segmented and then their average or median size calculated and used to define parameter

S. A constant value for S can be used if the individual dots in the image are roughly the same size. For the Heliotest this can be achieved by analysing the image in parts which contain roughly equal sized dots.

3.5.10 Method 2: Fourier domain self-filtering

Method 2 is based on frequency domain self-filtering [4]. In this approach, the frequency image itself defines the filter. If $\Xi(u, v)$ is the Fourier transform of an image $\xi(x, y)$, the filter $\mathfrak{M}_2(u, v)$ is the magnitude of the frequency image, i.e.,

$$\mathfrak{M}_2(u, v) = |\Xi(u, v)| \tag{3.22}$$

Depending on the frequency content of the original data, it might be appropriate to emphasise the high frequencies by applying

$$\mathfrak{M}_3(u, v) = \sqrt{u^2 + v^2}|\Xi(u, v)| \tag{3.23}$$

To enhance the relatively smaller peaks at higher frequencies, the following filter can be used.

$$\mathfrak{M}_4(u, v) = log(1 + \sqrt{u^2 + v^2}|\Xi(u, v)|) \tag{3.24}$$

It equalises the relative differences between high peaks at lower frequencies and smaller peaks at higher frequencies and therefore makes the resulting regular image sharper.

After the given image is filtered in the frequency domain, the regular and irregular image parts can be converted to the spatial domain by using the inverse Fourier transform. Thus the regular image part contains the repeating pattern and the irregular image part contains nothing but the irregularities and some noise. Once the regular and irregular image parts have been separated, Method 2 proceeds exactly like Method 1: the irregular image is thresholded, and binary areas larger than S are considered as missing dots.

It should be noted, however, that the method can suffer if proper windowing is not used. With the rectangular window used in the work, the repeating peaks in the Fourier domain leak energy to nearby frequencies and can thereby mask the irregular (missing dots) information that is located between the regular peaks. The most important property of the method is that it emphasises a pattern that is dominating in an image. For the Heliotest this is desirable since the most dominant repeating pattern in a Heliotest image is the ink dot pattern. With a sufficient number of repeating atoms of an input image, the method performs well enough despite the energy leakage. Because the reciprocal peaks are much stronger than the background, the method attenuates the reciprocal peak locations more than their surroundings and therefore emphasises the repeating pattern in the spatial domain.

3.5.11 Method 3: Fourier domain regularity detection and local grey-level processing in the spatial domain

This approach (referred to as Method 3) can be divided into the following steps:

1. Regular spatial lattice points estimation.
2. Local classification at spatial lattice points.

Spatial lattice estimation

Spatial lattice estimation corresponds to the estimation of irregularities in the regular part, and thus, Algorithms 1 and 2 can also be used to find centroids of the unit cells. The only difference is that the regular image part is used instead of the irregular one. When all the centroids of the regular image part have been located, the original image can be processed and analysed at each unit cell location.

Local classification at spatial lattice points

The locations of the unit cells can be extracted using the regular image and next the decision whether it is regular or irregular, not missing or missing can be made at the each location (see Fig. 3.9). First, some kind of feature extraction is needed, e.g., simply the vector of all grey-level values. After feature extraction, the features are classified using a classifier. There are a vast number of applicable methods available and for vectors of grey-level values a principal component subspace classifier was used [67]. The principle of the classifier is simple. The feature vectors are projected into a subspace so that the subspace basis vectors are orthonormal. The training features are treated the same way. Classification is performed by calculating the distance between subspace data of the features with respect to the training data subspaces. It should be noted that a separate training set is needed in this approach, but the local processing approach can also provide detailed information about the type of missing dots.

Figure 3.9: Examples of dots in Heliotest images: (a)-(c) Regular dots; (d) Regular dot expectation; (e)-(g) Missing dots; (h) Missing dot expectation (note that not completely missing).

3.6 Experiments

In the experiments the image enhancement method introduced in Section 3.4 was evaluated and the three proposed methods for detecting irregularities were tested.

3.6.1 Colour image conversion to grey level

To demonstrate the method both quantitatively and visually, RGB colour space was selected as the image output value $\vec{x}$. An image is generated by placing two random points into the 3-D RGB space, assigning every image pixel to one of the points with respect to fixed a priori values $P(0)$ and $P(1)$, and applying colour space noise based on fixed normal distributions $p(\vec{x}|0)$ and $p(\vec{x}|1)$ to the pixels. To test the effect of distance and variance of points in colour space, the points can be repeatedly generated from uniform distribution with varying distance and variance parameters.

Two images with different parameter values are shown in Fig. 3.10. It should be noted that the covariance is a diagonal with fixed variance in all dimensions.

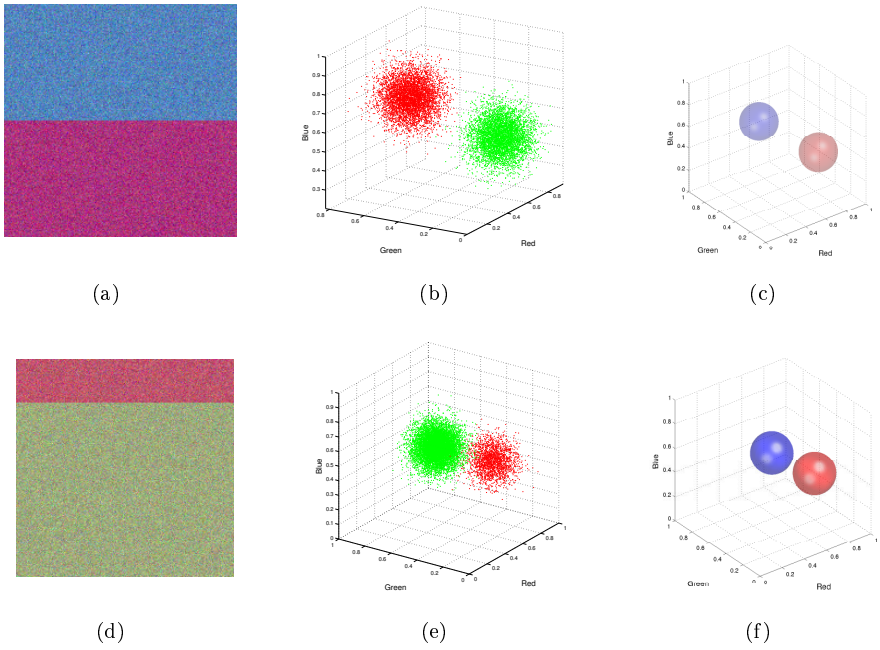

(a) (b) (c)

(d) (e) (f)

Figure 3.10: Generated bi-modal image data in the spatial domain (left), generated points in RGB space (middle), and EM-estimated distributions (right); (a),(b),(c) $P(0) = 0.5$, $P(1) = 0.5$, $\mu_0 = [85, 134, 191]/256$, $\mu_1 = [174, 52, 126]/256$, $\sigma_0 = 20/256$, $\sigma_1 = 20/256$; (d),(e),(f) $P(0) = 0.2$, $P(1) = 0.8$, $\mu_0 = [192, 87, 111]/256$,$\mu_1 = [159, 172, 126]/256$, $\sigma_0 = 20/256$, $\sigma_1 = 20/256$.

The most popular general method to convert RGB data to a single variable image (grey-level image) is the standard RGB-to-grey transformation, obtained by $(I_{(x,y)} = R_{(x,y)} + G_{(x,y)} + B_{(x,y)})/3$, and one of the most successful maximum contrast (thresholding) methods is the minimum-error thresholding [49]. To compare the proposed minimum-error contrast enhancement, where the calculated posteriori values are directly used as the grey level image, the MSE behaviour of these methods was studied for the generated data. The results are demonstrated in Fig. 3.11. The MSE is calculated with respect to the perfect maximal contrast image (binary).

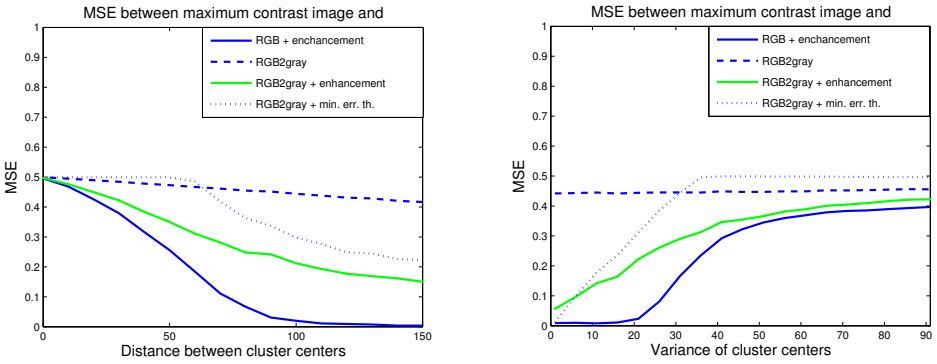

(a) (b)

Figure 3.11: MSE of different contrast enhancement methods: (a) As function of cluster distance $\sqrt{(\mu_0 - \mu_1)^2}$ ($P(0) = P(1) = 0.5$, $\sigma_0 = \sigma_1 = 20/256$); (b) As functions of cluster variance ($\sqrt{(\mu_0 - \mu_1)^2} = 100$, $P(0) = P(1) = 0.5$).

The different methods shown in the figures are as follows: RGB+enhancement means that the proposed colour image conversion method is applied to the RGB colour image, RGB2gray is linear RGB to grey conversion, RGB2gray + enhancement shows the proposed colour image conversion method applied to the grey level image obtained by the linear RGB to grey conversion. RGB2gray + min.err.th. shows the results when minimum-error thresholding [49] is applied to the grey level image obtained by the linear RGB to grey conversion. Based on the results shown in Fig. 3.11, the behaviour of the different methods is as expected. The standard RGB-to-grey conversion provides the weakest contrast. The minimum-error thresholding method provides sufficiently good contrast if the overlap of clusters is not significant. Best contrast representation is obtained by using the proposed contrast enhancement method. It should be noted that utilising the colour information provides the most accurate results, since it uses all the colour information available. Other simpler methods can falsely classify noisy background pixels (e.g. dirt/dust in real Heliotest images) to the foreground and vice versa. The results are shown in Figs. 3.12 and 3.13. The only difference between the images is the location of the cluster centres, the cluster distance $\sqrt{(\mu_0 - \mu_1)^2} = 100$ and noise variance $\sigma_0 = \sigma_1 = 15/256$ are equal.

The actual contrast enhancement method was applied to Heliotest data. To increase

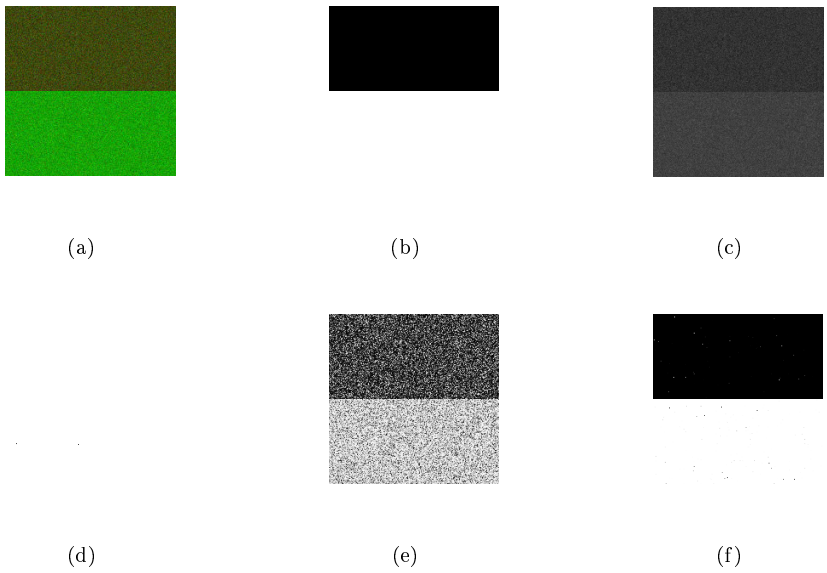

Figure 3.12: Examples of contrast enhancement images: (a) Original RGB image; (b) Maximal contrast image; (c) RGB to grey converted image (MSE=0.4726); (d) Minimum-error thresholding applied to the intensity image (MSE=0.5); (e) Posteriori contrast enhancement applied to the intensity image (MSE=0.2628); (f) Posteriori contrast enhancement applied to the RGB image (MSE=0.0072).

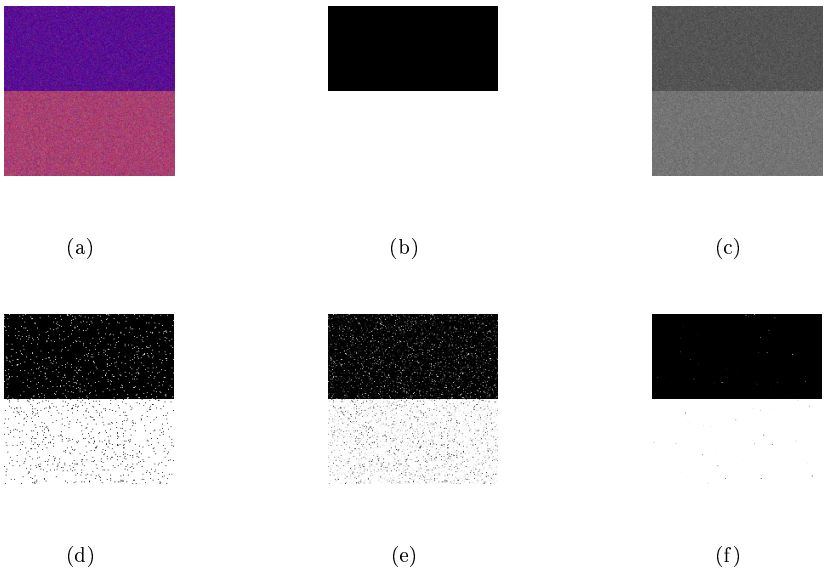

Figure 3.13: Examples of contrast enhancement images: (a) Original RGB image; (b) Maximal contrast image; (c) RGB to grey converted image (MSE=0.4383); (d) Minimum-error thresholding applied to the intensity image (MSE=0.0308); (e) Posteriori contrast enhancement applied to the intensity image (MSE=0.0466); (f) Posteriori contrast enhancement applied to the RGB image (MSE=0.0006).

the successful detection rate, the image contrast can be enhanced to magnify the separability of printed dots from the background. In Fig. 3.14, the performance of contrast enhancement has been demonstrated. The effect on thresholding can be seen in Fig. 3.15, in which an image is converted to grey level linearly by summing the individual colour channels and dividing by 3. The original colour image is also converted to grey level using the proposed method. After both images are in gray level, Method 2 is applied to both images. Both grey level images were normalised to have values between 0 and 1 in order to make the thresholding comparable. Both images in Figs. 3.15(c) and 3.15(f) were thresholded by using same threshold determined by visual evaluation of the thresholding result, the resulting thresholded images can be seen in Figs. 3.15(d) 3.15(g). As can be seen, the missing dot is much more visible in Fig. 3.15(g) with less noise than in Fig. 3.15(d). If the threshold in Fig. 3.15(d) is lowered, the missing dot area in the image becomes larger, but the noisy dots also become more numerous and larger.

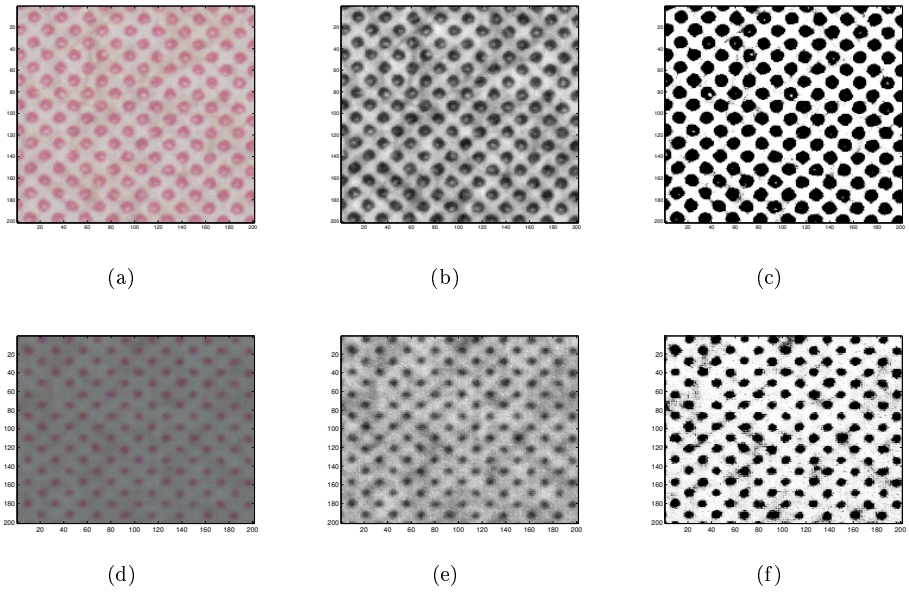

(a) (b) (c)

(d) (e) (f)

Figure 3.14: Partial Heliotest images: (a),(d) Original colour image; (b),(e) Intensity image; (c),(f) Posteriori contrast enhanced image.

3.6.2 Experiments for irregularity detection

Heliotest images

In the experiments, the three methods were compared by studying their accuracy and computational efficiency. All methods were implemented using Matlab. The dataset consisted of 101 Heliotest images scanned from Heliotest samples (for an example, see Fig. 3.16). The regular pattern in each image was a printed raster pattern which consisted

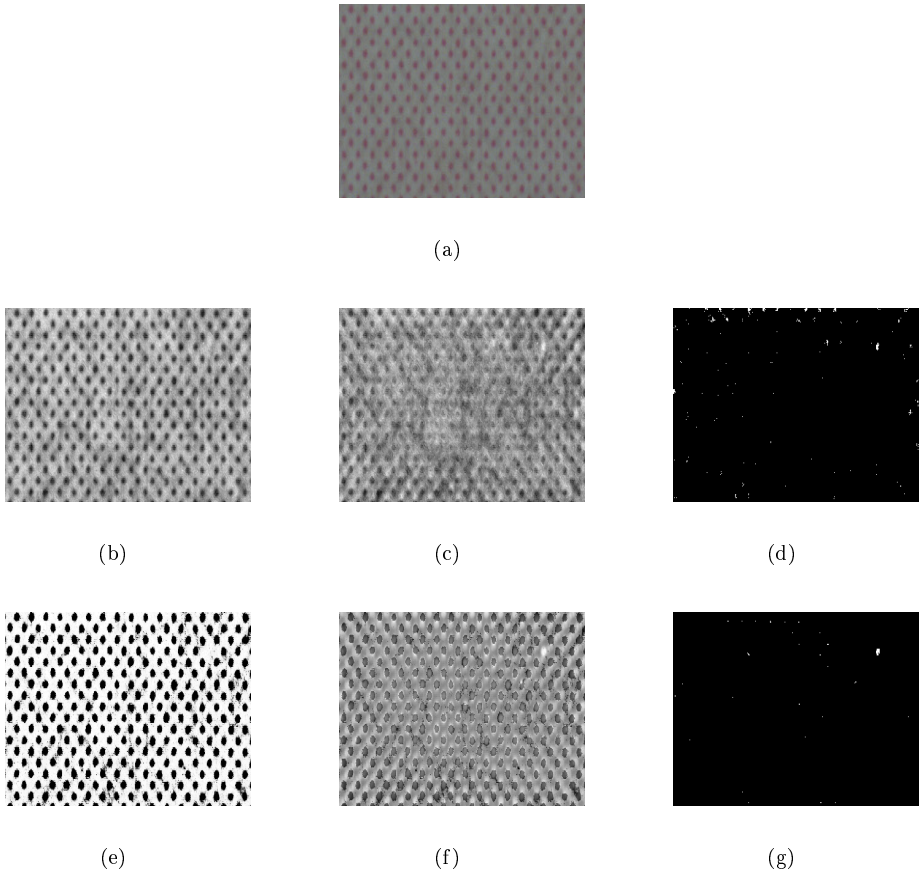

Figure 3.15: (a) Original image; (b) Gray level image; (c) Irregular image of gray level image; (d) Thresholded irregular gray level image; (e) Proposed colour conversion applied to original image; (f) Irregular image; (g) Thresholded irregular image.

of unit atoms with a Gaussian shape and a size of 6-10 pixels in diameter. The accuracy of each method was determined using the measure used in the paper and printing industry: the distance from the beginning of the raster pattern to the 20th missing dot in the raster pattern. This distance gives information about the printability of the tested paper type. Ground truth data was obtained by visually inspecting the images and by marking the irregularities, i.e., missing dot locations. Only the first 20 missing dots were marked, each sample could contain a lot more missing dots, but the paper and printing industry is only interested in the first 20. The results are reported for the proposed methods; global processing of the irregular image (Method 1), self-filtering (Method 2), and local processing of the original image (Method 3).

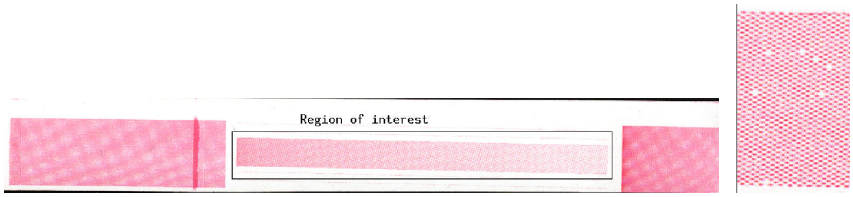

Figure 3.16: Test sample: (a) The measurement area is marked on the image as a rectangle; (b) Small part of the measurement area enlarged.

The number of detected missing dots and false alarms as a function of the radius from the ground truth missing dots are shown in Fig. 3.17 for all methods. The graph indicates how accurately the different methods are able to detect the missing dots. It can be seen that local processing (Method 3) more accurately detected missing dots and gave fewer false alarms. Methods 1 and 2 find all the missing dots, but on average (acceptance radius=4 pixels) they detect 2 more falsely detected missing points than Method 3. Method 3 may fail to detect one actually missing dot but it detects fewer false positives than Methods 1 and 2. The results are demonstrated in pixels and the mean shortest distance between two dots was 7.1 pixels (graphs in Fig. 3.17 stop at 4.0 pixels).

The accuracies of all methods compared to the ground truth distance to the 20th missing dot are shown in Fig. 3.18. Each method was separately used to count the missing dots from the beginning of each strip and each of them returned the distance estimation to the location of the 20th automatically detected missing dot from the start of the print area. In this performance measure, individual false positives and false negatives contributed only to the final error. Using this industrial error measure, all methods performed almost equally well. For 95% of the test samples, the error remains under 8.0 mm. The typical distance to the 20th missing dot varies between different paper grades; with good quality paper the distance is around 80 mm. The average execution times on a laptop PC (Pentium 4, 3200MHz, 512 Mb) for the methods were as follows: Method 1 - 7.76 s, Method 2 - 6.66 s and Method 3 - 49.9 s. The difference in execution times between Method 1 and Method 2 comes from the time needed to process the peaks in the frequency domain. It takes 0.43 s on average to detect and mask the frequency domain peaks with Method 1, whereas with Method 2, utilising frequency domain self-filtering,

the same task requires 0.15 s on average. The methods perform equally well for this industrial measurement. The advantage of Method 3 over the other methods comes from its ability to classify, if such functionality is later needed, the types of missing dots that are detected at the same time when the missing dots are detected.

Examples of the detected missing dots (Method 2) are shown in Fig. 3.19. Figs. 3.19(c) and 3.19(d) show examples where the method seems to be over-sensitive to detecting only partly missing dots as missing dots; however in some cases those points were also considered as missing dots by an expert.

Artificial images

In the second part of the experiments, artificial images were generated to act as controlled inputs to the methods (see Fig. 3.20). The images were prepared based on acquired Heliotest samples, and they consisted of a black background and white Gaussian-shaped peaks with regular intervals between the peaks. To model the uneven background (paper) and imaging process, each image was degraded by adding Gaussian noise with zero mean and normalised variance of 0.001. To model the missing portions of print, each image was further degraded with multiplicative speckle noise. The whole process of image generation can be formulated as follows:

$$\xi(x, y) = \mathrm{H}[\xi_{ideal}(x, y) + \eta(x, y)] \tag{3.25}$$

where $\xi(x, y)$ is the generated image, ξ_{ideal} is the artificial image with the regular pattern, η is the Gaussian noise image, H represents the multiplicative noise function utilising a uniformly distributed random variable with zero mean and varying variance. Mean square errors were computed between the images obtained by Methods 1 and 2 and the original artificial images that contained neither Gaussian nor speckle noise. Irregular images obtained by Methods 1 and 2 were compared to the image which contained only noise. This image was obtained by subtracting the original image with the regular pattern from the generated image. The results of this experiment are shown in Fig. 3.21. To further elaborate the differences of the approaches, Methods 1 and 2 were used to separate two different frequencies from each other. The original image is shown in Fig. 3.22(a), and the resulting regular and irregular images using both methods are shown in Figs. 3.22(b)-3.22(e).

Near regular images

The previous experiments on Heliotest images quantitatively evaluated the accuracy of the methods. To demonstrate generality, the proposed methods were also applied to free form regular textures. Images from the CMU NRT near-regular texture database (`http://graphics.cs.cmu.edu/data/texturedb/gallery/`) were used. Method 2 was applied to several images using the common threshold $\tau = 240$. Examples of irregularity detection from near-irregular textures with artificially imposed irregularities are shown in Fig. 3.23.

It is clear that while the Heliotest assessment appears a straightforward application of the proposed methods and acted as the original reason for the research, the methods also provide a more general approach to irregularity detection from regular and near-regular textures.

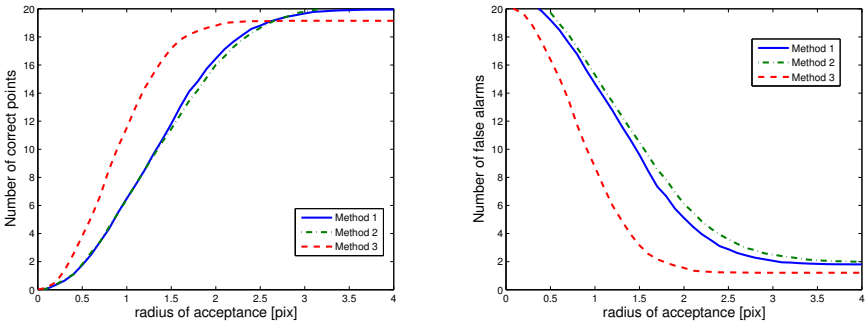

(a) (b)

Figure 3.17: Detection accuracies as functions of radius from the ground truth locations: (a) Correct positives, the faster graph reaches 20, the better the method; (b) False positives. The faster the graph drops from 20 to 0, the better the method.

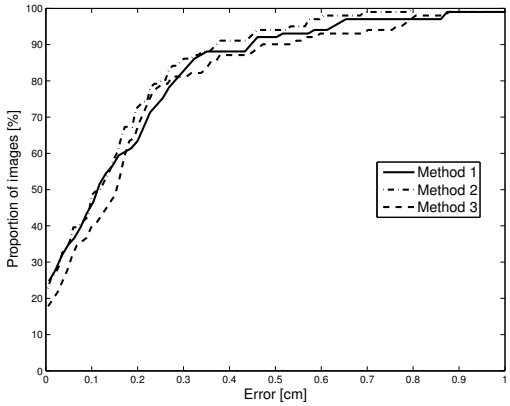

Figure 3.18: Cumulative error distributions with different methods. The faster the graph approaches 100%, the better the method.

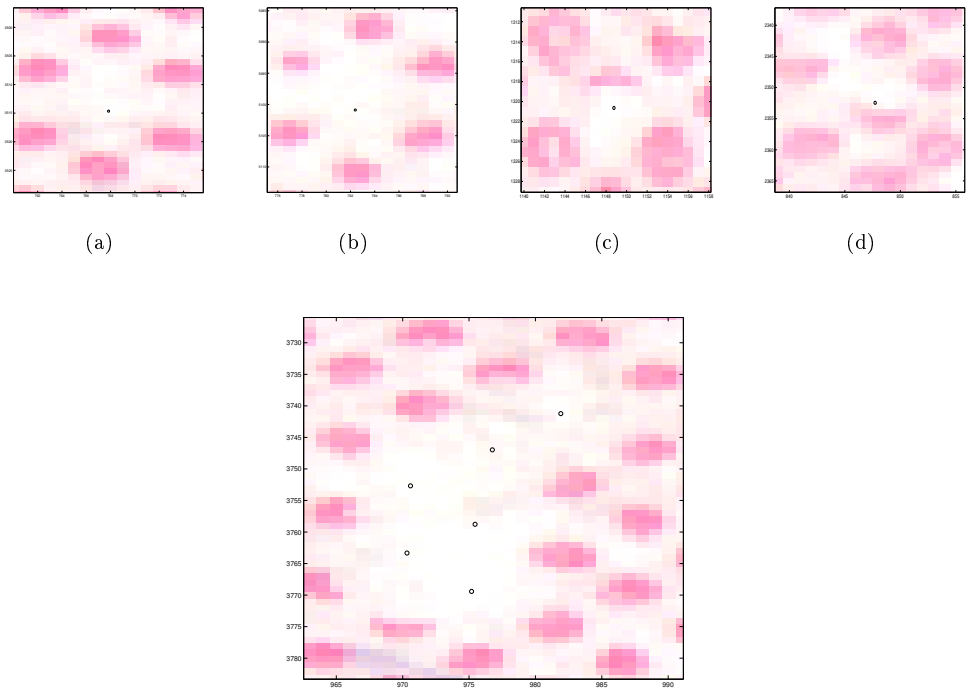

(a) (b) (c) (d)

(e)

Figure 3.19: Examples of detected missing dots: (a),(b) dot completely missing (correct positive); (c),(d) dot partly missing (false positive); (e) a group of missing dots (correct positives).

3.6.3 Discussion

All the presented methods are suitable for detecting irregularities in a regular pattern. Methods 1 and 2 are accurate in detecting missing dots from a pattern, but they cannot match the accuracy of Method 3. This is because Method 3 uses a classifier at each unit cell location to determine whether there is a missing dot or not. The disadvantage of Method 3 is that it requires more computing time. By using controlled input images, it is possible to demonstrate that frequency masks designed for each specific image types (Method 1) provide lower error levels when the results of frequency separation are compared to the ideal regular pattern. Depending on the application, this can be important in the classification of defects if the original image data is not used for this purpose.

Although Methods 1 and 2 are almost identical in nature, Method 1 has advantages over Method 2. Method 1 utilises prior knowledge of the Fourier peaks, and thus, can detect several underlying regular patterns from a given image. For example, if the image has two repeating patterns that have different frequencies, Method 1 can be used to

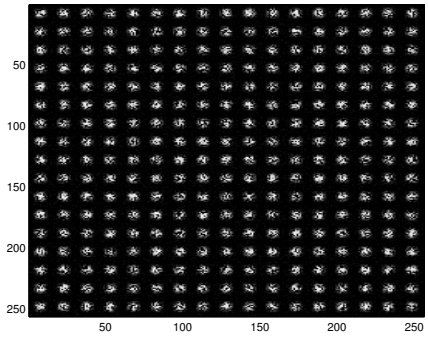

Figure 3.20: An example of an artificial image with highest level of speckle noise.

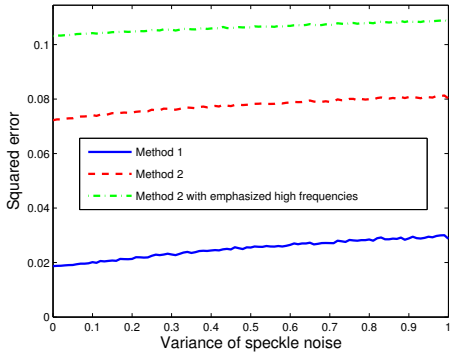

Figure 3.21: Mean square errors of regular images from Methods 1 and 2 for a set of artificial images with different levels of noise. Errors between the irregular images were identical to the presented ones.

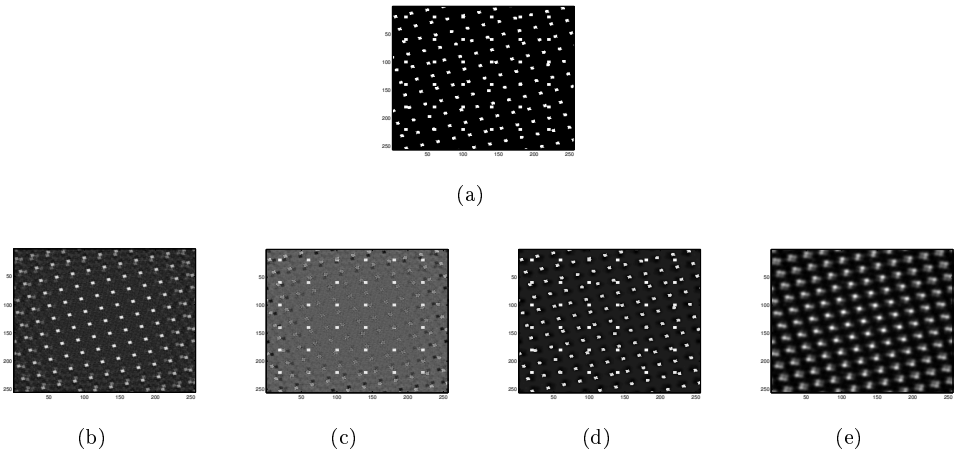

(a) (b) (c) (d) (e)

Figure 3.22: Two independent patterns appearing at different intervals. (a) Original image; (b-c) Separation of the regular (b) and irregular (c) part with Method 1; (d-e) Separation of the parts with Method 2. [(d) regular, (e) irregular].

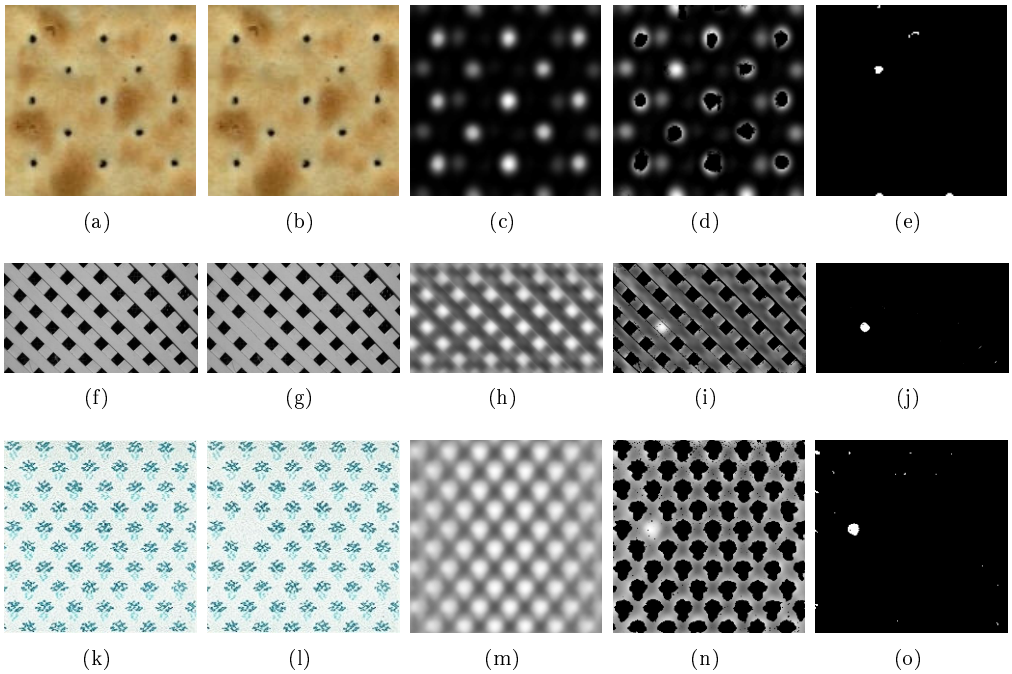

(a) (b) (c) (d) (e)
(f) (g) (h) (i) (j)
(k) (l) (m) (n) (o)

Figure 3.23: Near-regular textures from CMU NRT database; (a),(f),(k) Original image; (b),(g),(l) Artificially generated irregularity; (c),(h),(m) Regular image; (d),(i),(n) Irregular image; (e),(j),(o) Thresholded irregular image.

extract either one of the underlying patterns. Another advantage of Methods 1 and 3 is that they do not suffer from energy leakage as much as Method 2 since Methods 1 and 3 only select the repeating peaks from the Fourier plane and use them to build the regular image. Method 2, utilising frequency domain self-filtering, is unable to extract two different repeating patterns, but instead locates both patterns. This can be seen in Fig. 3.22. The advantage of Method 2, on the other hand, is that it needs no prior knowledge of the spatial properties of the repeating pattern as Methods 1 and 3 do.

From a practical point of view, Method 2 is good for general needs. It is accurate and its computational efficiency is very good. It does not need any training data and can perform the missing dot detection well since there is only a single repeating raster pattern in the Heliotest images. Methods 1 and 3 require parameters for detecting the peaks in the frequency domain, but Method 2 does not.

The key difference between the methods proposed in this thesis and methods found in literature [53, 31, 47] is the use of frequency information for detecting missing dots. The methods found in literature use only spatial information. Therefore the proposed methods have one major advantage over the other methods suggested in literature [53, 31, 47], namely the ability to detect individual missing dots clustered closely together. The other methods fail in this respect. They can detect if there are missing dots in an area, but if there are many missing dots next to each other, then the other methods are prone to fail. On the other hand, if it can be certain that the image to be analysed does not contain clusters of missing image atoms, then the methods proposed by [53, 31, 47] can work well and efficiently. Another benefit of these methods is that they work equally efficiently on image edges. The methods proposed in this paper can fail to detect missing dots near image edges because they are blurrier than image centres as can be seen in Fig.3.8. This happens due to Fourier transform being applied to a discrete image.

The method proposed in [30] is based on the similar Fourier principle proposed in this thesis. The difference between the methods comes from how the Fourier analysis is performed. In [30] they use a special imaging arrangement to perform optical Fourier transformation. The number of missing dots in the imaged area is obtained by measuring the effect of missing dots on the Fourier spectra, namely the effect on intensity between repeating peaks in the Fourier plane. Methods proposed in this thesis work very similarly with the difference being that first the perfectly regular image is obtained based on the repeating intensity peaks in Fourier plane. Then by subtracting this regular image from the original image with the missing dots, not only the missing dots can be calculated, but also their locations. The irregular image, obtained by subtracting the regular image from the original missing dot image, does, however, contain some noise. Due to the discreet nature of image processing and simple windowing used, the irregular image "leaks" some energy from the intensity peaks in the Fourier plane into neighbouring frequencies, causing some noise into the irregularity information. Method 2 suffers from this more than Methods 1 and 3. Methods 1 and 3 band pass only the repeating peaks in the Fourier domain and therefore the energy leakage does not affect the regular image as much.

The key advantage of method [30] is unquestionably its speed. The optical Fourier transformation is fast to perform and the results obtained by the system seem quite reliable. The systems seems very suitable for on-line missing dots measurements from

printed paper. However when number and locations of missing dots are needed, it is recommended to use methods proposed in this thesis.

3.7 Summary

In this chapter, three methods for measuring irregularities from a regular pattern was introduced. As an example, the methods were applied to Heliotest samples which consisted of a regularly printed raster pattern that could have missing dots, i.e. irregularities. The accuracies and execution times of the methods were compared, and their strengths and weaknesses discussed. For fast execution and good accuracy, the method based on frequency domain self-filtering (Method 2) was a good choice. However, if the application is sensitive to changes to the regular or irregular patterns or the image to be assessed contains more than one repeating pattern, Methods 1 and 3 utilising prior knowledge of the repeating patterns are more applicable.

An efficient method for enhancing contrast between two dominating colours in an image was also introduced. The contrast enhancement enabled later image processing steps to work more reliably.

Chapter IV

Runnability evaluation by detecting surface defects

Paper runnability was introduced in Section 2.2. In short, anything that adversely affects runnability is undesirable. Small particles that stick to printing heads or obstruct printing rollers is one part of this problem. Paper surface strength is typically inspected with the IGT picking test in order to determine how fast the paper can be printed without surface defects or tearing.

4.1 The IGT picking runnability test

Picking is closely related to linting, introduced in Section 2.2. The greatest difference between picking and linting is that picking is at least partially attached to paper whereas linting consists of totally loose particles [83]. The origin for picking can be poor paper surface strength or fast setting of the printing or both. The IGT picking test is printed by an IGT picking device that prints a test pattern on a paper sample with increasing speed using tacky printing oils with known viscosity (standards [39, 84, 78]). The IGT picking apparatus is a mechanical device which does not produce any image data from samples. The apparatus consists of an oil applicator and a printing unit in which a printing cylinder produces a test pattern $200 - 320$ mm long and 10 mm or 20 mm wide. The printing speed increases linearly towards the end of the print. The proportion of visible defects, e.g., fibre surfacing or coat tearing, is assumed to provide information about the printing properties of a particular paper type (printability and runnability). The longer the distance between the print starting point and the beginning of fibre surfacing, the higher the speed that can be used in the printing process. The speed and the printing oil viscosity information can be used to calculate the velocity-viscosity product (VVP), which enables comparisons between paper grades obtained using different printing oils. The VVP is calculated as follows:

$$VVP = v_d * V \tag{4.1}$$

where v_d is the speed at which the picking started and V is the printing oil viscosity in Pascals (Pa) at the printing room temperature [37]. Fig. 4.1 shows the different machines

required for picking inspection.

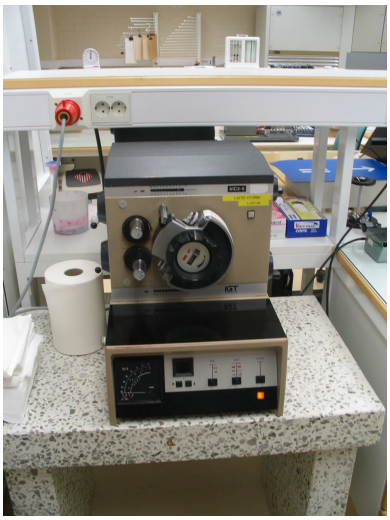

(a)

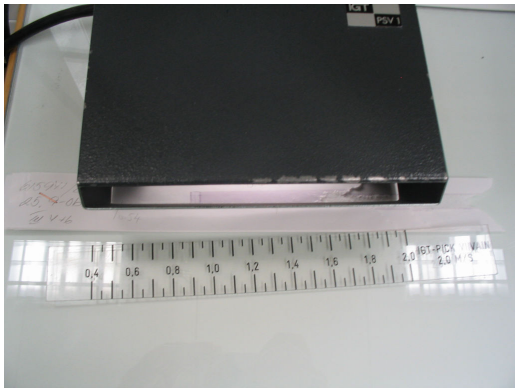

(b)

Figure 4.1: Equipment for inspecting picking: (a) Machine for making the test prints; (b) Special lighting system for visually determining the picking start location.

A problem in picking test inspection is the determination of the picking start location. Different experts have different opinions about where the picking should be marked as starting. Picking can be marked as starting if the defect size is small surfacing fibre or if 2/3 of the test print area width has torn, or somewhere in between. This criterion varies between experts. The most prominent problem is naturally eye strain. Due to these problems, standardisation and automation of the picking print analysis is desirable. Fig. 4.2 illustrates this problem well. In Fig. 4.2(a) an expert has few options for

interpreting where the picking starts, whereas in Fig. 4.2(b) the same type of paper is printed with different speed settings (speed at the end of print) and the marked picking start location (dark dots near image edges) lacks consistency.

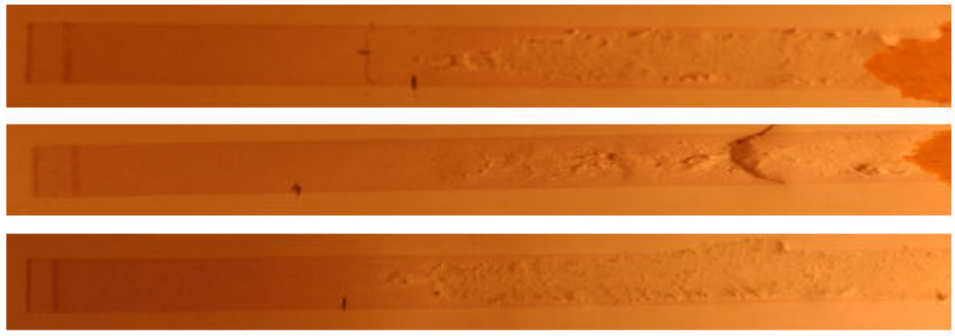

(a)

(b)

Figure 4.2: Example of difficulties in determining the picking start location. Picking start locations are marked with dark dots on the images: (a) "Easy" case; (b) Inconsistency in the results. Printing speed on the images increases from left to right.

4.2 Overall structure of the automated IGT picking test

Picking detection starts with image acquisition. Section 4.3 describes the necessary imaging arrangements required for picking detection. In order to highlight the protruding fibres on the samples, the samples are illuminated from a large angle with respect to surface normal.

Section 4.4 introduces the problem of detecting small and sparse details. In the following subsection 4.4.1 an analytical model for small and sparse details is introduced and how the defects are visualised. The visual model is used merely for visual comparison of an artificial image and an actual picking test image.

Section 4.4.2 reviews the well known thresholding methods that were used for detecting the small and sparse details. First the methods are introduced and in the following section 4.4.5 their performance for thresholding small and sparse details is determined experimentally; First with artificially generated data and then with actual picking samples (section 4.5).

4.3 Image acquisition

The first step is to obtain the sample image. The resolution of the image has to be high in order to detect small surface defects. A resolution of about 1200 dpi is sufficient to detect small defects, and the resulting image size is about 1200×3000 pixels. The sample surface should not be touched before the sample is imaged so that any small fibres that have lift from the paper do not get flattened. In the Heliotest a circular light source directly above the sample is used but this layout is not suitable for picking test inspection. In the case of picking test inspection, oblique lighting (front light at very low angles) is more suitable for detecting surface defects such as bumps, lift fibres and particles. With the oblique lighting, the surface of the object stays rather dark, but lift defects appear bright. The reason for this is that light from the flat surface does not reflect at the camera but lift defects reflect the light to the camera (Fig. 4.3). The drawback of this lighting arrangement is that surface bumps also reflect the light at the camera.

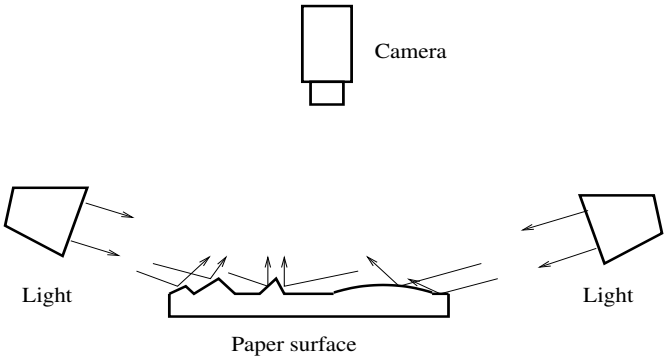

Figure 4.3: Oblique lighting principle.

After an image has been acquired under oblique lighting, the printed area is detected. Fig. 4.4 displays the different areas of a picking sample. Printed area detection is achieved using the same method as in the Heliotest in Section 5.2. Edge detection parameters for picking images have to be selected more carefully since the contrast between the paper and the printing oil/ink is worse than the contrast between the Heliotest pattern and paper.

Figure 4.4: Different areas of a picking sample. Printed area is marked with a thick borderline. The start of the printed area contains some picking due to initial impact of the printing head on the paper.

4.4 Picking detection by thresholding

Thresholding based segmentation can be found at the core of many machine vision based inspection applications, such as [16, 57, 61]. Several analytically sound and general solutions exist, but in practice, thresholding is often based on application-specific heuristics. The use of heuristics usually prevents reusability, and the methods become sensitive to small changes in the problem setting. This study provides a more general solution to detect adaptively a small number of fine details from a background. This solution is developed by first defining analytically the appearance of the details and then by studying the performance of the most well-known adaptive thresholding methods, that is, methods which do not require any parameters.

Binary thresholding is one of the most commonly used and essential operations in digital image processing, and in many applications, thresholding is used at some point of the algorithm. Even though the operation itself is very simple, the problem of selecting an optimal threshold value is not trivial at all. For a single image, the optimal value can be selected manually, but adaptive thresholding methods exist intended to automatically estimate the optimal value. Due to its importance, adaptive thresholding has been studied for a few decades, and a wide variety of different methods have been proposed [79]. The extensive work in the past should have resulted in a proper method for any existing problem. Since different methods may value different properties, method selection depends on the characteristics of the problem domain. However, new problem characteristics are continuously encountered in practical problems, and thus, adaptive thresholding still remains intensively studied after more than 30 years.

Most methods perform well when the image foreground and background constitute areas of sufficiently equal sizes, and the grey level values have substantially non-overlapping distributions [79]. However, when either or both of the above assumptions are not valid, major difficulties can be encountered. This is the case here, where the motivation originates from a problem in which small paper surface defects must be automatically detected [19]. The samples can be imaged into a digital form where low intensity grey-level values correspond to the paper surface, and high intensity grey-level values correspond to small defects on the surface. The proportion of pixels related to defects is typically very small, making the grey-level histograms almost unimodal. Additionally, the grey-level values of both the defects and surface overlap significantly. The spatial distribution of the defects can be considered random, although a single defect in an image can consist of a few neighbouring pixels in the image. This spatial information can be taken into account

by using a spot detector, which will be introduced in Section 4.5.2. The filter emphasises small intensity changes in a small area in the image and therefore encompasses the spatial information of a single defect. Due to the spatial randomness of the defects, the application of global thresholding methods is motivated.

This thesis assesses the ability of adaptive thresholding to bring up fine and sparse details. The problem is solved by defining the necessary statistical properties in the histogram domain and by analysing the performance of well-known and well-performing general adaptive thresholding methods and methods specifically applicable to unimodal histograms.

4.4.1 Fine and sparse details on noisy backgrounds

The motivation for researching methods to detect fine and sparse details and their possible application areas are explained first. In the particular case discussed here, the problem was to automatically perform the visual assessment of IGT picking samples. To get the image data, the paper strips are digitally imaged under oblique lighting (Fig. 4.5(a)). The grey-level histogram of the strip can be seen in Fig. 4.5(b).

In Fig. 4.5(a), the defects are not clearly visible, and the imaging suffers from the distortions characteristic of board strips (e.g., cockling). However, after proper image enhancement, the defects appear as tiny spots having higher intensity than the surrounding noisy background (Fig. 4.6). This masking however averages the image and therefore comparing values of neighbouring pixels after masking is useless. Consequently, a global processing is used to threshold these defects.

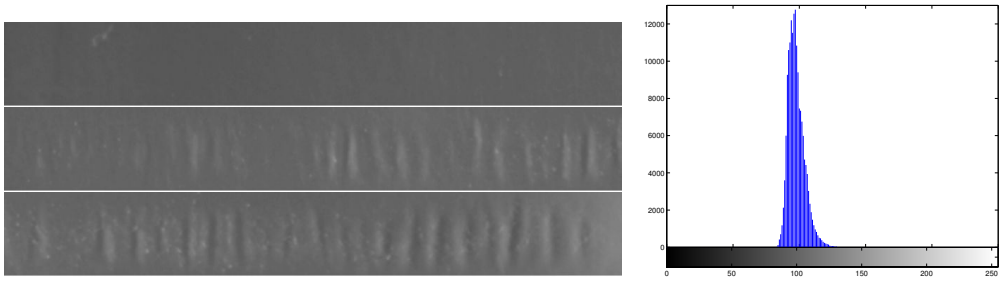

(a) (b)

Figure 4.5: Image of a picking sample (coated board) captured under oblique lighting: (a) The whole strip is divided into 3 pieces for better presentation. The adjacent pieces from left to right (printing speed increases) are arranged from top to down; (b) Grey-level histogram of the image.

The separation of image areas into background (paper surface) and foreground (defects) is more understandable from Fig. 4.6. For further processing, however, a suitable threshold value at which defects on the paper surface begin to appear in the foreground must be selected. Based on the set of test samples, it was found that the proportion of pixels representing the defects was 0.1-5.0% of total image area, and the defect pixels

partly shared intensity values with the background pixels. Therefore, the background and foreground are mixed into a nearly unimodal grey-level histogram, making selection of the threshold value a very difficult problem.

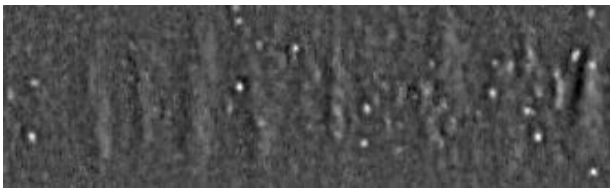

Figure 4.6: Enhanced partial image of picking sample.

The nature of the defects and their presence in the given problem have motivated to introduce the notion of *fine and sparse defects*. It should be noted that the terms *details* and *defects* are used interchangeably in this case. The fine and sparse defects are small (fine) and isolated (sparse) signal patches comprising only a minority of the total image area. Their intensities are close to or mixed with the background intensity range. To study the problem more extensively, a statistical model of the defects must be derived first. Based on the statistical model, the behaviour of different thresholding techniques can be analysed more analytically since the effect of all model parameters can be studied.

If the spatial relationships are neglected, image pixels can be considered as realizations of a random variable. For a sufficiently large image, the grey-level histogram corresponds to the probability density function of the random variable, and thus, it is sufficient to model the probability density function (pdf) to model the details.

A noisy background can be modelled with a single probability density function, and the foreground can be treated as a mixture of probability density functions. Finally, the whole pdf consists of a weighted sum of pdfs for both the foreground and background.

The intensities of background pixels can be modelled by values of a random variable having the normal distribution $N(\mu_b, \sigma_b)$ with the mean value μ_b, and standard deviation σ_b.

A single defect can be modelled by a low probability (low a priori) random variable which adheres to the normal distribution

$$P_d(i)\frac{1}{\sqrt{2\pi}\sigma_d(i)}e^{\frac{-(x-\mu_d(i))^2}{2\sigma_d(i)^2}} \tag{4.2}$$

where $\mu_d(i)$ and $\sigma_d(i)$ denote the intensity mean value and standard deviation for the i-th defect, and $P_d(i)$ corresponds to the a priori probability of encountering the defect. However, since a single defect is highly localised (concentrated near to a single spatial location), $P_d(i)$ corresponds to a proportional spatial size of the defect rather than a true a priori probability. Correspondingly, the proportional spatial size of the background is

$$P_b = 1 - \sum_i P_d(i) \ . \tag{4.3}$$

Now, the resulting histogram of fine and sparse defects on a noisy background depends solely on the set of parameters $\{\mu_b,\ \sigma_b,\ \mu_d(i),\ \sigma_d(i),\ P_d(i)\}$. Finally, the composite probability density function which defines the expected shape of the histogram is

$$f(x) = P_b \frac{1}{\sqrt{2\pi}\sigma_b} e^{\frac{-(x-\mu_b)^2}{2\sigma_b^2}} + \sum_i P_d(i) \frac{1}{\sqrt{2\pi}\sigma_d(i)} e^{\frac{-(x-\mu_d(i))^2}{2\sigma_d(i)^2}} . \qquad (4.4)$$

One more consideration is the distributions of $\mu_d(i)$ and $\sigma_d(i)$. The simplest class of sparse defects has the uniform distribution $\mu_d(i) \sim U(a,b)$ or the normal distribution $\mu_d(i) \sim N(\mu_{\mu_d}, \sigma_{\mu_d})$, and the standard deviation $\sigma_d(i) \sim N(\mu_{\sigma_d}, \sigma_{\sigma_d})$ (see Figs. 4.8 and 4.11). It should be noted that the number of defects can also be obtained from a random distribution, but it does not actually affect the results but only the foreground/background ratio.

Model visualisation

For the visualisation and for comparison of the artificial images with the real ones, a model in the spatial domain that corresponds to the model in the domain of grey-level histograms must be defined. This is done because obtaining the foreground and background distributions from actual picking samples has proved to be very difficult. The first problem was in determining which pixels in a picking image actually are defects. The second problem was to actually mark the pixels determined to be defective. When an image is observed without magnification, the picking locations are somewhat clear, but when the image is magnified, the difference between the background and defect was almost impossible to distinguish and in most cases failed.

This model includes the histogram and a mapping from the histogram to the spatial plane. The spatial model must be consistent with the histogram model and have the same parameters; the resulting artificial image possesses the same histogram as obtained via the histogram model.

First, the image background is generated using a random variable with the same distribution and parameters μ_b and σ_b as described for the histogram model. Next, the defects are randomly seeded on the noisy background. For each defect, the area is derived in accordance with the total image size, and the proportional defect size $P_d(i)$.

Finally, values at each defect area are derived from the corresponding random variable, $N(\mu_d(i), \sigma_d(i))$. To vary also area sizes, the proportional areas can be derived from $P_d(i) = N(\mu_{P_d}, \sigma_{P_d})$. It should be noted, however, that if a certain foreground/background ratio is required, the proportional sizes $P_d(i)$ must be normalised to achieve the requested ratio. An example of an artificial image is shown in Fig. 4.7.

The definition of details was carried out in the histogram domain, and thus, methods for histogram-based global thresholding can be used to separate the background and foreground. In the next section, the methods are discussed, and their detection performance is studied utilising the defined statistical model.

4.4.2 Defect segmentation by thresholding

Thresholding methods are based on the assumption that the grey levels of pixels belonging to objects (foreground) are substantially different from the grey levels of pixels belonging to the background. However, the characteristics of the histogram and the spatial distribution of the objects make some thresholding methods more suitable to a specific task than others.

Based on the definition of the details, suitable thresholding methods were searched from literature. First, the most popular and well-performing general-purpose thresholding methods were considered, several methods designed specially for unimodal histograms were studied.

4.4.3 Multimodal grey level thresholding methods

General thresholding methods should perform well when (i) the foreground objects and background constitute proportionally the same sizes in an image, and (ii) the grey-level values of objects and the background possess substantially distant and non-overlapping distributions. When these restrictions can be met, one of the most popular methods is Otsu's method [68]. Methods by Kittler et al. [49] and Kapur et al. [46] have been shown to outperform many others in comparisons [79]. Therefore, these methods are good candidates as general thresholding methods for the given problem. In the following sections, the three methods will be briefly reviewed.

Otsu's method

Otsu's thresholding method is based on the idea of finding a threshold value that minimises the within-class variance of the resulting foreground and background classes [68]. Thus, the optimal threshold T is calculated by minimising the criterion function

$$J(T) = \frac{P_1(T)\sigma_1^2(T) + P_2(T)\sigma_2^2(T)}{\sigma^2} \tag{4.5}$$

where σ^2 is the grey-level total variance estimated from the histogram and $P_1(T)$ and $P_2(T)$ are prior probabilities associated to foreground and background.

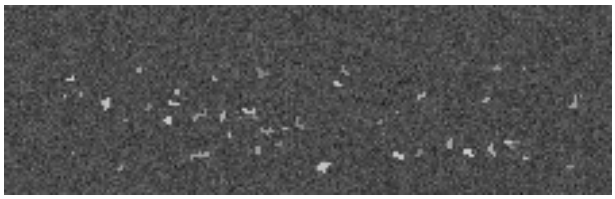

Figure 4.7: An artificial image with fine and sparse details generated using the visualisation of the histogram model ($\mu_b = 0.3$, $\sigma_b = 0.055$, $i = 1, \ldots, 50$, $\mu_{\sigma_d} = 0.01$, $\sigma_{\sigma_d} = 0.002$, foreground/background ratio $= 0.015$, $\mu_{P_d} = 5$, $\sigma_{P_d} = 3$). Intensity values scaled for visualisation.

Otsu's thresholding is one of the most widely used and cited threshold estimation methods. The method is very robust, and it provides thresholding results of considerable quality in a vast variety of cases. Performance is good when the number of pixels in the foreground and background are close to each other. However, the method usually fails to find an appropriate threshold value if the number of foreground pixels is less than 5% of the total image size. With unimodal or nearly unimodal histograms the method tends to split the only mode in the middle, resulting in a "salt and pepper" binary image [49].

Kapur's method

A thresholding method based on entropy has been proposed by Kapur et al.[46]. The method maximises class entropies, which can be interpreted as measures of class compactness and separability. In this case, the criterion function can be given as

$$J(T) = -\sum_{g=0}^{T} \frac{h(g)}{P_1(T)} \log\left(\frac{h(g)}{P_1(T)}\right) - \sum_{g=T+1}^{n} \frac{h(g)}{P_2(T)} \log\left(\frac{h(g)}{P_2(T)}\right) \tag{4.6}$$

where n is the maximum length of a histogram $h(g)$ of grey level values g. $J(T)$ is maximised to obtain maximum information between the object and background distributions in the image. The discrete value T, which maximises $J(T)$, is the threshold value. The method is suitable for images that have good separation between class entropies. Such images are, for example, material defect images. Such an image could be taken from, for instance, a fractured aircraft fuselage. In such a case the defect entropy differentiates well from the rest of the image even when the difference in the spatial image is hard to distinguish.

Kittler's method

Kittler and Illingworth have proposed a thresholding algorithm whose cost function is optimised based on the Bayesian classification rule [49]. In this method, it is assumed that components in the bi-modal histogram $h(g)$ in the grey level image are normally distributed. Normal distributions are defined by their means μ_i, standard deviations σ_i, and a priori probabilities P_i. For a case of two different classes ($i = 1, 2$), the background and foreground, and given a threshold T parameters can be estimated from the following:

$$\begin{aligned} P_i(T) &= \sum_{g=a}^{b} h(g) \\ \mu_i(T) &= \frac{1}{P_i(T)} \sum_{g=a}^{b} h(g)g \\ \sigma_i^2(T) &= \frac{1}{P_i(T)} \sum_{g=a}^{b} (g - \mu_i(T))^2 h(g) \end{aligned} \tag{4.7}$$

where

$$a = \begin{cases} 0 & \text{i=1} \\ T+1 & \text{i=2} \end{cases} \text{ and } b = \begin{cases} T & \text{i=1} \\ n & \text{i=2} \end{cases} . \tag{4.8}$$

Now, the criterion function can be calculated as

$$\begin{aligned} J(T) =& 1 + 2[P_1(T)\log\sigma_1(T) + P_2(T)\log\sigma_2(T)] \\ & - 2[P_1(T)\log P_1(T) + P_2(T)\log P_2(T)] \ , \end{aligned} \tag{4.9}$$

and the minimum error threshold can be computed by minimising the criterion $J(T)$. The method is suitable for thresholding images that have clearly bi-modal distributions for the background and foreground. The method can also perform well with histograms where the number of pixels contributing to the background and foreground distributions differ significantly or when the distribution between the foreground and background is nearly unimodal. In such a case the threshold is placed on either side of the mode resulting in an image where most of the pixels are classified to one class, and the rest to another.

4.4.4 Unimodal histogram thresholding methods

As already discussed, most thresholding methods work in the general case of bi- or multi-modal grey-level histograms. In such cases, all modes in the histogram are considered to represent different objects, or the background. However, the properties of the fine details, as seen above, can cause the images to have a distribution which is close to unimodal, therefore, the information available for distinguishing the details is hidden somewhere that looks like normal background noise. Fortunately, this is not a new problem in the field of thresholding and several different methods have been proposed. Some of these methods have a more sound basis while others are more or less ad hoc solutions. Two unimodal thresholding methods from the literature, Tsai's method [87] and Rosin's method [74], are interesting because of their adaptive nature. These two should be applicable for the given problem. They are reviewed briefly below.

Tsai's method

Tsai has introduced two similar approaches to image thresholding using smoothed histograms, one of which is especially intended for unimodal histograms [87]. Both approaches are introduced here, but the approach intended for unimodal histograms is of more interest for the given problem area. The method differs from previous methods such that it evaluates the shape of the histogram whereas the methods reviewed earlier use various statistical properties of image histograms.

The first approach looks for peaks and valleys in the histogram smoothed with a Gaussian kernel. The smoothing level is adjusted to make the smoothed histogram contain exactly the same number of peaks as the desired number of thresholding levels. The valleys between the peaks are selected as the threshold values. In the case where the number of peaks is less than the desired number after using the smallest possible Gaussian kernel for smoothing, additional threshold values are selected as the maximums of curvature of the histogram.

The second approach utilising curvature is intended especially for unimodal histograms, and represents a custom case of the first approach. In the case where only one peak can be found in the histogram, which is the unimodal case, the threshold value is selected as the

intensity value at which the histogram reaches its maximum curvature. The curvature values are calculated from [87]

$$K_t = \frac{1}{R}\sum_{j=1}^{R} |\psi_{t+j} - \psi_{t-j}| \tag{4.10}$$

where

$$\psi_t = \frac{1}{R}\sum_{j=1}^{R} \frac{h_k(t+j) - h_k(t-j)}{2j},\ h_k(i), i = 1 \ldots R \tag{4.11}$$

are the smoothed histogram values. $h_k(t)$ is the number of pixels with grey level t at the kth iteration. R specifies the region of support, and it is used as a smoothing factor to compute the mean tangent angle ψ_t and the mean curvature K_t at grey level t. To avoid over smoothing, a small R ($R < 3$) is generally used.

The basic idea behind the second approach is that it is assumed that even though the image histogram is unimodal, there might be some discontinuity at a point where the background and foreground distributions overlap. By detecting this discontinuity, the background and foreground of an image can be thresholded. If there are no discontinuities in an image histogram, then the performance of the method is questionable.

Rosin's method

Rosin's thresholding is another method for binary thresholding in the case of unimodal histograms [74]. This simple algorithm is shown in algorithm 3.

Algorithm 3 *Rosin thresholding*

1: *A line is drawn from the maximum of the histogram to the last non-zero element of the histogram:*
$(\underset{i}{\text{argmax}}\ h_i,\ \underset{i}{\max}\ h_i) \rightarrow (\underset{i}{\text{argmax}}\ [h_i = 0 \text{ and } h_{i-1} \neq 0], 0)$*, where* h_i *is the* i*-th element of the histogram.*

2: *The optimal threshold value is selected as the intensity value which maximises the perpendicular distance between the line and the histogram.*

This method definitely lacks intuitive motivation. Theoretical mathematical analysis shows that the method is almost insensitive to foreground pixels, and it actually determines the threshold value using only information about the dominating background [74]. The method is not always applicable, but works as long as the histogram mode is not so broad as to fill most of the histogram, and the mode is not too strongly peaked.

4.4.5 Evaluation of thresholding methods

The constructed model allows detailed analysis of different methods as functions of the model parameters since the distributions of both foreground and background are known. The optimal selection of a method for a specific application can be achieved by resolving which model parameters correspond to the variation in the acquired data.

The most important success factors in the evaluation of different adaptive thresholding methods are the number of not detected foreground pixels (false negatives) and falsely detected background pixels (false positives). The values however are dependent, and thus, should be combined to unambiguously compare the success between different methods. For the comparison, the enhanced Venkatesh-Kitchen discrepancy measure introduced in [22] was adopted. The discrepancy measure was originally devised for comparison of edge detection methods, but can be utilised here by setting the measure parameter values to $\alpha = 0.5$, $\beta = 0.5$, $\gamma = 0.0$ and $\delta = 0.0$, resulting in the following discrepancy error measure:

$$\text{error} = \text{false positives} \times \alpha + \text{false negatives} \times \beta \tag{4.12}$$

$\alpha = \beta = 0.5$ yields from the assumption that both false positives and false negatives are considered as equally erroneous mistakes. γ and δ are set to zero since they affect the spatially dependent error factors, that is, errors near correct values are considered less erroneous compared to errors further away. This is motivated in the case of edge detection, but for fine and sparse details the errors are equally erroneous regardless of their location.

In the picking data, for example, the statistical properties consistently change along the strips. In this specific case, the change can be modelled as an increase in the a priori probability of encountering a defect $P_d(i)$ as demonstrated in Fig. 4.8. In Fig. 4.8 the histogram, computed from areas of the same size in different locations of the sample, shapes remain the same but their amplitude increases.

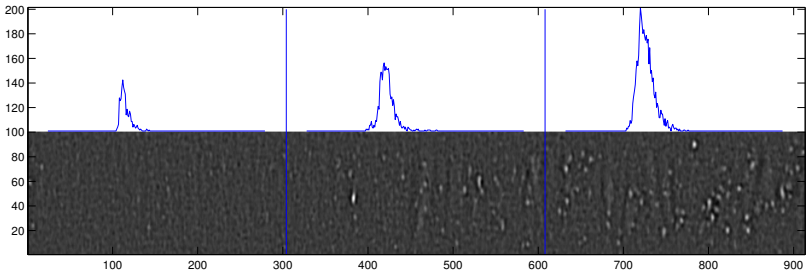

Figure 4.8: Histograms of manually marked defects.

Since the foreground/background ratio is clearly an important property, it is motivated to inspect performance of different methods as a function of this ratio. This is done by applying the methods to artificial images. The behaviour remains the same for different selections of parameters, but here the values are derived to correspond to the ones occurring in the picking samples. The actual foreground/background ratios vary between $0.1\%-5.0\%$ while the other characteristics correspond to the model parameters $\mu_b = 0.30$, $\sigma_b = 0.055$, $i = 1, \ldots, 50$, $\mu_d(i) \sim U(0.50, 0.80)$, $\sigma_d(i) = N(\mu_{\sigma_d}, \sigma_{\sigma_d}) = N(0.01, 0.002)$. The behaviour was inspected for ratios between 0.001 and 0.050, and the histograms and images corresponding to the two extreme values are shown in Fig. 4.9. It is advisable to note that the methods are applied to model histograms and the probability of a miss classification is not an actual miss classification for real picking images. False negative

values in Fig. 4.10(a) are obtained by calculating how much of the estimated foreground is below the threshold obtained by the different thresholding methods. Similarly, false positives in Fig. 4.10(b) are obtained by calculating how much of the background distribution is above the threshold obtained by the different thresholding methods. The discrepancy measure in Fig. 4.10(c) is calculated by using Eq. 4.12.

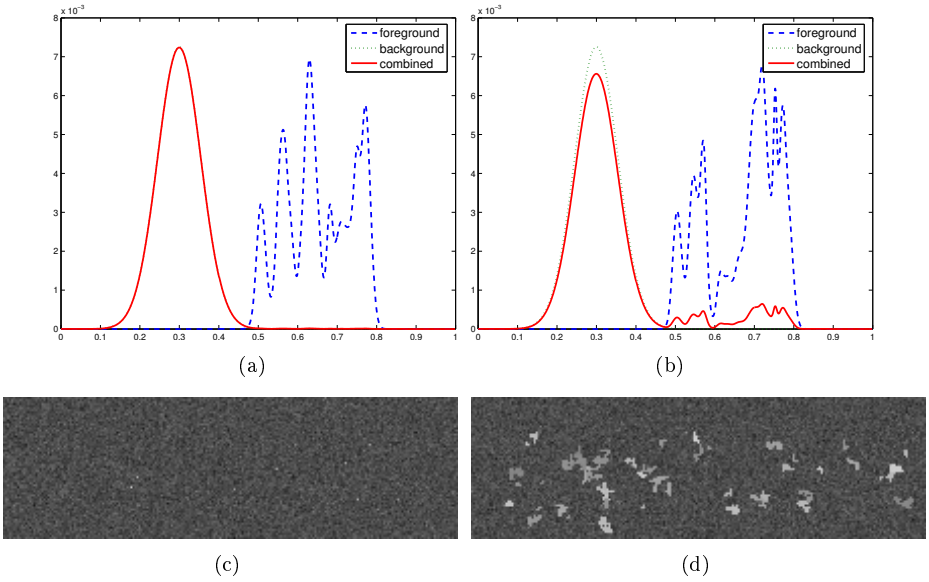

Figure 4.9: Model-generated histograms and the corresponding artificial images: (a),(c) Foreground/background ratio ($\sum P_d(i)/P_b$) 0.001; (b),(d) 0.05.

Surprisingly, a change in the a priori value does not induce any significant change in the performance of the methods as shown in Fig. 4.10. This behaviour is natural for methods based on the bi-modality assumption (Kittler and Rosin). Otsu's method completely fails by detecting most of the background as foreground (Fig. 4.10(b)), and Kapur's method fails by missing a significant number of foreground defects (Fig. 4.10(a)). These two general thresholding methods seem to be inapplicable to the given problem domain. Tsai's method performs well for small numbers of defects, but it becomes unstable when the foreground/background ratio approaches 0.05 (Figures 4.10(a) and 4.10(b)). The success of the different methods become even more clear in the discrepancy graph in Fig. 4.10(c). The two most successful methods are Kittler's and Rosin's methods. The change in thresholds can be seen from Fig. 4.10(d). Picking data also supports the next study since the distribution of paper defects can be modelled as a normal distribution (Figs. 4.8 and 4.11).

Since the histogram in Fig. 4.11 posses a clearly unimodal distribution, it is motivated to study how the methods perform as a function of the level of unimodality. The tolerance can be tested by varying the mean of the defect distribution. The mean of the foreground distribution μ_{μ_d} was varied between 0.36 and 0.56 while the other parameters were kept

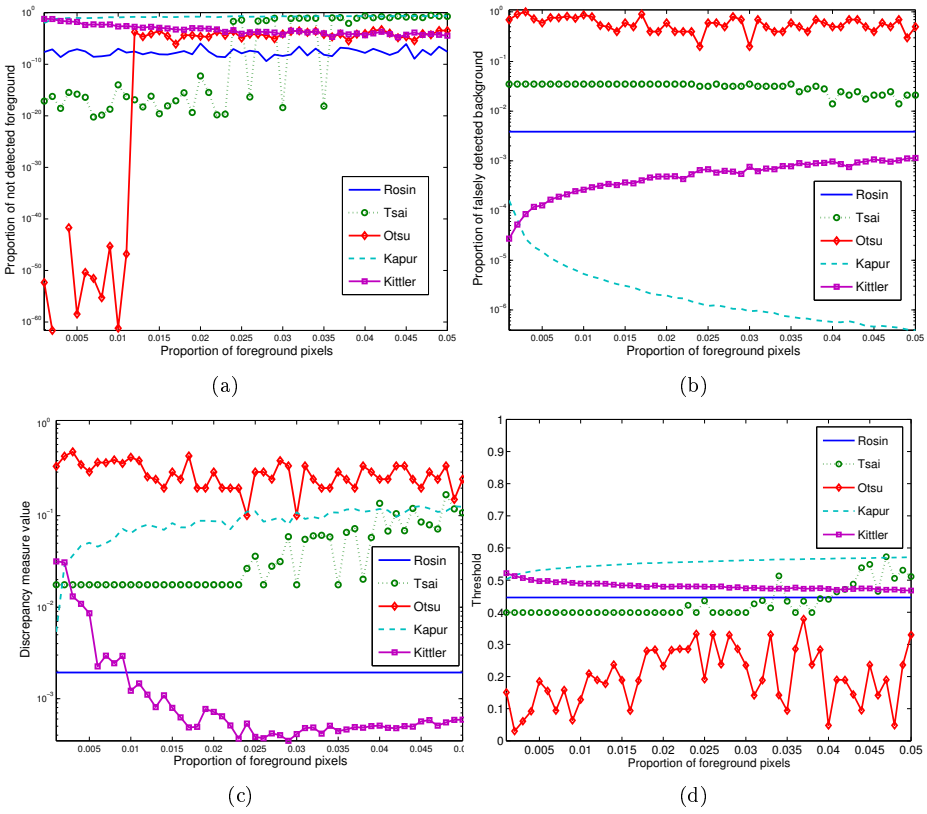

Figure 4.10: Detection results for artificial data, lower values are better in Figs. (a)-(c): (a) Proportion of not detected foreground pixels; (b) Proportion of falsely detected background pixels;(c) Discrepancy; (d) Threshold change with respect to foreground/background ratio.

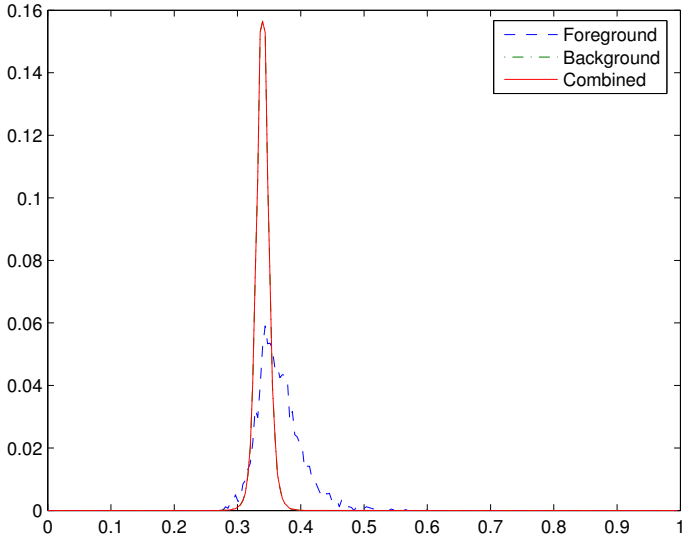

Figure 4.11: Histograms of manually marked picking defects and the background. The foreground/background ratio is $\sum_i P_d(i) = 0.005$, the background mean is $\mu_b = 0.345$ and the standard deviation $\sigma_b = 0.011$. The foreground mean is $\mu_{\mu_d} = 0.372$ and the standard deviation $\sigma_{\sigma_d} = 0.037$.

constant ($\mu_b = 0.30$ and $\sigma_b = 0.055$). From the results in Fig. 4.12, it is evident that Rosin's, Tsai's, and Kittler's methods perform equally well in the detection of defects and only Otsu's method provides distinctly worse results. The results are again most obvious in the discrepancy graph in Fig. 4.12(c) (note that Kapur's method is here omitted due to its poor performance earlier).

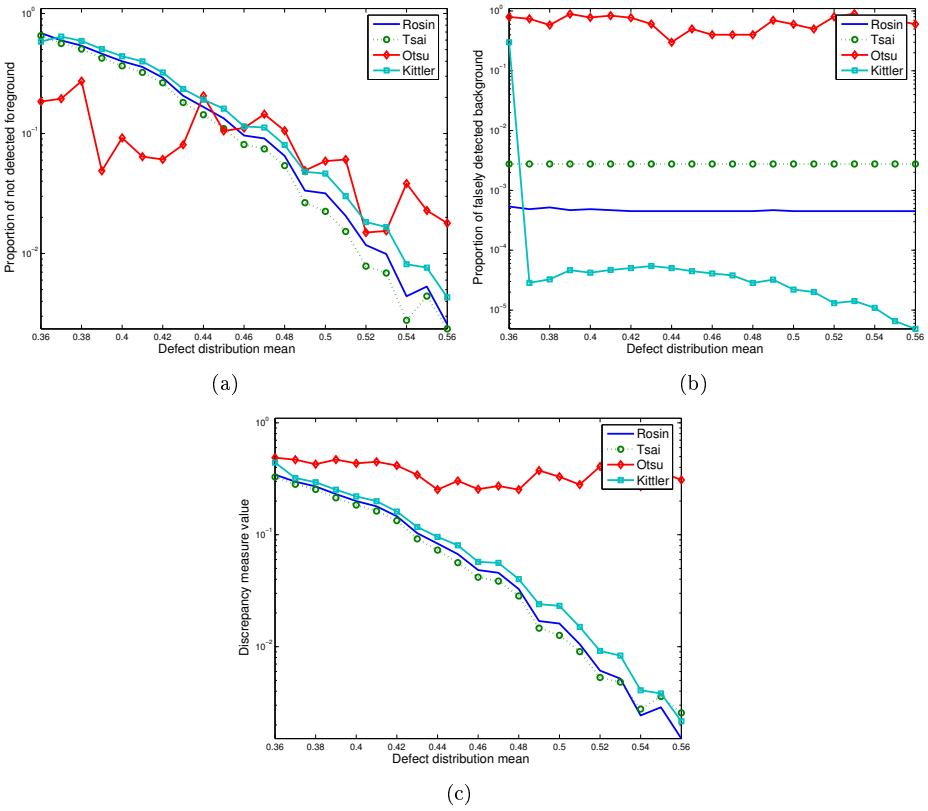

Figure 4.12: Detection results for artificial data as functions of defect distribution mean μ_{μ_d}, the background distribution was kept constant $mu_b = 0.30$, lower values are better: (a) Proportion of foreground pixels that were not detected, and (b) Proportion of pixels that were falsely detected as background pixels; (c) Discrepancy.

4.5 Experiments

In this section, the results with the real picking images are briefly described.

4.5.1 Picking images

A set of picking images captured under oblique lighting were used as the real test set for the candidate methods. As a preceding step to thresholding, an image enhancement procedure was applied to the images.

4.5.2 Image enhancement

In practice, input images often are or have been derived from images with only 8 bits per pixel, i.e., 256 intensity levels, so there is little motivation to generate histograms with more than 256 bins. However, certain image transformations, such as convolution filtering in the floating point form, can dramatically increase the number of intensity levels and produce larger histograms which allow a more precise threshold estimation. Another benefit of the filter is that it encompasses the spatial of a single defect and therefore makes the detection of defects more accurate since intensity and spatial information can be used.

It is clear that certain image enhancement techniques may lead to more accurate thresholding results since sub-level accuracy is achieved. With fine and sparse details, it can be beneficial to filter the image with a spot detection filter. By filtering with a simple $n \times n$ filter, the number of distinct intensities in an image can increase up to the factor of n^2 times. Such image preprocessing before constructing the histogram agrees with the results presented in [5]. In the case of the picking images, the following spot detection filter was used:

$$f = \begin{pmatrix} -1 & -1 & -1 & -1 & -1 & -1 & -1 \\ -1 & 0 & 0 & 0 & 0 & 0 & -1 \\ -1 & 0 & 1.5 & 3 & 1.5 & 0 & -1 \\ -1 & 0 & 3 & 6 & 3 & 0 & -1 \\ -1 & 0 & 1.5 & 3 & 1.5 & 0 & -1 \\ -1 & 0 & 0 & 0 & 0 & 0 & -1 \\ -1 & -1 & -1 & -1 & -1 & -1 & -1 \end{pmatrix} . \tag{4.13}$$

The main reason for the image enhancement for the picking images was removal of undesired imaging effects on the paper samples, such as the waving appearing in Fig. 4.5(a) (visible in the top row images). This spot filter is not necessary for uncoated papers, which do not suffer partial delamination in the same way as coated papers do. Uncoated papers do not suffer from waving and therefore this step, again, is not required although it does enhance small details even in uncoated paper images.

Image examples

Figs. 4.13 and 4.14 show four picking images for coated papers, their enhanced versions, and the results for all five thresholding methods. The results with the real images correspond to the results with the artificial data: two of the most promising methods are Rosin's method and Kittler's method. Rosin's method detects more foreground pixels, but also falsely detects a large number of background pixels. This is evident from Figs. 4.10, 4.13 and 4.14. Therefore, Kittler's method corresponds more precisely to what is to be detected from the original images.

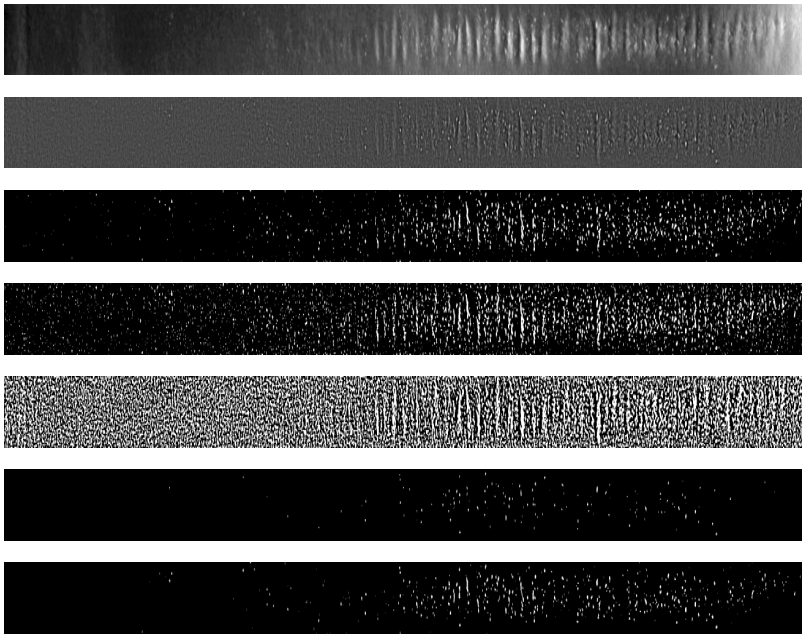

(a)

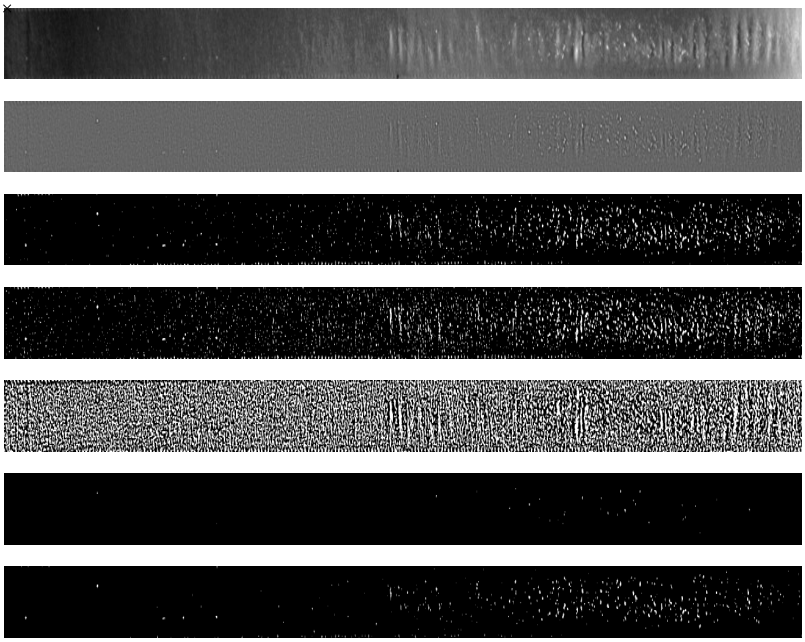

(b)

Figure 4.13: Two examples of picking images, and the thresholding results. Images from the top are the aligned image (top), the enhanced image, the result from the method by Rosin, Tsai, Otsu, Kapur, and Kittler (bottom).

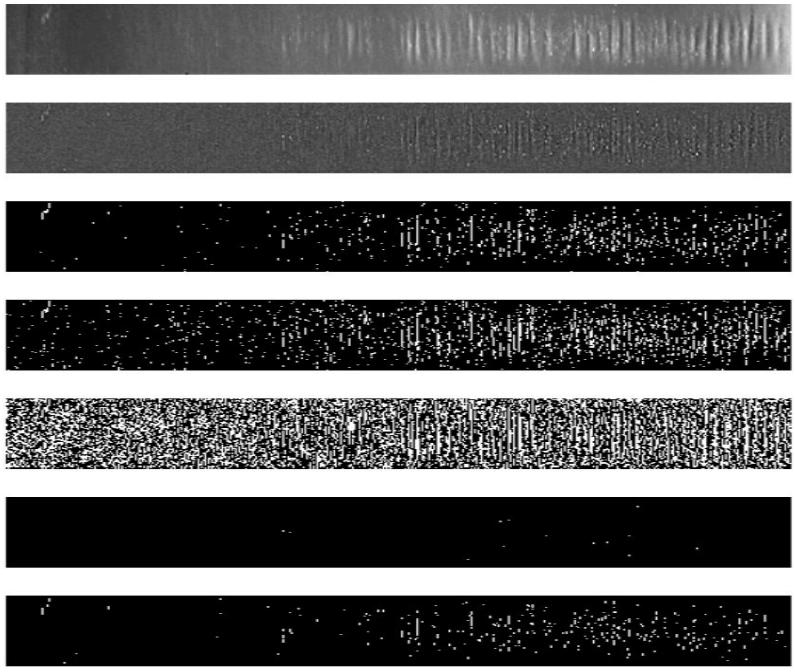

(a)

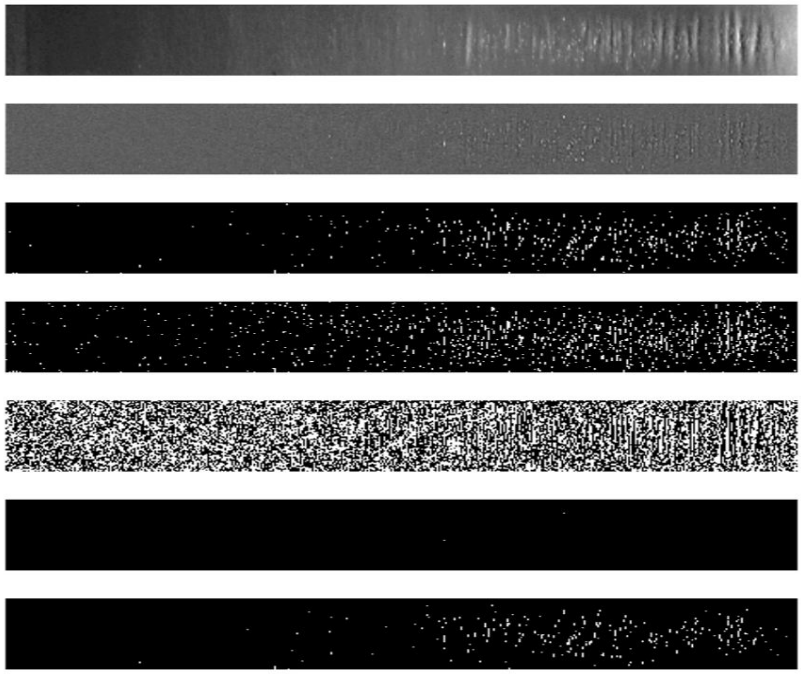

(b)

Figure 4.14: Two additional examples of picking images, and the thresholding results. Images from the top are the aligned image (top), the enhanced image, the result from the method by Rosin, Tsai, Otsu, Kapur, and Kittler (bottom).

4.6 Heuristics to determine the starting location of picking

After the images have been thresholded, some heuristics and post processing is required to determine the actual starting location of the picking. Currently the picking location is determined by calculating the profile of the thresholded binary image, i.e., the number of detected defects is summed over the length of the image so that a profile of the image is obtained. The picking starting location can be determined from the profile with some user definable parameters. The first parameter is the size of the picking N, which in a profile graph means that all values below this number are considered as being not picking but some noise such as dust speckles or irrelevant (too small) pickings. When the profile graph exceeds the set threshold N its length above the threshold is measured. If the measure is higher than d, the picking is marked to start at the location where the profile graph first exceeded threshold N. In order to allow small gaps in the thresholded graph, a third variable d_{min} is used. It ignores small gaps in the thresholded graph if they are not longer than d_{min}. Fig. 4.15 demonstrates how the heuristics work to determine the picking start location.

This is just one example of the heuristics that can be used to determine the starting location of the picking. It has been advised by numerous industrial experts that this step should be as customisable as possible. Different laboratories, even inside same company, have different ways to actually determine the picking start location depending on their customers' requirements. Currently, the paper and printing industry are trying to define a standard that would define picking more clearly but at the time of writing, the standard is not ready and thus cannot be used to define picking start location more clearly.

The whole picking detection method is summarised in algorithm 4.

Algorithm 4 *Method for detecting picking.*

1: *Image the sample.*
2: *Preprocessing.*
3: *Threshold the image.*
4: *Use heuristics to determine picking start location.*

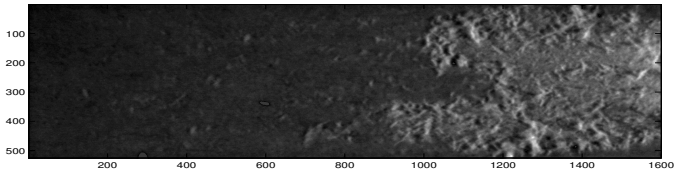

(a)

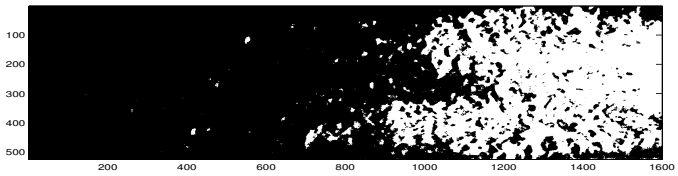

(b)

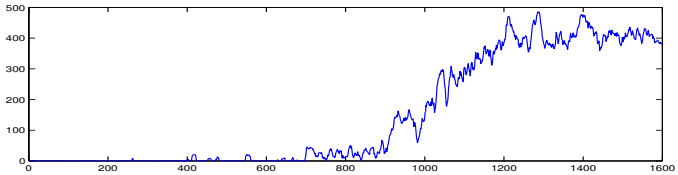

(c)

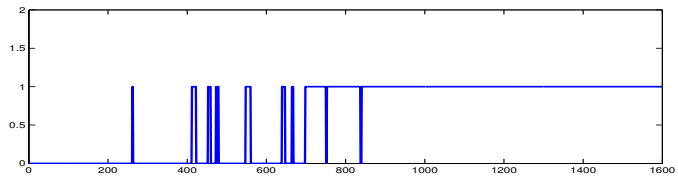

(d)

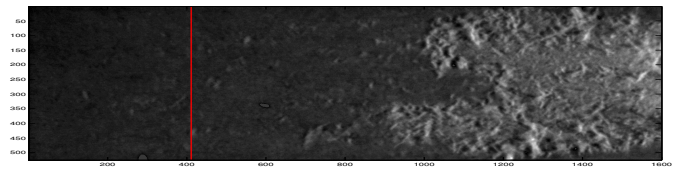

(e)

Figure 4.15: Example of the heuristics procedure. a) Grey level image of picking sample; b) After Kittler's thresholding; c) Projection of thresholded image.; d) Thresholded projection, 1 designated picking area and 0 background; e) Picking start location marked in the original grey level image (dark line at around 400).

4.7 Summary

In this chapter, an automated method for detecting picking from printed test samples was introduced. A model for images with fine and sparse details was also given based on statistical properties in the image grey-level histogram domain. Based on the proposed model, several well-known and widely used thresholding methods were studied to evaluate their performance as functions of the model variables, and the most promising methods were proposed for detecting fine and sparse details.

The proposed model aimed to explain characteristics of real images containing different types of defects on a noisy background. An adaptable and problem specific method was introduced in this thesis for the automatic evaluation of picking samples. Visualisation of the model corresponded to the real data, and the results with real images verified the analytical results. Based on the study and the conducted experiments, Kittler's and Illingworth's minimum error thresholding was selected as the most suitable method for the given task.

Determining the actual starting location of picking was complicated. Different paper and printing industry experts have different opinions about what should be considered as picking and therefore only an adaptable and problem specific method was introduced.

Chapter V

Imaging setup for performing the Heliotest and picking test

During the course of the thesis work, a laboratory test setup for performing the Heliotest and picking test inspection on printed samples was built. The setup enabled testing the methods introduced in the earlier chapters.

5.1 Imaging setup

As mentioned in Chapter 3, the Heliotest has demanding requirements for image resolution. Furthermore the printed Heliotest and picking test samples should not come into contact with anything during industrial quality inspection tests since the ink can still be wet and lift fibres should not be folded back into the paper surface. In order to meet these requirements, an Allied Vision Oscar F510C CCD camera with Moritex ML-Z0108 micro objective lens was chosen as the imaging device. Table I.1 in Appendix I lists the camera specifications and specifications for the lens are listed in Table I.2. The camera was attached to a computer via a Firewire connection. The benefit of this arrangement was that the camera could now be controlled via Linux due to freely distributed Firewire drivers [17].

Two different light sources were selected to illuminate samples below the camera. For the Heliotest samples, a ring light illuminating the samples directly from above was chosen. For the picking samples, two high pressure 250W halogen lights were chosen to meet the oblique illumination requirement. The lights were attached to an adjustable handle and could be adjusted to provide light at low angles with respect to a sample. Specifications for the ring light and its light source are listed in Tables I.3 and I.4.

One problem with the camera arrangement was that the whole sample did not fit into an image and had to be imaged in parts. A solution for this imaging difficulty was to use a very accurate desktop robot to move either the sample or the camera. Specifications for the Sony Cast Pro II robot are given in Table I.5. The accuracy of the robot enables the user to move the camera or sample very accurately to a known position which means that time consuming image alignment was not needed but done by the robot.

In the system, imaging is done by placing the sample on the robot table and the camera is moved above the sample. The sample is imaged in parts and each image part is processed with the proposed algorithms. Image acquisition is asynchronous which, means that the actuator moves to the next location while the current image is being processed. Fig. 5.1 shows the whole test setup.

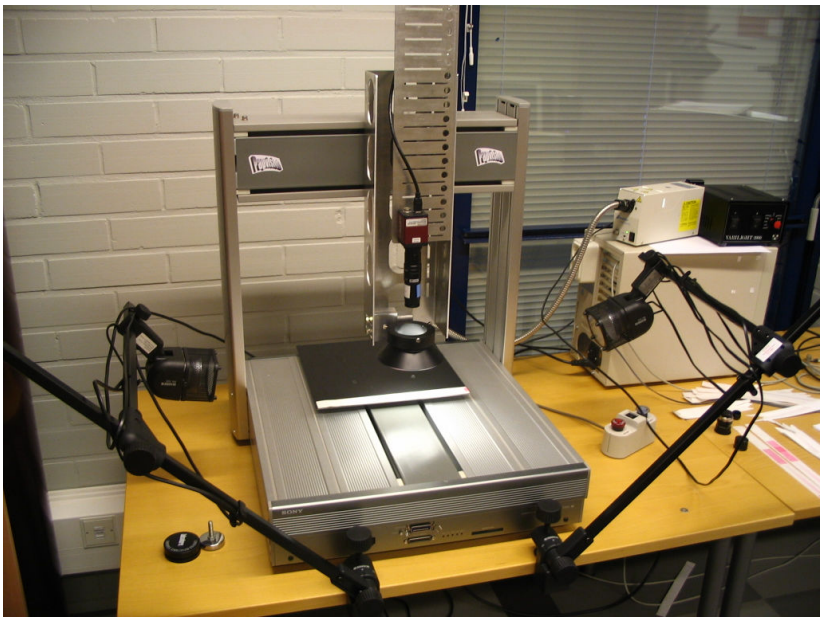

Figure 5.1: Experimental setup ready for analysing Heliotest sample.

5.2 Detecting the rectangular measurement area

After an image of a sample is acquired, the rectangular measurement area must be located in order to avoid unnecessary image processing. Regions outside the measurement area do not provide any necessary information but only slow processing. Furthermore, dots can be falsely detected as missing outside of the measurement area since that area is blank and does not contain any dots. The measurement area differs from the background based on its texture pattern and colour. In short, the measurement area is detected by edge detectors, Hough transform and heuristics.

In order to reduce the number of unnecessary details like edges of individual dots in the Heliotest and to speed up processing, the input image is first downsampled. The scaling factor can be set by the user and it should be selected so that individual dots inside the measurement area become indistinguishable from each other. In this way the measurement area itself is portrayed in one colour and the background in a noticeably different one. After downsampling, the image is filtered using a Gaussian filter so that any minor details left in the image become blurred and do not appear as edges. Fig. 5.2

shows the original image and the images after it has been down sampled and Gaussian filtered.

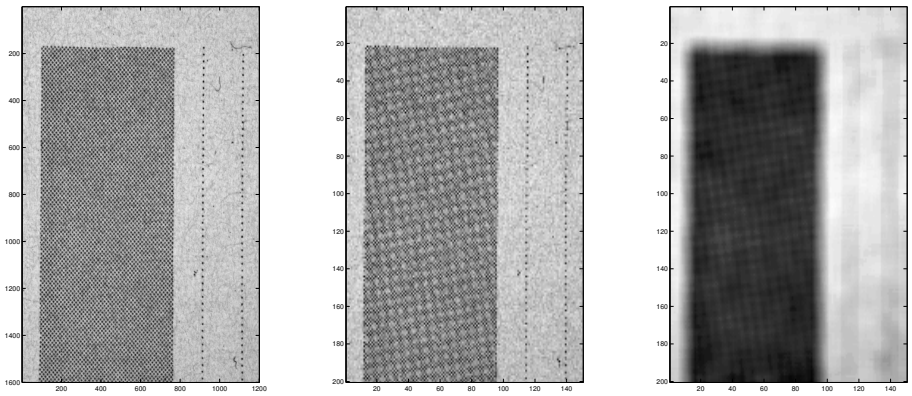

(a) (b) (c)

Figure 5.2: Image processing before edge detection: (a) Original grey-level image; (b) Downsampled; (c) After Gaussian filtering.

After image smoothing by Gaussian filter, the edges of the measurement area are detected using edge detector. The Canny edge detector [10] was chosen for the task because of its good performance compared to other methods [80]. The Canny algorithm requires two parameters which are application dependant. The parameters are called hysteresis thresholds. The upper threshold defines a value above which a possible edge is identified to be an actual edge. The lower threshold tries to connect partial edges together. If the pixel next to an accepted edge pixel drops below the higher threshold but stays above the lower one, it is considered as belonging to the same edge. These parameters are usually found by trial and error but more refined methods have also been studied [58].

After the edge lines of the measurement area are detected, their parameters are established. The edge line parameters are needed for determining the actual shape of the measurement area. Only the corner points of the measurement area are actually needed, but in order to detect the corner points, crossings of the edge lines are needed. Fig. 5.3 shows how the edge lines are used.

Edge line parameters are determined by using the Hough transform [54]. The number of lines to be detected is limited to four since the measurement area consists of four edges.

After the corner points have been obtained, a bounding box can be used to either define the measurement area or the area can be rotated to strictly vertical by using the affine transform [81]. By rotating the image, unnecessary data is removed thus making image manipulation faster. The downside of the rotation operation is its rather heavy computational cost with large images. The rotation matrix required for the affine transformation

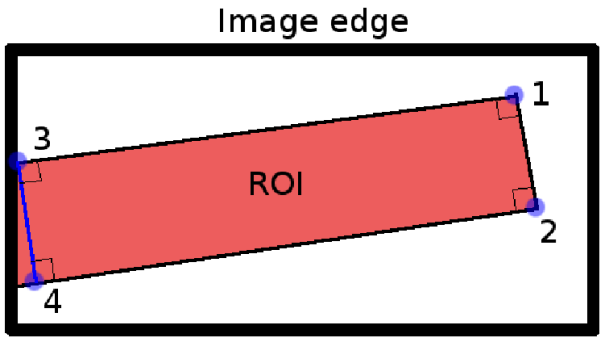

Figure 5.3: Example of corner detection, corners are numbered in detection order.

is formed based on the corner point information. Fig. 5.4 show an input image and the detected measurement area using the described method. The whole measurement detection algorithm is summarised in algorithm 5.

Algorithm 5 *Detecting the printed measurement area.*

1: *Downsample the image.*
2: *Smooth the image.*
3: *Detect edges of the image by using the Canny edge detector.*
4: *Estimate the parameters of the edge line by using Hough transform.*
5: *Calculate the crossing points of edge lines.*
6: *Define bounding box for the measurement area based on edge points.*

It should be noted that the detected measurement area will have some minor errors since the measurement area calculations are done to downsampled image. The full sized measurement area can have an error by the down sampling factor. Also the Gaussian filtering causes the edge of the measurement area to blur thus making detection of the actual edge more inaccurate, as can be seen from Fig. 5.4(b). However, these minor errors do not harm the later processing. In addition no aliasing effect happens in the resulting image since the image is not downsampled, only cropped.

After measurement area detection, the methods introduced in the previous chapters can be used to detect missing dots or pickings from the imaged sample. Each individual image is processed separately and coordinates of missing dots or possible pickings are saved. After the 20th missing dot or picking point is located, the distance is calculated and shown on the screen both in pixels and in millimetres.

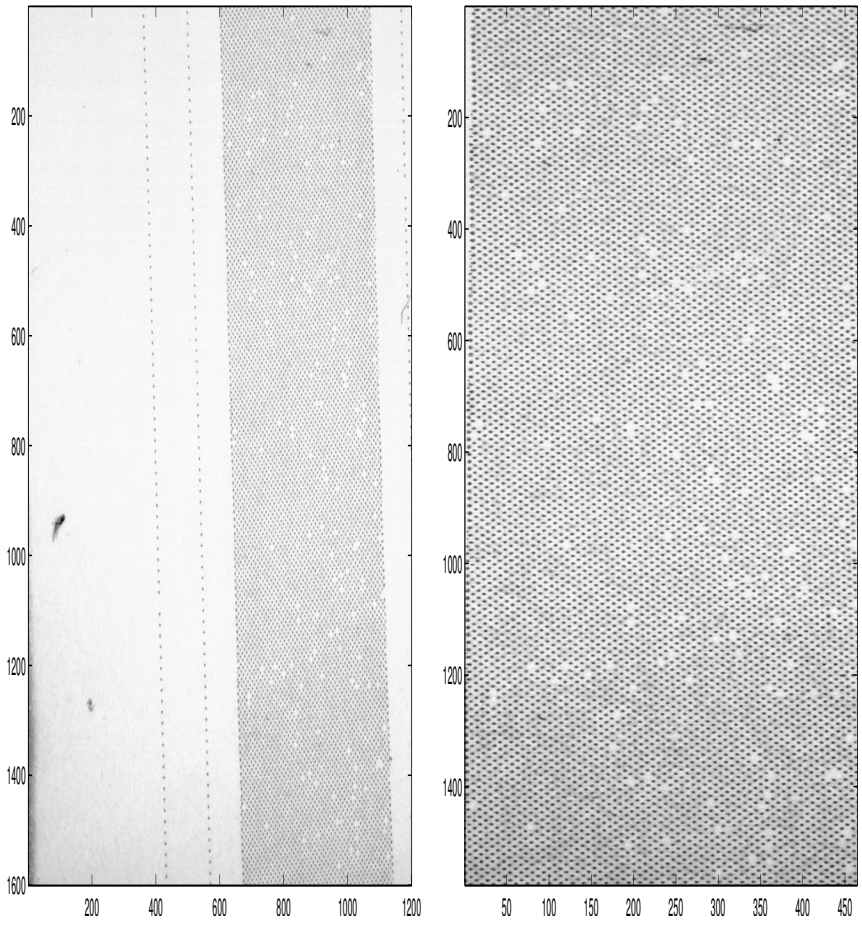

Figure 5.4: Measurement area detection: (a) Image of a Heliotest strip; (b) Measurement area detected from the same image.

5.3 Experiments

The experimental setup was tested with the co-operation of industrial partners at paper mills. The tests were preliminary in nature but they give a good indication of the potential of the setup in automating the quality inspection tasks. Appendix II lists the results obtained by two laboratory experts and the experimental setup regarding picking test inspection. Both experts marked picking location on a separate paper without seeing each other's markings. Finally the experimental setup was used to analyse the same samples.

Hand marked distances are measured using an ordinary 30 cm long ruler and therefore can easily contain errors of about ± 1 mm which should be kept in mind when the results are assessed. The results were quite satisfactory most of the time, picking was found correctly but determining where to mark the picking starting location requires more consideration. The coefficient of determination (R^2) between the measurements of experts and these of the setup are listed in Table 5.1. As can be seen, the setup results correlate better with expert 1 than with expert 2 but there is still a notable difference of opinions about missing dot locations between the setup and the experts. However, even the experts are not unanimous about the picking start location.

Table 5.1: Coefficient of determination between expert measures and setup measures with picking test samples. E denotes expert and S denotes setup. Correlations were calculated over all different paper qualities.

E1 vs S	E2 vs S	E1 vs E2
0.84	0.81	0.97

Similar tests with the Heliotest were also performed. The individual results can be found from appendix III. The setup performed very well with the Heliotest, there were some troublesome cases where the dots were so dimly printed that the setup mistakenly labelled them as missing dots, whereas human experts did not. Fig. 5.5 demonstrates this. The decision to classify dot as a missing/not missing can be subjective and the threshold for marking a dot as a missing depends on the set threshold. The coefficient of determination correlations between the setup and experts are listed in Table 5.2. As can be seen from the results, measurements between experts and the experimental setup are very well aligned.

Table 5.2: Correlations between expert measures and setup measures with Heliotest samples. E denotes expert and S denotes setup. Correlations were calculated over all different paper qualities.

E1 vs S	E2 vs S	E3 vs S	E1 vs E2	E1 vs E3	E2 vs E3
0.99	0.99	0.99	1.00	1.00	0.99

Statistics for individual paper grades were not calculated due to the few measurements available. The industrial partners were satisfied with the accuracy of the methods and

the experimental setup. The speed of the measurement methods were also deemed satisfactory. The picking test for a single sample could be performed in about 10 seconds. For the Heliotest it took a bit longer, a single test sample is analysed in about a minute. A laboratory expert can perform the same tests in about 30 seconds per sample, depending on the level of experience and difficulty of the sample.

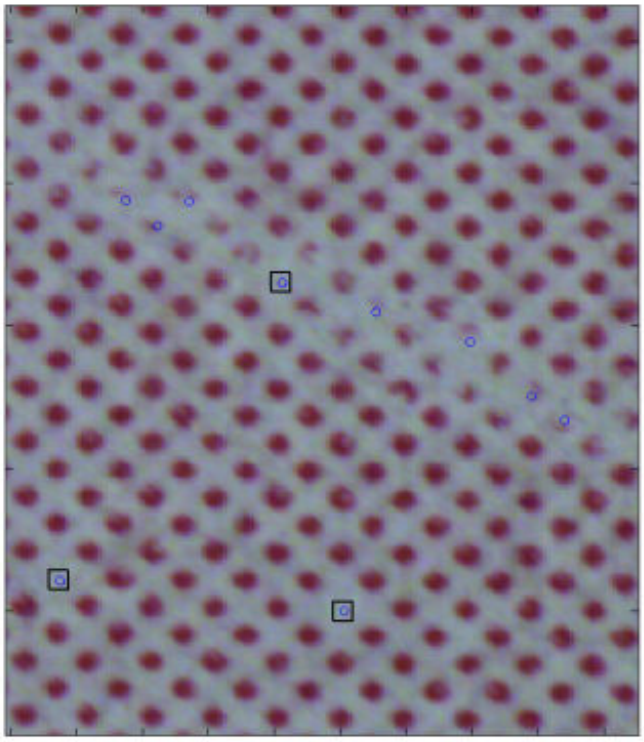

Figure 5.5: Cluster of falsely located missing dots. Circles mark missing dots found automatically, missing dots found by laboratory expert have been marked with squares.

5.4 Summary

This chapter explained how the methods introduced in the previous chapters were applied to an experimental test setup. The setup was introduced and its specifications presented. A method for detecting the measurement area from the Heliotest and picking test images

was also presented. Finally the setup was used to perform the Heliotest and picking test inspection on samples that were also evaluated by industrial experts. The results of these tests are given in appendices II and III. Industry partners were satisfied with the setup performance. Although the Heliotest could be performed faster manually, the benefit of using automation comes from repeatability and reduction in eye strain.

Chapter VI

Discussion

The objective of this thesis was to seek methods to detect irregularities from regular patterns and methods for detecting small and sparse details from images. Two paper quality measurement problems in paper and printing industry were introduced as practical problems: The first was the detection of missing dots from Heliotest patterns and the second detection of small and sparse details from IGT picking samples.

The first practical problem is generally related to regular patterns and how to detect irregularities from them. The well known Fourier transform was selected as a basis for further study. Three methods were developed for detecting irregularities (missing "dots") from regular patterns based on Fourier analysis. Their performance in the Heliotest inspection task was analysed and the generality of methods was discussed. The proposed methods are applicable to all tasks where regular pattern may contain irregularities, for example, the inspection of patterned wafers, and a very similar method is patented for integrated circuit fault detection [75]. For irregularity detection it became apparent that a good contrast between the object and the background gives better results and therefore a contrast enhancement algorithm based on Bayesian decision making was developed. The posteriori contrast enhancement method made the task of thresholding the irregular image easier. The most noteworthy advantage of the proposed irregularity detection methods over the methods proposed earlier in [53, 31, 47] are their ability to detected multiple irregularities clustered next to each other.

The weaknesses of the proposed irregularity detection method appear when the actual irregularities are segmented from the irregular image. Selecting a suitable threshold for detection is not simple. Small variations in the image, such as noise, can easily be falsely interpreted as irregularities. To counter this, the irregular image can be thresholded and analysed so that the binarised areas have to match the sizes of the actual dots in the regular image part. In this way noisy pixels in the binarised image do not affect the irregularity detection process.

There is also a practical problem with Heliotest. The printed pattern edges are not always straight, meaning that the edge line of printed dots can suddenly shift one dot

column left or right. When this happens in the middle of an image, the empty space after the shift can be mistaken as a column of missing dots. This problem is countered by simply ignoring a certain amount of missing dots near the image edges. By applying the proposed methods to an imaging setup, the Heliotest could be performed with very satisfying results.

The second problem addressed in this work was the detection of small and sparse details from images such as IGT picking sample images. Well known thresholding methods were chosen for the task and their performances with artificial small and sparse details were compared. Kittler's and Illingworth's minimum error thresholding was chosen as the most suitable for the task. When applied in practice on IGT picking sample images, picking (paper surface tearing) in the images is detected accurately; problems are more related to analysing the actual thresholded images. Consensus needs to be reached on how the picking start location is defined. The current method produces repeatable results, but still may fail to satisfy experts because their opinions differ on how to define the picking start location. Therefore, testing the method with real picking test images with ground truth data is difficult, since no common ground is found on how to define the ground truth. Marking picking spots manually on the samples would take a lot of time and would still produce subjective results. Therefore to reliably to measure thresholding performance an artificial data was used. For the artificial data, the exact ground truth was available.

In the future studies, more information about determining the picking starting location from the thresholded images is needed. Industry would prefer the results to be close to those obtained by human evaluation. Spatial information of the defects could be used more, along with intensity, as the separation between the background and defects in picking images might improve.

In this thesis, an experimental setup is presented, which utilises the methods introduced to detect irregularities and small and sparse details. The performance of the setup is measured by performing Heliotests and picking tests on expert evaluated samples. Feedback on the performance of the setup from paper laboratories has been encouraging and therefore further product development is justified.

[1] Properties of paper. Available: http://www.paperonweb.com/paperpro.htm, Referenced: 6.11.2006.

[2] Acciani, G., Brunetti, G., and Fornarelli, G. Application of neural networks in optical inspection and classification of solder joints in surface mount technology. *IEEE Transactions on Industrial Informatics 2*, 3 (2006), 200–209.

[3] Ashcroft, N., and Mermin, N. *Solid State Physics*. Thomson Learning, Inc., 1976.

[4] Bailey, D. Detecting regular patterns using frequency domain self-filtering. In *Proc. Int. Conf. on Image Processing* (1997), vol. 1, pp. 440–443.

[5] Baradez, M.-O., McGuckin, C., Forraz, N., Pettengell, R., and Hoppe, A. Robust and automated unimodal histogram thresholding and potential applications. *Pattern Recognition 37*, 6 (2004), 1131–1148.

[6] Bergman, L., Verikas, A., and Bacauskiene, M. Unsupervised colour image segmentation applied to printing quality assessment. *Image and Vision Computing*, 23 (2005), 417–425.

[7] Berndtson, J., and Niemi, A. Automatic observation of the dry line in paper machine. In *International Conference on Pattern Recognition* (1996), vol. 3, pp. 308–312.

[8] Calderon-Martinez, J., and Campoy-Cervera, P. A convolutional neural architecture: an application for defects detection in continuous manufacturing systems. In *Proceedings of the 2003 International Symposium on Circuits and Systems* (2003), vol. 5, pp. 749–752.

[9] Campoy, P., Canaval, J., and Peña, D. InsPulp-IC: an on-line visual inspection system for the pulp industry. *Computers in Industry 56*, 8 (2005), 935–942.

[10] Canny, J. A computational approach to edge detection. *IEEE Transactions on Pattern Analysis and Machine Intelligence 8*, 6 (1986), 679–698.

[11] Carvalho, P., Araújo, H., and Dourado, A. An automatic optical sensor for vessels and fibbers quality inspection in pulp production. *Computers & Industrial Engineering 37*, 1-2 (1999), 355–358.

[12] Chan, C.-H., and Pang, G. Fabric defect detection by fourier analysis. *IEEE Transactions on Industry Applications 36*, 5 (2000), 1267–1276.

[13] Chen, C., R.J., P., and Wygant, R. A review of techniques for characterizing paper coating surfaces, structures and printability. In *Proceedinds of Tappi Coating Funcdamentals Symposium* (1995).

[14] Chin, R. Automated visual inspection: 1981 to 1987. *Computer Vision, Graphics, and Image Processing 41*, 3 (1988), 346–381.

[15] Cover, T., and Thomas, J. *Elements of Information Theory.* John Wiley & Sons, 1991.

[16] de la Escalera, A., Moreno, L., Salichs, M., and Armingol, J. Road traffic sign detection and classification. *IEEE Transactions on Industrial Electronics 44*, 6 (1997), 848–859.

[17] Dennedy, D., Douxchamps, D., and Peters, G. *1394 Based DC control library.* Sourceforge.net, Referenced: 24.11.2006. Available: http://sourceforge.net/projects/libdc1394.

[18] Donoser, M., Wiltsche, M., Bischof, H., and Bauer, W. Paper coating layer analysis based on computer vision methods. In *International Conference on Quality Control by Artificial Vision* (2005).

[19] Drobchenko, A. Automated picking assessment using machine vision. Master's thesis, Lappeenranta University of Technology, 2004.

[20] Drobchenko, A., Vartiainen, J., Kamarainen, J.-K., Lensu, L., and Kälviäinen, H. Thresholding based detection of fine and sparse details. In *IAPR Conference on Machine Vision Applications* (2005), pp. 257–260.

[21] Elektronische Mess-und Steuerungstechnik GmbH, E. Image Analysis, Referenced: 22.9.2006. Available: http://www.emco-leipzig.com/english/download/prospekte_eng.htm.

[22] Fernández-García, N., Medina-Carnicer, R., Carmona-Poyato, A., Madris-Cuevas, F., and Prieto-Villegas, M. Characterization of empirical discrepancy evaluation measures. *Pattern Recognition Letters 25* (2004), 35–47.

[23] Gonzalez, R. C., and Woods, R. E. *Digital Image Processing.* Prentice-Hall, Inc., 2002. ISBN 0-201-18075-8.

[24] Granlund, G. H. In search of a general picture processing operator. *Computer Graphics and Image Processing 8* (1978), 155–173.

[25] Hall, E. Almost uniform distributions for computer image enhancement. *IEEE Trans. Computers C-23*, 2 (1974).

[26] Hansson, P., and Manneberg, G. Fourier optic characterization of paper surfaces. *Optical Engineering 36*, 1 (1997), 35–39.

[27] Hansson, P., and Manneberg, G. Fourier optic online measurement of the dimensional variations in paper. *Optical Engineering 38*, 10 (1999), 1683–1687.

[28] Haralick, R. M. Statistical and structural approaches to texture. *Proc. of the IEEE 67*, 5 (1979), 786–804.

[29] Healey, G., and Slater, D. Global colour constancy: recognition of objects by use of illumination-invariant properties of colour distributions. *Optical Society of America. Journal A: Optics, Image Science, and Vision 11*, 11 (1994), 3003–3010.

[30] Hedsten, H., and Mannenberg, G. Optical Fourier analysis of a diffusely reflective screen dot pattern with an optically addressed spatial light modulator. *Optical Engineering 34*, 2 (1995), 535–547.

[31] Heeschen, W., and Smith, D. Robust digital image analysis method for counting missing dots in gravure printing. In *Proceedings of International Printing & Graphic Arts Conference* (Atlanta, GA, USA, 2000), pp. 29–35.

[32] Heikkurinen, A. *Pulp and Paper Testing*, vol. 17 of *Papermaking Science and Technology*. Fapet Oy, 1999, ch. Single fiber properties.

[33] Ho, T., and Smith, W. Applying digital image technology to pulp and paper. In *Canadian Conference on Electrical and Computer Engineering*, vol. 2, pp. 1139 – 1143.

[34] Huang, J., Kumar, S., Mitra, M., Zhu, W.-J., and Zabih, R. Image indexing using color correlograms. In *IEEE Computer Society Conference on Computer Vision and Pattern Recognition* (1997), pp. 762–768.

[35] Hummel, R. Histogram modification techniques. *Computer Graphics and Image Processing 4* (1975).

[36] IGT. IGT information leaflet W41, Heliotest, Referenced: 10.9.2006. Avalable: http://www.igt.nl/igt-site-220105/index-us/w-bladen/GST/W41.pdf.

[37] IGT. IGT information leaflet W31: IGT AIC2-5 from type AA PICKING, IGT method, aluminium disc, Referenced: 2.10.2006. Avalable: http://www.igt.nl/igt-site-220105/index-uk/w-bladen/AIC/oud/W31.pdf.

[38] Intopii Oy, Referenced: 22.9.2006. Available: http://www.intopii.fi/index.php?section=english.Products.PINTA_Paper.

[39] ISO standard. *ISO 3783, Paper and board – Determination of resistance to picking – Accelerated speed method using the IGT-type tester (electric model).*

[40] ISO standard. *ISO 287, Paper and board – Determination of moisture content – Oven-drying method*, 1985.

[41] ISO standard. *ISO 187, Paper, board and pulps – Standard atmosphere for conditioning and testing and procedure for monitoring the atmosphere and conditioning of samples*, 1990.

[42] ISO standard. *ISO 536, Paper and board – Determination of grammage*, 1995.

[43] ISO STANDARD. *ISO 2144, Paper, board and pulps – Determination of residue (ash) on ignition at 900 degrees C*, 1997.

[44] ISO STANDARD. *ISO 186, Paper and board – Sampling to determine average quality*, 2002.

[45] KANG, H. R. *Digital Color Halftoning*. SPIE Press, 1999.

[46] KAPUR, J., SAHOO, P., AND WONG, A. A new method for gray-level picture thresholding using the entropy of the histogram. *Computer Vision Graphics and Image Processing 29* (1985), 273–285.

[47] KHALAJ, B., AGHAJAN, H., AND KAILATH, T. Patterned wafer inspection by high resolution spectral estimation techniques. *Machine Vision and Applications 7* (1994), 178–185.

[48] KIISKINEN, H. T., KUKKONEN, H. K., PAKARINEN, P. I., AND LAINE, A. J. Infrared thermography examination of paper structure. *TAPPI 80*, 4 (1997), 159–162.

[49] KITTLER, J., AND ILLINGWORTH, J. Minimum error thresholding. *Pattern Recognition 19* (1986), 41–47.

[50] KJAER, A., WELLSTEAD, P., AND HEATH, W. On-line sensing of paper machine wet-end properties: dry-line detector. *IEEE Transactions on Control Systems Technology 5*, 6 (1997), 571–585.

[51] KLINKER, H. Computerized mottle and Heliotest analysing: the-state-of-the-art-solution for mottle and Heliotest analysis. In *Appita Annual General Conference* (1998), vol. 2, pp. 591–594.

[52] LAITINEN, J. Effect of charge transfer efficiency on image quality in CCD line scan-based web inspection. *Optics and Lasers in Engineering 29*, 6 (1998), 385–401.

[53] LANGINMAA, A. An image analysis based method to evaluate gravure paper quality. In *Proceedings of the 11th IAPR International Conference on Computer Vision and Applications* (1992), vol. 1, pp. 777–780.

[54] LEAVERS, V. Which Hough transform. *CVGIP: Image understanding 58*, 2 (1993), 250–264.

[55] LEVLIN, J.-E. *Pulp and Paper Testing*, vol. 17 of *Papermaking Science and Technology*. Fapet Oy, 1999, ch. Aim of pulp and paper testing.

[56] LEVLIN, J.-E. *Pulp and Paper Testing*, vol. 17 of *Papermaking Science and Technology*. Fapet Oy, 1999, ch. General physical properties of paper and board.

[57] LIA, Q., WANG, M., AND GU, W. Computer vision based system for apple surface defect detection. *Computers and Electronics in Agriculture 36*, 2-3 (2002), 215–223.

[58] LIU, G., AND HARALICK, R. Two practical issues in Canny's edge detector implementation. In *15th International Conference on Pattern Recognition* (2000), vol. 3, pp. 676–678.

[59] Luo, J., and Zhang, Z. Automatic colour printing inspection by image processing. *Journal of Materials Processing Technology*, 139 (2003), 373–378.

[60] Malamas, E., Petrakis, E. G. M., Zervakis, M., PetitL., and Legat, J.-D. A survey on industrial vision systems, applications and tools. *Image and Vision Computing 21*, 2 (2003), 171–188.

[61] Medina-Carnicer, R., Madrid-Cuevas F.J.and Fernández-García, N., and Carmona-Poyato, A. Evaluation of global thresholding techniques in non-contextual edge detection. *Pattern Recognition Letters 26*, 10 (2005), 1423–1434.

[62] Moraleda, J., Ollero, A., and Orte, M. A robotic system for internal inspection of water pipelines. *Robotics & Automation Magazine 6*, 3 (1999), 30–41.

[63] Myller, K., Juuti, M., Peiponen, K.-E., R., S., and Heikkinen, E. Quality inspection of metal surfaces by diffractive optical element-based glossmeter. *Precision Engineering* (2006), In press.

[64] Mäenpää, T., Pietikäinen, M., and Ojala, T. Robust texture classification by subsets of local binary patterns. In *International Conference on Pattern Recognition* (2000), vol. 3, pp. 935–938.

[65] Newman, T., and Anil, K. J. A survey of automated visual inspection. *Computer Vision and Image Understanding 61*, 2 (1995), 231–262.

[66] Odemir, S., Baykut, A., Meylani, R., Ercil, A., and Ertuzun, A. Comparative evaluation of texture analysis algorithms for defect inspection of textile products. In *Fourteenth International Conference on Pattern Recognition* (1998), vol. 2, pp. 1738–1740.

[67] Oja, E., and Kohonen, T. The subspace learning algorithm as a formalism for pattern recognition and neural networks. *IEEE Int. Conf. on Neural Networks 1* (1988), 277–284.

[68] Otsu, N. A threshold selection method from gray-level histograms. *IEEE Transactions on Systems, Man, and Cybernetics 9*, 1 (1979), 62–66.

[69] Paalanen, P., Kamarainen, J.-K., Ilonen, J., and Kälviäinen, H. Feature representation and discrimination based on Gaussian mixture model probability densities—Practices and algorithms. *Pattern Recognition 39* (2006), 1346–1358.

[70] Pardo, A., and Sapiro, G. Visualization of High Dynamic Range images. *IEEE Transactions on Image Processing 12*, 6 (2003).

[71] Paul, D., Hattich, W., Nill, W., Tatari, S., and Winkler, G. VISTA: visual interpretation system for technical applications -architecture and use. *Pattern Analysis and Machine Intelligence 10*, 3 (1988), 399–407.

[72] Phung, S., Bouzerdoum, A., and Chai, D. Skin segmentation using color pixel classification: Analysis and comparison. *IEEE Transactions on Pattern Analysis and Machine Intelligence 27*, 1 (Jan. 2005), 148–154.

[73] Piette, P., Morin, V., and Maume, J. Industrial-scale rotogravure printing tests. *Wochenblatt für Papierfabrikation 125*, 16 (1997), 744–750.

[74] Rosin, P. Unimodal thresholding. *Pattern Recognition 34*, 11 (2001), 2083–2096.

[75] Russell, J. *Spatial filtering method for failure analysis of a device.* United States Patent 6731824, 2004.

[76] Sadovnikov, A. Automated heliotest inspection using machine vision. Master's thesis, Lappeenranta University of Technology, 2003.

[77] Sadovnikov, A., Vartiainen, J., Kamarainen, J.-K., Lensu, L., and Kälviäinen, H. Detection of irregularities in regular dot patterns. In *IAPR Conference on Machine Vision Applications* (2005), pp. 380–383.

[78] SCAN standard. *SCAN 63:90, Surface strength, IGT.*

[79] Sezgin, M., and Sankur, B. Survey over image thresholding techniques and quantitative performance evaluation. *Journal of Electronical Imaging 13*, 1 (2004), 146–165.

[80] Sharifi, M., Fathy, M., and Mahmoudi, M. A classified and comparative study of edge detection algorithms. In *International Conference on Information Technology: Coding and Computing* (2002), pp. 117–120.

[81] Shizawa, M. Discrete invertible affine transformations. In *10th International Conference on Pattern Recognition* (1990), vol. 2, pp. 134–139.

[82] Smith, S. Color coding and visual separability in information displays. *Journal of Applied Psychology 47* (1963).

[83] Suontausta, O. *Pulp and Paper Testing*, vol. 17 of *Papermaking Science and Technology.* Fapet Oy, 1999, ch. End-use properties of printing papers.

[84] Tappi standard. *Surface Strength of Paper (IGT Tester) (Formerly T 499).*

[85] Teknosavo Oy. ChipSmart(tm), Referenced: 20.9.2006. Available: http://www.teknosavo.fi/tuotteet_entry.asp.

[86] Tong, Y. *The Multivariate Normal Distribution.* Springer Series in Statistics. Springer-Verlag, 1990.

[87] Tsai, D.-M. A fast thresholding selection procedure for multimodal and unimodal histograms. *Pattern Recognition Letters 16* (1995), 653–666.

[88] Tsai, D. M., and Hsieh, C. Y. Automated surface inspection for directional textures. *Image and Vision Computing 18*, 1 (1999), 49–62.

[89] Turtinen, M., Pietikäinen, M., Silven, O., Mäenpää, T., and Niskanen, M. Paper characterisation by texture using visualisation-based training. *The International Journal of Advanced Manufacturing Technology 11-12*, 22 (2003), 890–898.

[90] Vaarasalo, J. *Pulp and Paper Testing*, vol. 17 of *Papermaking Science and Technology.* Fapet Oy, 1999, ch. Optical properties of paper.

[91] Vartiainen, J., Lensu, L., Kamarainen, J.-K., Sadovnikov, A., and Kälviäinen, H. Detecting irregularities in regular patterns. In *Proceedings of the 18th International Conference on Pattern Recognition (ICPR2006)* (2006).

[92] Vartiainen, J., Lyden, S., Sadovnikov, A., Kamarainen, J.-K., Lensu, L., and Kälviäinen, H. Automating visual inspection of print quality. In *Proceedings of the International Conference on Image Analysis and Recognition* (2006).

[93] Vartiainen, J., Paalanen, P., Kämäräinen, J.-K., Lensu, L., and Kälviäinen, H. Minimum error contrast enhancement. Research report 102, Lappeenranta University of Technology, Department of Information technology, 2006.

[94] Vartiainen, J., Sadovnikov, A., Kamarainen, J.-K., Lensu, L., and Kälviäinen, H. Detection of irregularities in regular patterns. *Machine vision and applications* (2007). Accepted.

[95] Verikas, A., Malmqvist, K., and Bergman, L. Detecting and measuring rings in banknote images. *Engineering Applications of Artificial Intelligence 18*, 3 (2005), 363–371.

[96] Wygant, R., Pruett, R., and Chen, C.-Y. A review of techniques for characterizing paper coating surfaces. In *TAPPI International Paper Coating Fundamentals Symposium* (May 1995). (invited).

[97] Zhang, J. B. Computer-aided visual inspection for integrated quality control. *Computers in Industry 30*, 3 (1996), 185–192.

[98] Zimmerman, J., Pizer, S., Staab, E., Perry, J., McCartney, W., and Brenton, B. An evaluation of the effectiveness of adaptive histogram equalization for contrast enhancement. *IEEE Transactions on Medical Imaging 7*, 4 (1988).

APPENDIX I

Specifications for imaging setup

The technical specifications for imaging setup are listed below.

Table I.1: Specifications for Allied Vision Technologies OSCAR F-510C camera.

Manufacturer	Allied Vision Technologies
Model	OSCAR F-510C
Type	Industrial camera
Sensor size	2/3"
Resolution	up to 2588×1958
Pixel size	3.2 μm (square)
Sensor type	CMOS
Colour	RAW, RGB, YUV-4 : 2 : 2, Mono8
Scan type	True partial scan
Shutter speed	$20\mu s - 67s$
Resolution depth	from 12bit up to 16bit in high resolution mode
Connector	Firewire
Lens mount	C
Dimensions	$44 \times 44 \times 58.9$ mm
Drivers	Linux & Windows
Abilities	Possible to define custom resolution for images.

Table I.2: Specifications for Mortitex macro zoom objective.

Manufacturer	Moritex
Model	ML-Z0108
Type	$0.1\times - 0.8\times$ zoom lens
Working Distance	213 mm
WD adjustment	± 20 mm
Effective F Number	$8.2 - 9.3$
Depth of Field	$32.8 - 0.6$ mm
Resolution	$55 - 8$ μm
TV Distortion	$-0.02 \pm 0.17\%$ (or less)
Largest sensor	1/2"
Mount	C-mount

Table I.3: Specifications for light source.

Manufacturer	Moritex
Model	MHF-M1002
Type	100W Halogen type light source
Input Voltage	AC180 $\sim$ 250V
	50/60 Hz
Power consumption	270 VA
Lamp type	LM-100
Options	External light control (0–5 V)
	External volume light control
	External on/off
	Lamp rush current detection
	Internal temperature detection

Table I.4: Specifications for lamp.

Manufacturer	Moritex
Model	LM-100
Type	100W Halogen lamp
Power consumption	100 W
Lamp current	8.4 A
Average life	1000 h
Average luminosity	30000 lux
Colour Temperature	3100° K

Table I.5: Specifications for Sony Cast Pro II desktop robot.

Manufacturer	Sony
Model	Cast Pro II
Type	desktop robot
Operating area	350×350 mm
Moving precision	0.02 mm
Number of axis	2

APPENDIX II

Picking test with test setup

Picking test measurement results. All measures are given in millimetres. 5 different paper qualities were measured and each quality contained 5 samples. Different quality papers are separated with horizontal lines. Table II.1 lists the measurements.

Table II.1: Picking test results. Expert 1 and 2 results were obtained by human observations and Setup was performed by machine vision setup. All results are presented in millimetres. Quality refers to different paper grades.

Grade	**Sample**	**Expert 1**	**Expert 2**	**Setup**
Quality 1	1	88	81	99
	2	71	74	102
	3	73	73	97
	4	62	67	64
	5	80	82	97

Table II.2: Table II.1 continued.

Grade	Sample	Expert 1	Expert 2	Setup
Quality 2	1	51	47	49
	2	32	34	33
	3	32	29	36
	4	44	44	45
	5	42	42	43
Quality 3	1	40	40	43
	2	47	47	50
	3	42	40	43
	4	46	42	45
	5	42	44	39
Quality 4	1	93	89	85
	2	93	87	97
	3	92	90	113
	4	83	76	82
	5	82	69	85
Quality 5	1	184	137	137
	2	184	185	138
	3	194	193	143
	4	193	192	-
	5	181	183	122

APPENDIX III

Heliotest with test setup

The test was performed by 3 human experts and Setup. The greatest differences in measurements happened when some dimly missing dots were falsely classified as missing dots by the machine vision setup. Table III.1 lists the measurement results.

Table III.1: Heliotest results. Expert 1, 2, and 3 results were obtained by human observations and Setup was performed by machine vision setup. All results are presented in millimetres. Quality refers to different paper grades.

Grade	Sample	Expert 1	Expert 2	Expert 3	Setup
Quality 1	1	62	60	64	62
	2	56	56	56	54
	3	51	50	50	50
	4	63	62	63	62
	5	56	56	56	55
Quality 2	1	72	72	72	72
	2	61	60	61	63
	3	71	70	70	70
	4	69	67	68	64
	5	79	79	79	78
Quality 3	1	26	26	23	28
	2	20	20	19	20
	3	28	26	25	28
	4	31	29	29	30
	5	26	29	23	28

Table III.2: Table III.1 continued.

Grade	Sample	Expert 1	Expert 2	Expert 3	Setup
Quality 4	1	40	40	39	40
	2	47	46	46	46
	3	37	36	36	38
	4	47	46	46	47
	5	42	41	41	41
Quality 5	1	48	48	48	46
	2	51	50	50	50
	3	54	50	50	49
	4	63	63	63	60
	5	53	51	52	46
Quality 6	1	80	82	81	80
	2	90	90	89	89
	3	81	80	89	82
	4	85	85	84	84
	5	90	90	89	80
Quality 7	1	96	96	95	94
	2	110+	110+	110+	-
	3	105	106	105	101
	4	95	95	94	94
	5	106	107	106	105
Quality 8	1	78	77	76	77
	2	81	82	81	82
	3	65	66	65	66
	4	91	93	91	91
	5	80	82	80	80